COPPE
Instituto Alberto Luiz Coimbra de Pós-Graduação e Pesquisa de Engenharia
UFRJ

COOLING CRYSTALLIZATION: FROM MODELING AND CONTROL TO EXPLORING NEW POLYMORPHIC STRUCTURES

Marcellus Guedes Fernandes de Moraes

Tese de Doutorado apresentada ao Programa de Pós-graduação em Engenharia Química, COPPE, da Universidade Federal do Rio de Janeiro, como parte dos requisitos necessários à obtenção do título de Doutor em Engenharia Química.

Orientadores: Argimiro Resende Secchi
Maurício Bezerra de Souza Jr.
Paulo Laranjeira da Cunha Lage

Rio de Janeiro
Março de 2023

COOLING CRYSTALLIZATION: FROM MODELING AND CONTROL TO EXPLORING NEW POLYMORPHIC STRUCTURES

Marcellus Guedes Fernandes de Moraes

TESE SUBMETIDA AO CORPO DOCENTE DO INSTITUTO ALBERTO LUIZ COIMBRA DE PÓS-GRADUAÇÃO E PESQUISA DE ENGENHARIA (COPPE) DA UNIVERSIDADE FEDERAL DO RIO DE JANEIRO COMO PARTE DOS REQUISITOS NECESSÁRIOS PARA A OBTENÇÃO DO GRAU DE DOUTOR EM CIÊNCIAS EM ENGENHARIA QUÍMICA.

Orientadores: Argimiro Resende Secchi
Maurício Bezerra de Souza Jr.
Paulo Laranjeira da Cunha Lage

Aprovada por: Prof. Argimiro Resende Secchi
Prof. Maurício Bezerra de Souza Jr.
Prof. Paulo Laranjeira da Cunha Lage
Prof. Gabriel Gonçalves da Silva Ferreira
Prof. Carla Luciane Manske Camargo
Prof. Martha A. Grover

RIO DE JANEIRO, RJ - BRASIL
MARÇO DE 2023

de Moraes, Marcellus Guedes Fernandes

Cooling Crystallization: from Modeling and Control to Exploring New Polymorphic Structures. – Rio de Janeiro: UFRJ/COPPE, 2023.

XXIV, 157 p.: il.; 29,7 cm.

Orientadores: Argimiro Resende Secchi

Maurício Bezerra de Souza Jr.

Paulo Laranjeira da Cunha Lage

Tese (doutorado) – UFRJ/ COPPE/ Programa de Engenharia Química, 2023.

Referências Bibliográficas: p. 127-142

1. Crystallization. 2. Modeling and Control. 3. Polymorphism. 4. Praziquantel. 5. Image Analysis.

I. Secchi, Argimiro Secchi *et al.* II. Universidade Federal do Rio de Janeiro, COPPE, Programa de Engenharia Química. III. Título.

Ackowledgments

I am immensely grateful to my advisors Profs. Argimiro, Maurício and Paulo. Undoubtedly, it was an honor to have your support, advice, and guidance during this thesis. Thank you for your example, encouragement, and concern in my academic career. I hope to be able to reflect a little on what you are in my professional life, both as a teacher and researcher. Many thanks!

To my advisors in the US, Prof. Martha Grover and Allan Myerson. My "sandwiches" at Georgia Tech and MIT, respectively, were only possible and fruitful because of you. I am flattered by the opportunity to work with you and immensely grateful for all the support you gave to my formation and research.

Thanks also to Professor Ronald Rousseau for the discussions on crystallization. And to Professor Amaro for all support and advice. Thank you for also being my fourth advisor.

To Professors Heloísa Sanches, Mônica Antunes, and Verônica Calado, for, since undergraduate, always having good words of encouragement and rooting for my academic formation. To Kese, Raquel Massad, Bruno Capron, and Fabio Santos, professors and partners of "Noturno" in Escola de Química. Thanks for all your help and friendship. I want to thank Professor Papa Matar for all his receptivity and support while I was at Escola de Química as a professor.

To my undergraduates ("ICs"), especially Giovanna Mandarino and Pedro Magno, for their total competence in helping me when I needed it most – while I was working at Petrobras.

I would like to thank my family and friends for their support. To my parents, for all the efforts they have always made for my education, struggling

with all the life difficulties. Our stories are countless. I am very proud of my origin, being from the suburbs of Rio, and the value I attach to "my places" (paraphrasing Arlindo Cruz): Colégio, Irajá, and Madureira. I am very proud to be the result of the transformation from education, where everything would be much more difficult without you two. I also thank my brother, Pedro Henrique Guedes, for all the companionship and being a partner in many moments.

To my friend Amanda Soares, for all the friendship at all times together. Thank you for always supporting and being with me and for your sincere company. It's adorable to see how much you root for me, and you know it's reciprocal forever.

To Pedro Delou and (Prof.) Henrique Pacheco, for all the friendship and good times at "Escola Piloto". I really thank Fernando Lima, and I am also pleased to pass him the baton and see the continuation of this work in crystallization in our group.

To Mary, Vera Cruz e Luciana for all the help since the beginning of the thesis.

To my friends Stefani Kocevska and Youngjo Kim. Stefani, thank you for being my English teacher for the first few months, being so helpful, and supporting me with (absolutely) everything. Thank you for your friendship and good times together (and the times in NYC). Youngjo, thank you so much for all the crystallization discussions, your joy and fun times together in the office.

To my friend Ayse Eren, for her sincere friendship and all her support, both in and out of the research. For all the conversations about crystallization or not. Undoubtedly, you are already a big name in this field. Thank you so much for all the times together in Boston. To my friend Francesco Civati, for all his help in learning the experimental techniques I developed in this thesis and for all the conversations and advice in our day-to-day work at the office.

To CAPES, CNPq and Fulbright for financial support. I specially thank Carolina Martins and Taynara Ramos from Fulbright Brazil for everything. I am really proud of being a former Fulbrighter.

Resumo da Tese apresentada à COPPE/UFRJ como parte dos requisitos necessários para a obtenção do grau de Doutor em Ciências (D.Sc.)

CRISTALIZAÇÃO POR RESFRIAMENTO: DA MODELAGEM E CONTROLE À EXPLORAÇÃO DE NOVAS ESTRUTURAS POLIMÓRFICAS

Marcellus Guedes Fernandes de Moraes

Março/2023

Orientadores: Argimiro Resende Secchi
Maurício Bezerra de Souza Jr.
Paulo Laranjeira da Cunha Lage

Programa: Engenharia Química

O presente trabalho estuda a cristalização por resfriamento focando em avanços sob perspectiva da operação baseada em modelos matemáticos, bem como do auxílio no desenvolvimento de formulações farmacêuticas. Primeiramente, modelos representativos foram desenvolvidos a partir de experimentos em unidade de cristalização em batelada via análise dinâmica de imagens, incluindo a estimação de parâmetros cinéticos para os sistemas avaliados. A boa predição obtida permitiu desenvolver estratégias de controle ótimo para alcançar critérios desejados de tamanho e forma dos cristais. Além disso, metodologias de cristalização por resfriamento para investigação de formas sólidas de fármacos foram desenvolvidas, especificamente para o praziquantel, anti-helmíntico utilizado para tratamento da esquistossomose. Uma metodologia sistemática de triagem foi proposta para a investigação de polimorfos. Duas novas formas anidras e um solvato foram descobertos, e todas as formas previamente caracterizadas puderam ser obtidas pela primeira vez por cristalização por resfriamento.

Abstract of Thesis presented to COPPE/UFRJ as a partial fulfillment of the requirements for the degree of Doctor of Science (D.Sc.)

COOLING CRYSTALLIZATION: FROM MODELING AND CONTROL TO EXPLORING NEW POLYMORPHIC STRUCTURES

Marcellus Guedes Fernandes de Moraes

Março/2023

Advisors: Argimiro Resende Secchi
Maurício Bezerra de Souza Jr.
Paulo Laranjeira da Cunha Lage

Department: Chemical Engineering

The present work studies cooling crystallization, focusing on advances from the perspective of model-based operation and aiding the development of pharmaceutical formulations. First, representative mathematical models were developed from experiments in a batch crystallization unit using dynamic image analysis, including estimating kinetic parameters for the evaluated systems. The good prediction obtained by the models allowed the development of model-based optimal control strategies to make it possible to reach the desired specificity for the size and shape of the crystals. Moreover, the development of cooling crystallization methodologies to investigate solid forms of drugs was obtained, specifically for praziquantel, an anthelmintic used against schistosomiasis. A systematic screening methodology was proposed for the polymorph investigation. Two new anhydrous forms and one solvate were discovered, and all previously characterized forms could be obtained for the first time via cooling crystallization.

Contents

List of Figures

Figure 3.8 - KDP crystal and the characteristics lengths.....60

Figure 3.9 - Relative dissolution rate of KDP.....68

Figure 3.10 - Precited and experimental values for supersaturation zone experiment: characteristic mean lengths (left), zeroth order cross-moment (middle) and supersaturation (right). Black lines represent the values predicted by the model.....71

Figure 3.11 - Simulation results for optimal control of KDP. Above: state trajectories (left); Euclidean distance to target (right). Below: supersaturation optimal control actions (left); temperature policies calculated by supersaturation policies (right).....73

Figure 3.12 - L_1 x L_2 plot. Changes in trajectory slope indicate that aspect ratio changes. Targets are in green. Some scale representations of KDP crystals at different positions in space are shown.....74

Figure 3.13 – Coefficients of variation CV_1 and CV_2 throughout the runs for the optimal control of KDP.....75

Figure 4.1 - PXRD pattern for PZQ-DMA and comparison with Forms A, B, and C.....,,,

List of Tables

List of Symbols

a	conductivity parameter [-]
A_1	conductivity parameter $[mS\ cm^2/\ g\ ℃]$
A_2	conductivity parameter $[mS\ cm^2/\ g]$
AR	aspect ratio [-]
b	nucleation supersaturation exponent [-]
B	nucleation rate $[(min \cdot cm^3\ )^{-1}]$
$\boldsymbol{B}$	sensitivity matrix
C	solute concentration [g/L]
C_s	solute equilibrium concentration [g/L]
CV	coefficient of variation [-]
d_{F^-}	minimum Feret diameter $[\mu m]$
d_{F^+}	maximum Feret diameter $[\mu m]$
D_1	dissolution rate in L_1 $[cm/min]$
D_2	dissolution rate in L_2 $[cm/min]$
D_{rel}	relative dissolution rate [-]
E_{Ab}	nucleation activation energy $[J/mol]$
E_{Ag}	growth activation energy $[J/mol]$
g	growth exponent parameter [-]
G	growth rate $[\mu m/min]$
G_1	growth rate in L_1 $[cm/min]$
G_2	growth rate in L_2 $[cm/min]$
L	crystal size $[\mu m]$
L_0	nuclei size $[\mu m]$

L_1	characteristic length (width) for KDP $[\mu m]$
L_2	characteristic length (length) for KDP $[\mu m]$
$\bar{L}_n$	number-average crystal size
M_j	jth-order moments of distribution ν $[\mu m^j]$
M_T	mass of crystals per solvent volume $[g/cm^3]$
$n(L,t)$	monovariate number density distribution $[(\mu m\,.\,cm^3)^{-1}]$
$n(L_1,L_2,t)$	bivariate number density distribution $[(\mu m^2\,.\,cm^3)^{-1}]$
$n_{L_1}(L_1,t)$	marginal density distribution $[(\mu m\,.\,cm^3)^{-1}]$
n_s	number density distribution of the seeds $[(\mu m\,.\,cm^3)^{-1}]$
N_d	number of particles that leave the domain [-]
R	the universal gas constant $[J/mol\,K]$
$\boldsymbol{R_\theta}$	parameter correlation matrix
${s_R}^2$	residual variance [-]
S	relative supersaturation [-]
T_f	melting point [℃]
T_r	transition temperature [℃]
$\dot{V}$	volumetric flow rate in the sampling loop $[cm^3/min]$
V_c	volume of a single crystal $[cm^3]$
$V_{solution}$	volume of solution (free of solids) $[cm^3]$
$V_{suspension}$	volume of suspension $[cm^3]$
$\boldsymbol{V}_y$	measurement covariance matrix
k_V	volume shape fator
k_b	nucleation constant
k_g	growth rate constant $[(\mu m/min\,)(\,L/\mathrm{g})^g]$
x_p	PZQ molar fraction [-]
β	nucleation third moment exponent [-]
$\delta(\cdot)$	Dirac delta

ΔC	absolute supersaturation [g/L]
Δg_{ps}	binary interaction coefficient $[J/mol]$
Δg_{sp}	binary interaction coefficient $[J/mol]$
ΔH_f	enthalpy of fusion $[kJ/mol]$
γ	size-dependent growth constant [-]
γ_p	PZQ activity coefficient [-]
	$[(min \cdot cm^3)^{-1}(L/\mathrm{g})^b(cm^3/\mu m^3)^\beta]$
κ	conductivity [mS/cm]
μ_j	j$^{\text{th}}$-order moment of distribution n $[\mu m^j/cm^3]$
$\Omega(\theta)$	objective function of PBM's parameter estimation
θ	model parameter vector
ϑ	volume fraction of the total crystal population

List of Abbreviations

AA	Acetic Acid
API	Active Pharmaceutical Ingredient
BPTT	BackPropagation Through Time
CLD	Chord Length Distribution
CSD	Crystal Size Distribution
DMA	Dimethylacetamide
DSC	Differential scanning calorimetry
ESN	Echo State Network
ESN-NMPC	Echo State Network – Nonlinear Model Predictive Controller
FBRM	Focused Beam Reflectance Measurement
IPOPT	Interior Point OPTimizer
KDP	Potassium dihydrogen phosphate
KF	Karl Fischer
MSZW	Metastable Zone Width
MLP	MultiLayer Perceptron
MPC	Model Predictive Control
NMPC	Nonlinear Model Predictive Control
NWCC	Non-Weighted Chord Counts
PBM	Population Balance Model
PB-NMPC	Population Balance – Nonlinear Model Predictive Controller
PXRD	Powder X-ray diffraction
PZQ	Praziquantel

PZQ-AA	Praziquantel acetic acid solvate
PZQ-DMA	Praziquantel Dimethylacetamide solvate
PZQ-HH	Praziquantel hemihydrate 1
PZQ-HH2	Praziquantel hemihydrate 2
SEM	Scanning Electron Microscopy
SQP	Successive Quadratic Programming
SWCC	Square-Weighted Chord Counts
SWMCL	Square-Weighted Mean Chord Length
WHO	World Health Organization

Chapter 1

Introduction

1.1 Contextualization

Crystallization is a unit operation crucial for the many sectors of the industry, such as chemicals, agrochemicals, pharmaceuticals, and food[1,2]. More than 90% of active ingredients are produced in the pharmaceutical field as crystals[3]. The crystallizer purifies and separates the products of an industrial process. Different approaches exist for a crystallization process include evaporation, reaction, antisolvent addition, and cooling[4].

First, for the proper prediction of the final product quality obtained in industrial crystallization processes, more detailed knowledge about the size of the crystals is necessary. For this, modeling via population balance is the most used approach for crystallization processes[5-7], in which the population balance equation must be solved.

Using a one-dimensional crystal size distribution (CSD) is the most widespread way to model and control crystal size in crystallization processes[8]. Population Balance Model (PBMs) for crystallization processes are frequently used in the literature with three main objectives[8]: to estimate parameters for the kinetic model for the involved phenomena, to predict particle size and shape using such kinetic model, and, finally, to optimize the process conditions for the required product specification.

PBMs were proven to be effective for the design and control of crystallization processes[9]. Usually, using a PBM is accompanied by a numerical solution to simulate the process[10,11], which can be followed by estimating model parameters based on experimental data. Many works in the literature used PBMs to obtain the kinetic model parameters for the phenomena involved in the process, especially examining the kinetics of primary nucleation, secondary nucleation, and particle growth[12-27]. A sequential approach to estimating the kinetic model parameters is presented by Calvo et al.[25]. The solute concentration is the most common and necessary measured variable, usually obtained from in situ spectroscopic techniques[28] or from measuring another property such as conductivity[29] or solution density[30]. Offline measurements of the crystal size distribution traditionally characterize the solid phase[17,21,31].

Recently, the literature has reported significant progress regarding online crystal phase information. In situ techniques, such as focused beam reflectance measurements (FBRM) and image analysis from Mettler Toledo's PVM and EasyViewer or the Blaze Metrics' Blaze systems[32], usually require great computational effort and investment in models that are capable of providing a good approximation of the real CSD, still being a challenge in some applications[7,33]. Regarding using FBRM, which measures the chord length distribution (CLD), some relationships between the CLD and CSD were developed[34], but with limited direct application in parameter estimation[12,35,36]. Szilagyi and Nagy directly compared experimental CLD with that obtained from PBM by artificial neural network soft sensors[37]. Recent studies applied the FBRM data directly in the parameter estimation framework without further transformations by maximizing the correlation between the predicted crystal number density and the measured FBRM counts[38,39].

Online image analysis via ex-situ imaging setup has been gaining prominence in several applications, using a flow-through cell setup[40,41] and commercial online imaging tools (e.g., Sympatec QICPIC) to evaluate

crystallization kinetics[42-44], agglomeration[45], and optimal control[46]. More recently, the use of microcomputed tomography to obtain three-dimensional images of potash alum has been reported[47].

In addition to the concern with particle size, shape modeling (crystalline habit) is shown to be necessary and increasingly used in the development of predictive models and control of crystallization processes. Growing research started in the 2000s[48,49] is observed in the literature for designing PBMs with internal variables that represent the morphology of crystals.

In the pharmaceutical industry, crystallization plays a crucial role, since the products, without their great majority, consist of solid materials of high purity, being dominant in almost all processes. In this case, engineering focuses on how the crystals' size and shape affect the process – specifically on their processability – and how these characteristics affect the bioavailability of active pharmaceutical ingredients (APIs). Product specification in terms of its morphology has also gained prominence in recent years for APIs[50]. For the crystallization of pharmaceuticals, achieving the specification criteria for size, shape, and yield may be directly related to the presence of more than one crystalline arrangement (polymorphism) and chirality of certain compounds, such phenomena being intrinsic to each studied system, expressively present in APIs.

A significant challenge in developing pharmaceutical formulations is the low bioavailability due to the low water solubility of many active pharmaceutical ingredients (APIs)[51]. Thus, searching for new solid forms capable of improving solubility and reducing the therapeutic dose becomes relevant[52]. Polymorphism is the ability of a compound to exist in more than one crystalline form, with different structures and packing ways[51-53]. These structural differences can result in very different physical and chemical properties, and polymorphic research is of great interest, especially for developing new formulations and drug candidates[51,54].

Praziquantel (PZQ) is a racemic compound and an anthelmintic API prescribed for treating schistosomiasis. It is administered in high dosages mainly

due to the low water solubility and extensive first-pass metabolism[55]. PZQ is included in the list of essential drugs of the World Health Organization (WHO)[56], recommended for all known forms of the disease. Schistosomiasis is a chronic disease strongly linked to poverty that affects more than 240 million people. It is also classified as a neglected tropical disease precisely because it affects the poorest and most vulnerable populations, contributing to the perpetuation of poverty and social inequality and impacting child health[57,58]. In endemic areas, schistosomiasis is the second most prevalent disease in socioeconomic and public health terms, surpassed only by malaria[59,60].

Investments in research applied to neglected diseases are low, not directly reflecting the development and accessibility to medicines and new technologies for prevention and control. In a brief context about schistosomiasis, according to WHO, it is estimated that 700 million people live in endemic areas, prevailing tropical and subtropical regions such as Brazil[56]. In these regions, schistosomiasis is the second most important disease in socioeconomic and public health, surpassed only by malaria[60].

Brazil is the most affected in the Americas, with 19 states comprising the endemic area. Estimates for the exposed and parasitized populations are around 26 and 8 million, respectively. The regions with the highest cases are the northeast and southeast.[57] Schistosomiasis in adults has a low mortality rate, although the debilitating effects are significant. The primary concern is the contraction by preschool-age children with a higher risk of morbidity for the disease.

The primary investigation of new solid forms of praziquantel involved obtaining cocrystals of carboxylic acids[61-65] and using polymorph screening by mechanochemistry[66-71]. The pure enantiomers of praziquantel are reported as hemihydrates, indexes under the codes SIGBUG (S-praziquantel hemihydrate)[72], SIGBUG01 (R-praziquantel hemihydrate)[73], and LIFVED (R-praziquantel monohydrate)[74]. Table 1.1 summarizes the literature survey for all reported polymorphs of PZQ (also considering the solvates).

Table 1.1 - Reported polymorphs of PZQ.

Racemic PZQ			
Form	**Method**	**Type**	**Ref. code**
A	Commercial	Anhydrous	TELCEU[63]
B	Neat grinding	Anhydrous	TELCEU01[68]
C	Neat grinding	Anhydrous	GOYZOM[69]
D	Neat grinding	Anhydrous	not indexed[66]
E	Liquid assisted grinding (THF)	Not reported	not indexed[66]
F	Amorphous	Anhydrous	not indexed[66]
PZQ-MH	Cooling from melting	Monohydrate	not indexed[67]
PZQ-HH	Neat grinding	Hemihydrate	WUHQAU[70]
PZQ-AA	Liquid assisted grinding	Solvate (acetic acid)	DAJCEA[71]
PZQ-2P	Liquid assisted grinding	Solvate (2-pyrrolidone)	DAJCA[71]
-	Liquid assisted grinding	Hydrate	not indexed[86]
PZQ pure enantiomers			
Type			**Ref. code**
S-PZQ hemihydrate			SIGBUG[72]
R-PZQ hemihydrate			SIGBUG01[73]
R-PZQ monohydrate			LIVFED[74]

Solution crystallization is a commonly used method to access different solid-state forms of one substance. Several works in the literature focus on

obtaining and transforming metastable forms and determining their relationship with the choice of solvent, supersaturation level, temperature, and cooling rate[75-82]. Rapid cooling crystallization is also preferred to favor the nucleation of metastable forms[75,78]. Fast cooling crystallization is still important even for highly polymorphic compounds already well explored in the literature. We can highlight this technique's recent discovery of the ninth form of tolfenamic acid[83]. Furthermore, high and medium throughput techniques using cooling crystallization have been established as a suitable method for polymorph screening[75,76,84,85].

Given the above, obtaining appropriate models and control strategies for cooling crystallization processes that deal with the size and shape of the crystals is significant to developing new technologies. Allied with this process concern, the polymorph investigation from a product perspective is crucial for APIs. In this thesis, we addressed both aspects and their respective contributions.

1.2 Objectives and Contributions

The work has a scope that contributes to modeling and control aspects and experimental aspects in cooling crystallization processes. In this way, the main contributions of this thesis relate to advances in cooling crystallization from the point of view of operation for product quality, such as product development. These advances came from developing mathematical models to enhance the process understanding and optimal control to meet critical quality criteria and by identifying polymorphs under different experimental conditions.

This thesis had the following objectives.

I. Develop representative modeling and control schemes that can be applied to the size and shape of crystals in batch processes. For this, a theoretical-experimental interface was used based on PBM and data

obtained experimentally in the crystallization apparatus of the present group using a dynamic image analyzer for the crystal phase information. As specific contributions, the following stand out.

a. Using ex-situ image analysis as a suitable tool for the solid phase characterization, providing validated phenomenological modeling for the cooling crystallization of potassium sulfate (K_2SO_4) and potassium dihydrogen phosphate (KDP).
b. Model parameter estimation included measurements of all moments of the crystal size distribution that appear in the model equations.
c. Use of a linear size-dependent growth rate for potassium sulfate in water, which still needed to be fully established.
d. The development of an optimal control framework for the crystal size and coefficient of variation using a monovariate population balance modeling for K_2SO_4.
e. The development of an optimal control framework for the crystal size and shape using a bivariate population balance modeling for KDP, considering operation in supersaturated and undersaturated conditions.

II. investigate the polymorphism of praziquantel using cooling crystallization experiments under different conditions not explored in the literature for this drug to access different solid forms. Specific contributions are:

a. the discovery of 2 anhydrous new polymorphs of praziquantel, and a dimethylacetamide solvate;
b. the determination of solubility data of praziquantel in different solvents by solvent screening method, providing solid-liquid equilibrium equations for the systems studied;

c. the development of an effective systematic methodology to screen polymorphs using cooling crystallization;
d. the importance of solvent selection and variation in the rate of supersaturation generation to access different forms, even those obtained from more complicated techniques as well as finding new polymorphs;
e. the relevance of finding novel solvates, as this can lead to unidentified phases when desolvation occurs.

1.3 Thesis Structure

Given the diversity of topics addressed during the development of this thesis, the thesis was structured based on articles in the following chapters. This work is divided into five chapters.

Chapter 1 (this chapter) presents the developed studies' context, motivation, and objectives.

Chapter 2 addresses the modeling of cooling crystallization using ex-situ image analysis to get information about the solid phase. This chapter discusses aspects of the experimental apparatus used and describes the data processing and the experimental procedure. In this chapter, phenomenological modeling is applied to the crystallization of potassium sulfate in water, in which kinetic parameters and details on the estimation and construction of confidence regions are presented.

In **Chapter 3**, the developed applications of optimal control to different cases of crystallization are presented. Section 3.1 presents the application of open-loop supersaturation control applied to potassium sulfate crystallization. In Section 3.2, the application of neural networks is addressed. Section 3.3 presents the optimal size and shape control applied to KDP crystallization and the modeling used for the model-based control scheme.

Chapters 4 and **5** refers to the praziquantel cooling crystallization. **Chapters 4** addresses the investigation of the polymorphism of praziquantel exploited through cooling crystallization. This study applied different conditions and techniques, showing the vital role of cooling crystallization in accessing polymorphs allowing access to other solid forms, and discovering new ones.

In **Chapter 5**, the results obtained up to the present moment for the crystallization of praziquantel are presented and discussed. First, the determination of praziquantel solubility in different organic solvents was explored to validate experimental methodology with solvent screening for solubility determination and subsequent analysis of the crystallization process. Second, the preliminary investigation of the batch cooling crystallization of praziquantel is presented, highlighting essential points about the operation of the process via in-situ image analysis monitoring.

Chapter 6 summarizes the conclusions from the results and discussions presented in the previous chapters and suggests future directions related to the developments obtained in this thesis.

Chapter 2

Modeling of Cooling Crystallization using Ex-Situ Image Analysis

This chapter presents the modeling of batch-cooling crystallization based on online dynamic image analysis. A flow-through microscope was used to track the temporal evolution of the crystal population. A population balance modeling (PBM) approach, parameter estimation, and validation were obtained for the batch-cooling crystallization of potassium sulfate in water. The performed experiments provided new experimental data, giving dynamic information about the crystal size throughout each run. The kinetic model parameters for crystal nucleation and growth were estimated using a hybrid optimization algorithm, followed by the confidence region construction using a more exploratory particle swarm algorithm. In the parameter estimation framework, in addition to solute concentration, the first four lower order moments computed throughout all experiments were included in the objective function. A size-dependent linear growth rate was found to capture well the dynamics of the potassium sulfate crystal-size distribution. The experimental results evidenced that the crystal shape of potassium sulfate is predominantly constant, allowing the adequacy of the developed model. The chapter was adapted from the following paper recently submitted as a research article to Industrial & Engineering Chemistry Research:

i. de Moraes, M. G. F.; Lima, F. A. R. D; Lage, P. L. C.; de Souza Jr., M. B.; Barreto Jr., A. G; Secchi, Ag. R. Modeling and Predictive Control of Cooling Crystallization by Dynamic Image Analysis: Exploring Population Balance Model and Machine Learning Approaches.

2.1 Introduction

Specifically for the crystallization of potassium sulfate, Mullin and Gaska evaluated the particle growth of potassium sulfate in a fluidized bed crystallizer[87]. The authors studied the effect of crystal size at 20 °C, noting that the potassium sulfate's growth rate (G) is clearly size dependent, expressed by $G \propto L^{0.6}$ (L is the crystal size in µm). Randolph and Rajagopal fit experimental data of potassium sulfate using McCabe's ΔL law in a continuous mixed-suspension crystallizer as only dependent on the supersaturation level[88].

Randolph and Cise correlated experimental data from mixed-suspension mixed-product removal (MSMPR) experiments of potassium sulfate in water and observed the growth rate markedly size-dependent[89]. They proposed an expression in which $G \propto \exp(-k/L^{1/2})$, but with poor correlation ($R^2 = 0.425$).

Jones et al. and Budz et al. showed that experimental data using an MSMPR crystallizer fit a growth rate in which $G \propto (1 + 2L^{2/3})$ for crystals greater than 20 µm[90,91]. This dependency was later used by Jones et al. for the investigation of operational conditions to improve solid-liquid separation of potassium sulfate in a batch crystallizer[92]. Chianese et al. used the same size-dependent expression ($G \propto (1 + 2L^{2/3})$) to fit their data obtained from seeded batch crystallization experiments[93]. Thus, this dependency is the most used in the literature, but the works point out a good approximation for crystals larger than 100 µm, with no general agreement for crystals smaller than 20 µm in the studies carried out so far[90].

Omar and Ulrich studied the effect of crystal size in a fluidized bed crystallizer of potassium sulfate in water[94]. They correlated the crystal size according to an expression where $G \propto L^{1.01}$. However, this limited study evaluated only two supersaturation levels and four crystal size values in the [200,600] µm size range. Thus, there has yet to be a general agreement on the size-dependent growth rate of potassium sulfate in water, especially for crystals smaller than 100 micra.

In addition, works involving simulation and optimal control for potassium sulfate use the model presented by Rawlings, where the growth rate is independent of size[95], which does not reflect the experimental observations for the description of the growth rate of potassium sulfate. That work was used as a benchmark in other works to evaluate optimization and nonlinear control[96,97] and predictive control strategies[98].

This work's first objective is to develop representative phenomenological modeling for the cooling crystallization of potassium sulfate in water. This process was revisited using online measurements from dynamic image analysis and electrical conductivity. A new experimental dataset was obtained, composed of dynamic information about the crystal size distribution and concentration throughout each experiment. The kinetic model parameters for nucleation and growth rates were estimated to predict the process dynamics. The confidence regions of the parameters were built using a more exploratory particle swarm optimization algorithm and later compared with the elliptical approximation. The obtained model was validated against other experiments to establish a digital twin for this process.

The present work also proposes a new expression for the growth rate of potassium sulfate in water, in which the linear dependence $G \propto (1 + \gamma L)$ represents well the experimental data obtained for systems with the presence of smaller crystals.

2.2 Experimental Section

2.2.1 Materials and experimental setup

Potassium sulfate (purity of 99%) was purchased from Synth and represented the substance used for the investigations in this work. Fresh distilled water was used as the solvent in all experiments. The crystallization setup (scheme in Figure 1) consisted of a 1 L crystallizer vessel (Syrris®) stirred by a two-bladed stirrer (Orb®). The conductivity was determined using the SevenCompact™ Duo S213 (Mettler Toledo), connected to the Inlab® 731 (Mettler Toledo) conductivity sensor for monitoring the liquid phase. The monitoring of the solid phase took place using the image analyzer QICPIC (Sympatec GmbH, Germany) supplied with the LIXELL accessory (Sympatec GmbH, Germany), in which real-time images of the suspension were acquired.

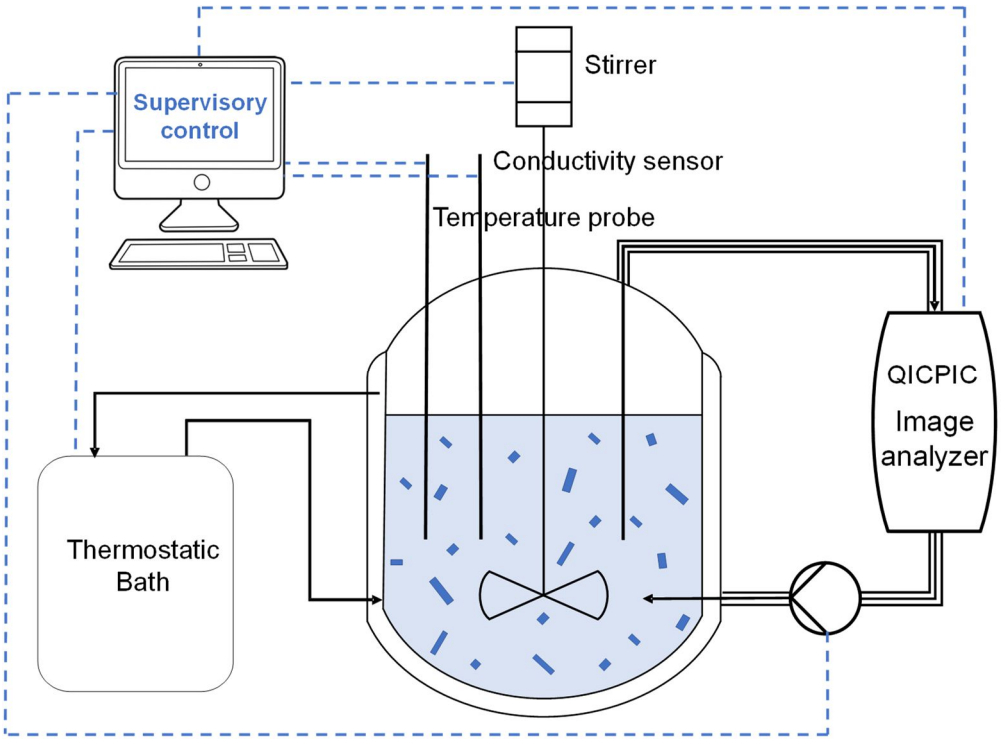

Figure 2. 1 - Experimental setup for the crystallization experiments

The image analyzer was located in an ex-situ sampling loop in a tube with an inner diameter of 5 mm, in which continuous withdrawal from the vessel through the analyzer was provided by a peristaltic pump (Masterflex L/S) at a constant flow rate of 140 cm^3/min. The peristaltic pump was installed downstream of the image analyzer to minimize the sample mischaracterization and better represent the state removed from the vessel. The sample passed through a 500 µm-thickness cell, generating a thin layer of suspension that eliminated from the measurement the interference of crystals in different planes depths.

A PT100 thermocouple was used to measure the solution temperature. The thermostatic bath (Huber® Petite Fleur) was connected to the vessel's cooling jacket for temperature control.

2.2.2 Seeds preparation

The seeds were prepared by fast cooling (2 °C/min) recrystallization of the commercial potassium sulfate. A saturated solution at 50 °C was prepared at 60 °C to ensure complete dissolution. The solution was cooled to 50 °C and kept at this temperature for 30 minutes when cooling started. As soon as the particle count in QICPIC showed an expressive increase due to nucleation, also indicated by fine crystals in suspension, the experiment continued for 15 minutes to enable the growth of new nuclei. After that, the suspension was filtered using a vacuum filter. The filtered crystals were washed with acetone and dried at 45°C in a vacuum oven overnight. The product was then manually sieved, and crystals between the 38 µm and 53 µm sieves (400 and 270 Mesh Tyler, respectively) were collected and used as seeds for all experiments.

2.2.3 Data processing

The WINDOX Sympatec® software allowed real-time monitoring and data processing of the images. The QICPIC image analyzer continuously took videos

from the suspension at 100 frames per second. Figure 2.2 illustrates typical frames obtained at different times of an experimental run.

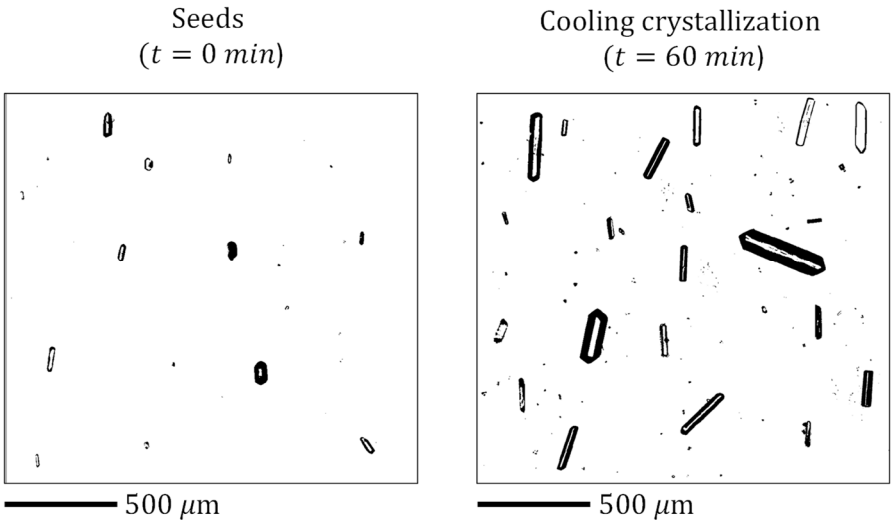

Figure 2. 2 - Experimental setup for the crystallization experiments

Data were acquired continuously. At each minute, all particles detected during the last minute (sampling time) had their size and shape information stored in a "particle gallery" In this work, the Feret diameter was used to represent the size of the particles. The maximum (d_{F^+}) and minimum (d_{F^-}) Feret diameters are determined being the greatest and smallest distance possibly measured when tracing two parallel planes that will tangent a given particle, as illustrated in Figure 2.3.

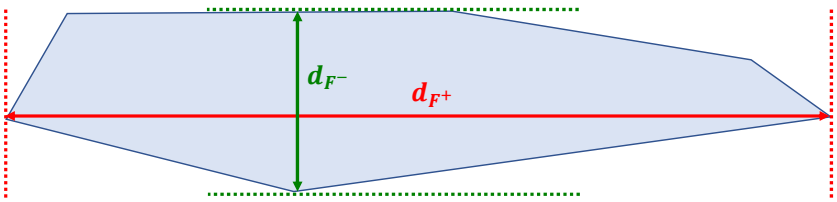

Figure 2. 3 - Illustration of the maximum and minimum Feret diameter (d_{F^+} and d_{F^-}).

As potassium sulfate crystals have a regular shape (rods), the measurement of d_{F+} and d_{F-} proved adequate to characterize the crystals. For the characteristic size for the one-dimensional modeling, we adopt the arithmetic average Feret diameter (d_F), between these two. This assumption is corroborated by the crystals' aspect ratio being approximately constant in the evaluated conditions (see Section 2.6.1).

Notably, breakage and aggregation phenomena were not observed through the images during the experiments. Agglomeration for potassium sulfate is predominant only for longer batch times (e.g. 2h), which did not correspond to the cases studied for modeling. As an illustration, Figure 2.4 shows frames after 2 hours of batching, in which agglomerates formed.

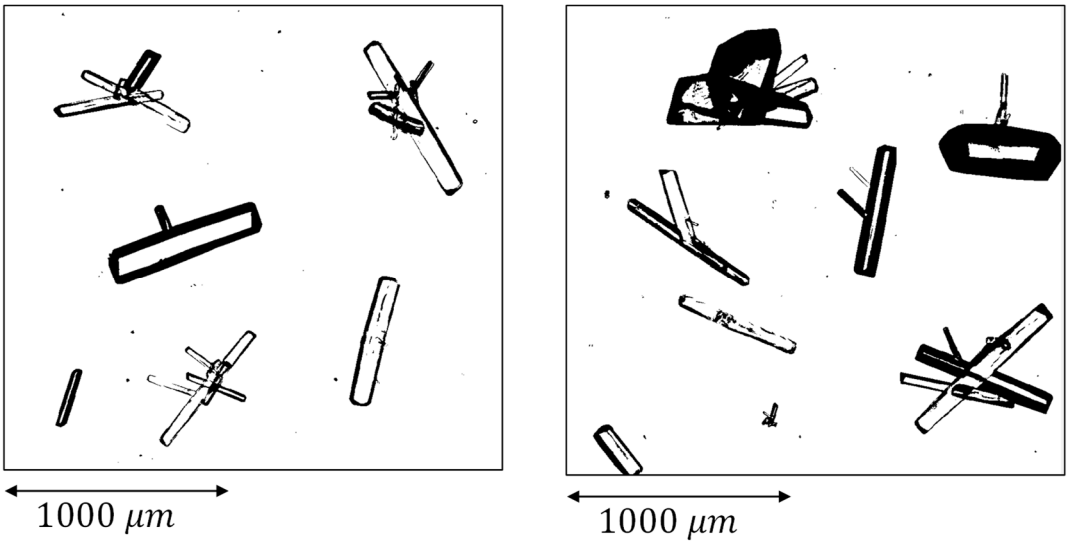

Figure 2.4 - Images from longer-lasting experiments (greater than 2h), showing agglomerates' formation.

For mathematical modeling of the process using equations of moments (see Section 2.6.2), the first four moments of the CSD were computed based on d_F in all sampling times. Using all particles analyzed during the sampling interval, Δt, moments of order j, M_j, were calculated by

$$M_j(\Delta t) = \sum_{i=1}^{N} (\bar{L}_i)^j \, v(\bar{L}_i, \Delta t) \, \left(L_{i,u} - L_{i,l}\right) \quad , \quad j = 0,1,2,3 \tag{2.1}$$

where L is the particle size, adopted as d_F $[\mu m]$, N is the number of bins, and $L_{i,l}$ and $L_{i,u}$ are the lower and upper limit of the particle size interval for each bin, respectively. In Eq. 2.1, $\bar{L}_i$ is the arithmetic average between $L_{i,l}$ and $L_{i,u}$ and $v(\bar{L}_i, \Delta t)$ represents the sample number density distribution $[\mu m^{-1}]$ of the particles analyzed from $t - \Delta t$ to t with size between $L_{i,l}$ and $L_{i,u}$.

The bin interval $\left(L_{i,l} - L_{i,u}\right)$ varies according to the following progression:

$$L_{i+1,u} = \frac{L_{i,u}}{L_{i,l}} \tag{2.2}$$

where $L_{i+1,l} = L_{i,u}$. The analyzer can detect crystals of size above 1.6 μm. The limits for the first bin containing the smallest particles to be analyzed, $L_{1,l}$ and $L_{1,u}$, are defined by the software as 1.6 μm and 1.7 μm, respectively. The number of bins and, consequently, the particles' size range computed during a given Δt vary according to the largest particle detected.

The number density distribution $n(L, t)$, expressed as number of particles per size per suspension volume, in $[(\mu m \, . \, cm^3 \; of \; suspension)^{-1}]$, was related to $v(L, \Delta t)$ as

$$n(L, t) \approx \frac{v(L, \Delta t)}{\Delta t \, \dot{V}} \tag{2.3}$$

where $\dot{V}$ is the volumetric suspension flow rate in the sampling loop. The moments μ_j of $n(L, t)$ are defined as

$$\mu_j(t) = \int_0^{\infty} L^j \, n(L, t) \, dL \tag{2.4}$$

in $[\mu m^j \,.\, cm^{-3}\ of\ suspension]$. Based on Eq. 2.3, and approximating the integral by the summatory established in Eq. 2.1 , $\mu_j(t)$ were calculated as

$$\mu_j(t) = \frac{M_j(\Delta t)}{\Delta t\, \dot{V}} \tag{2.5}$$

The solute concentration was determined from the conductivity data acquired during the same sampling time using a calibration model that relates the solute concentration with the conductivity and temperature.

Zhang et al. proposed the following semiempirical conductivity model to correlate conductivity (κ), temperature (T), and mass concentration (C) of electrolyte solutions[99]:

$$\kappa(C,T) = (P_1 T + P_2) C^n \exp\left(-\frac{P_3 C}{T - P_4}\right) \tag{2.6}$$

where the 5 parameters $n, P_1, P_2, P_3,$ and P_4 can be estimated for each system electrolyte-solvent. Firstly, Eq. 2.6 was used to obtain the correlation between experimental data for the conductivity of K_2SO_4 in water. It was observed that the last term on the right side of Eq. 2.6 is approximately constant for the system and conditions studied. With that, and together with the fact that a more appropriate expression would be one that made it possible to explicitly obtain $C = f(\kappa, T)$:

$$C(\kappa,T) = \left(\frac{\kappa}{A_1 T + A_2}\right)^a \tag{2.7}$$

Eq. 2.7, therefore, is the equation proposed in this work for the calibration model for solute (K_2SO_4) concentration. Eq. 2.7 can be expressed in logarithmic form as

$$\ln C = a \ln \kappa - a \ln(A_1 T + A_2) \tag{2.8}$$

where κ is expressed in mS/cm; C in g/cm^3; T in ℃.

Calibration was obtained for the concentration and temperature range employed during the crystallization experiments. For this, supersaturated solutions were prepared to cover a region with a supersaturation level close to those performed experimentally. Fewer calibration points were obtained for lower temperatures due to the possibility of nucleation in higher concentrations at those temperatures. Calibration took place in the same apparatus used for the experiments, with the conductivity sensor placed in the same position as during the experiments. Image analysis through QICPIC was obtained to ensure the non-formation of crystals during the process.

The amount of K_2SO_4 added for each determination was weighed on an analytical balance, and the volume of water was measured using volumetric flasks. The stir rate was 500 rpm. For each experimental point, the solution was heated 20 °C above the desired value for the determination to ensure complete dissolution and then returned to the desired value, equilibrating for 40 minutes.

For the supersaturation experiments, the temperature was reduced to the appropriate value by performing a cooling ramp at a rate of -1.0 °C/min to avoid crystallization caused by a sudden change in temperature .

The parameters $a, A_1,$ and A_2 in Eq. 2.7 were estimated from the calibration experimental data, κ $[mS/cm]$, C [g/cm^3], T [℃]. Figure 2.5 presents the experimental data (black dots) on a log-log-scale, compared to the values calculated by the model.

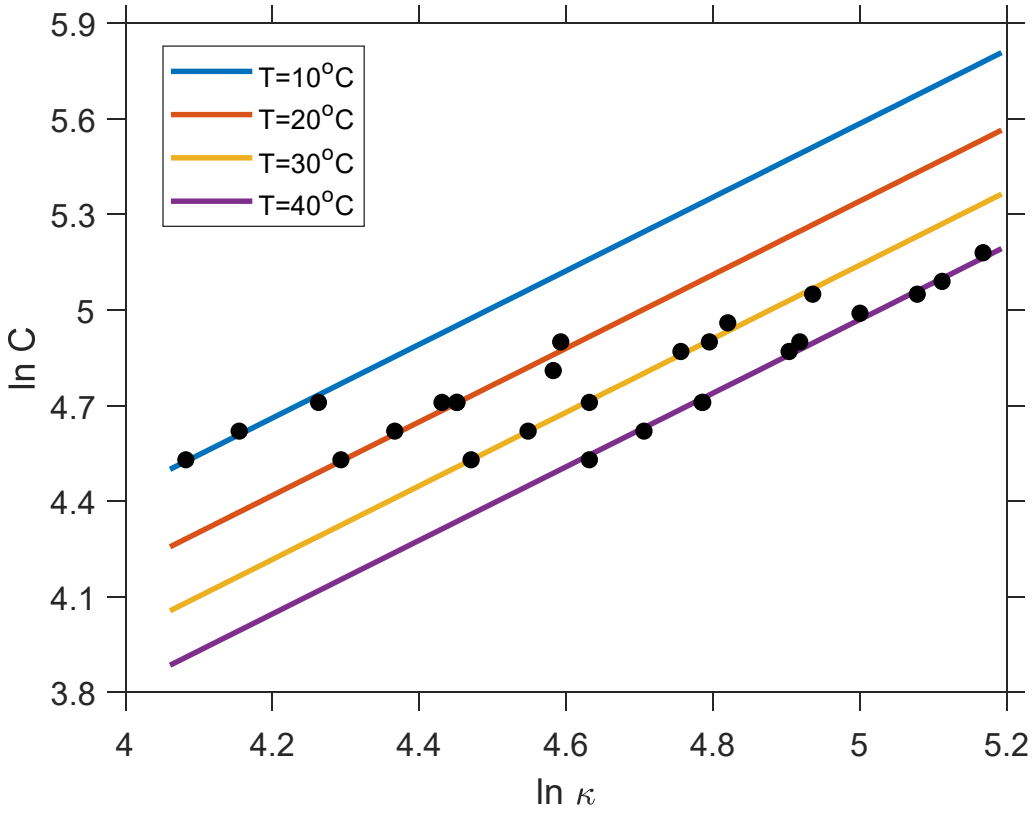

Figure 2. 5 - Calibration curves in different temperatures expressing $C[g/cm^3]$ as a function of $\kappa[mS/cm]$ and $T[℃]$ *($R^2 = 0.9956$).*

Table 2.1 shows the calibration, where a coefficient of determination $R^2 = 0.9956$ was obtained for the experimental and predicted concentrations.

Table 2.1 - Estimated parameters of the calibration model in Eq. 2.7

Parameter	Unit	Value
a	$[-]$	1.155497
A_1	$[\,mS\ cm^2/\ g\ ℃]$	0.027677
A_2	$[\,mS\ cm^2/\ g\ ]$	0.903823

2.2.4 Experimental procedure

The procedure of the experiments of seeded batch crystallization was as follows. First, the conductivity and temperature sensors were positioned in the empty, clean vessel. Then, the solvent (water) was introduced, starting the circulation pump and stirrer. The amount of potassium sulfate was added to the vessel, followed by the amount of water to complete the solution volume to 1L. The solution was heated to 15 degrees above each experiment's starting temperature to ensure complete dissolution. The proper absence of particles or contaminates was detected by analyzing live images in the QICPIC software. The temperature was then reduced to the starting temperature of each experiment and maintained for 30 minutes for equilibration. Each run was started seeds' loading, accompanied by the start of the cooling policy. Table 2.2 lists the experimental conditions that were kept fixed in all experiments.

Table 2.2 - Experimental conditions common to all batch crystallization runs

Condition	Value
Stir rate	400 rpm
Sampling loop flow rate	140 cm^3 / min
Mass of seeds	0.25 g
Seeds size	38 – 53 μm (sieved)
Volume of solvent	1L

Table 2.3 summarizes the experimental conditions used for each run, where "C" indicates the calibration experiments, and "V" validation experiments used to evaluate the model prediction performance in the parameter estimation (see Section 2. 3). Experiments Exp4, Exp5, and Exp6 are triplicates.

Table 2.3 - Experiments performed with the corresponding conditions

Experiment	Type*	Initial Temperature (°C)	Cooling rate (°C/min)	Final Temperature (°C)	Initial Concentration (g/cm^3)
Exp1	C	40	0	40	0.16
Exp2	V	40	0.125	32	0.16
Exp3	C	40	0.166	30	0.16
Exp4	C	40	0.25	25	0.16
Exp5	C	40	0.25	25	0.16
Exp6	C	40	0.25	25	0.16
Exp7	V	40	0.5	22	0.16
Exp8	C	30	0	30	0.14
Exp9	V	30	0.166	20	0.14
Exp10	C	30	0.25	20	0.14

* Related to the parameter estimation on Section 3

2.3 Population Balance Modeling

2.3.1 Moment equations and crystallization kinetics

To describe the crystal population by its number density based on the suspension volume, $n(L,t)$, the population balance equation applied to the batch crystallizer in supersaturated conditions yields[100]:

$$\frac{\partial n}{\partial t} + \frac{\partial (G\, n)}{\partial L} = 0 \tag{2.9}$$

A size-dependent growth rate $G(L)[\mu m/min]$ was considered in this work and is described by:

$$G(L) = G_0(1 + \gamma L) \tag{2.10}$$

The rate G_0 $[\mu m/min]$ express the temperature and supersaturation-dependent factor:

$$G_0 = k_g \, exp\left(\frac{-E_{Ag}}{RT}\right) \Delta C^g \tag{2.11}$$

where k_g is the growth rate constant $[(\mu m/min\,)(L\ of\ solution/\mathrm{g})^g]$; E_{Ag} is the growth activation energy $[J/mol]$; R is the universal gas constant; and g is the growth exponent parameter $[-]$; The absolute supersaturation is $\Delta C = C - C_s$ $[\mathrm{g}/L\ of\ solution]$, where C_s is the solute equilibrium concentration. The choice of ΔC to represent the supersaturation was made due to its use in previous works for potassium sulfate[87-89].

A temperature dependent correlation for C_s $[\mathrm{g}/L\ of\ solution]$ was obtained from solubility experimental data of K_2SO_4 in water[101] $(0°C < T < 100℃)$. The best correlation was the following quadratic equation $(R^2 = 0.9997)$:

$$C_s(T)\ [g/L] = -686.27 + 3.5795\,T - 2.9287 \times 10^{-3}\,T^2 \tag{2.12}$$

T in K. The boundary and initial condition are expressed as

$$n(L, t = 0) = n_s \tag{2.13}$$

$$G\,n(L = L_0, t) = B \tag{2.14}$$

where the initial condition (Eq. 2.13) gives the number density distribution of the seeds (n_s), and L_0 denotes the nuclei size. The assumption of $L_0 = 0$ was considered. The boundary condition (Eq. 2.14) establishes the nucleation rate B

as a birth rate at the domain[100], given in $[(min \cdot cm^3\ of\ suspension)^{-1}]$. The nucleation rate is described as

$$B = k_b\ exp\left(\frac{-E_{Ab}}{RT}\right)\Delta c^b \mu_3^\beta \tag{2.15}$$

where k_b is the nucleation constant $[(min \cdot cm^3\ of\ suspension\ )^{-1}(L\ of\ solution/\ g)^b(cm^3 of\ suspension/\mu m^3)^\beta]$; E_{Ab} is the nucleation activation energy $[J/mol]$; $b\ [-]$ and $\beta\ [-]$ are nucleation exponent parameters.

Applying the moment integral transform operator to Eq. 2.9[6], for $j = 0, 1, 2, 3$, the set of ODEs in Eq. 2.16-19 is obtained.

$$\frac{d\mu_0}{dt} = B \tag{2.16}$$

$$\frac{d\mu_1}{dt} = G_0\ (\mu_0 + \gamma\ \mu_1) \tag{2.17}$$

$$\frac{d\mu_2}{dt} = 2\ G_0\ (\mu_1 + \gamma\ \mu_2) \tag{2.18}$$

$$\frac{d\mu_3}{dt} = 3\ G_0\ (\mu_2 + \gamma\ \mu_3) \tag{2.19}$$

The moments μ_0, μ_1, μ_2, and μ_3 are proportional to the total crystal number, length, surface area, and volume, respectively. The volume of solution (volume free of solids) $V_{solution}$ can be written as

$$V_{solution} = (1 - \vartheta)\ V_{suspension} \tag{2.20}$$

where ϑ is the volume fraction of the total crystal population:

$$\vartheta = k_V \, \mu_3 \times 10^{-12} \tag{2.21}$$

where k_V is the volume shape factor. The factor 10^{-12} in Eq. 2.21 converts the third moment chosen dimension $[\mu m^3/cm^3 \; of \; suspension]$ to a dimensionless fraction. In this way, the solute mass balance in the batch crystallizer can be established for the K_2SO_4 concentration C expressed in $[g \; of \; solute \; / \; L \; of \; solution]$:

$$\frac{dC}{dt} = - \frac{3 \, \rho_c \, k_V}{1 - \vartheta} \, G_0 \, (\mu_2 + \gamma \, \mu_3) \tag{2.22}$$

where ρ_c is the crystal density.

The set of differential-algebraic equations described above defines the model of the batch crystallizer. The output model vector $y = \{ \tilde{\mu}_0 \, , \tilde{\mu}_1 \, , \tilde{\mu}_2 \, , \tilde{\mu}_3 \, , \tilde{C} \}$ is defined based on the variables measured during the crystallization experiments. The accent ~ represents the normalized variables. The output variables and model equations were normalized due to the differences in their orders of magnitude

The following normalization of variables $\mu_0, \mu_1, \mu_2, \mu_3,$ and C was adopted, inspired on the proposition by Secchi and Pereira[102], to obtain the normalized variables $\tilde{\mu}_0, \tilde{\mu}_2, \tilde{\mu}_3, \tilde{\mu}_4,$ and $\tilde{C}$:

$$\tilde{\mu}_j = \frac{\ln(\mu_j)}{12 + 2j} \quad , \quad j = 0, 1, 2, 3 \tag{2.23}$$

$$\tilde{C} = \frac{C}{C_{t=0}} \tag{2.24}$$

Eq. 2.23 and Eq.2.24 provided measured variables with the same order of magnitude for all sampling times in all experiments. To obtain the normalized

calculated outputs, the model equations in Eq. 2.16-19 and Eq. 2.22 also had the proper normalization performed, applying the chain rule to express the ODEs for the new normalized variables.

Numerical integration of the model was carried out by the integrator code DASSLC v3.9[103]. The temperature history of each experiment was as an input variable for the parameter estimation problem, using linear interpolation for each time step to perform the numerical integration.

2.3.2 Parameter estimation

The model parameter vector $\boldsymbol{\theta} = \{k_b, E_{Ab}, b, \beta, k_g, E_{Ag}, g, \gamma, k_V\}$ was determined by minimizing the objective function $\Omega(\theta)$ in Eq. 2.25 given by

$$\Omega(\boldsymbol{\theta}) = \sum_{e=1}^{N_e} \sum_{k=1}^{K_e} \sum_{i=1}^{N_y} \left(\hat{y}_i(t_{k,e}) - y_i(t_{k,e}; \theta) \right)^2 \tag{2.25}$$

where $t_{k,e}$ represents the k^{th} discrete (sampling) time point in the calibration experiment e; K_e is the number of time instants in experiment e; N_e represents the number of calibration experiments; N_y represents the number of measured variables; and $\hat{y}_i$ and y_i denotes the measured and predicted variables, respectively. The parameter estimation procedure was performed in MATLAB R2022a. First, the optimization problem was solved by a particle swarm optimization (PSO) algorithm[104] in series with the Nelder-Mead method (Flexible Polyhedron method)[105]. The tuning parameters of the PSO were: 15 generations, population size of 200, local and global search parameter of 1.5, and inertial factor of 0.8. The solution was then refined using the automatic parameter selection and estimation algorithm SELEST proposed by Secchi et al.[106]. This algorithm ensures a well-conditioned estimation problem of the identifiable parameters by selecting the more significant and less correlated ones.

In order to obtain the confidence intervals and confidence regions of the

parameters, the measurement variance $\boldsymbol{V}_y$ must be known. The residual variance between experimental data and predicted values ${s_R}^2$ is given by:

$$ {s_R}^2 = \frac{\Omega(\widehat{\boldsymbol{\theta}})}{N - P} \tag{2.26} $$

where $N = N_y \sum_{e=1}^{N_e} K_e$ is the number of all measured data, and P is the number of parameters (size of vector $\boldsymbol{\theta}$). The residual variance ${s_R}^2$ in Eq. 2.26 was assumed to be an estimator to the measurement variance, i.e., $\boldsymbol{V}_y \approx {s_R}^2 \boldsymbol{I}$. This approximation is valid when comparing the measurement variance for the 3 experiments (Exp4, Exp5, and Exp6) that represent replications (details in Section 2.6.3). The parameter covariance matrix $\boldsymbol{V}_\theta$ $(P \times P)$ is then given by[107,108]

$$ \boldsymbol{V}_\theta = {s_R}^2 (\boldsymbol{B}^T \boldsymbol{B})^{-1} \tag{2.27} $$

where $\boldsymbol{B}$ is the sensitivity matrix of dimension $(N \times P)$. The matrix $\boldsymbol{B}$ was obtained as a block matrix with N_e sensitivity matrices $\boldsymbol{B^e}$ of dimension $(K_e N_y \times P)$.

$$ \boldsymbol{B} = \begin{bmatrix} \boldsymbol{B^1} \\ \boldsymbol{B^2} \\ \vdots \\ \boldsymbol{B^{N_e}} \end{bmatrix} \tag{2.28} $$

$$ \boldsymbol{B^e} = \frac{\partial \boldsymbol{y}^e}{\partial \boldsymbol{\theta}} \tag{2.29} $$

where $\boldsymbol{y}^e$ is the vector that contains all k discrete time points of all measured variables for a calibration experiment $\boldsymbol{e}$:

$$ \boldsymbol{y}^e = \{y_{1,k}, y_{2,k}, \dots, y_{N_y,k}\}, \;\; k = 1, 2, \dots, K_e. \tag{2.30} $$

The sensitivity matrix $\boldsymbol{B}$ was approximated by central finite differences. Such simplification allows rewriting the hyper-ellipsoid-like confidence region of the parameters related to the least-square objective function $\Omega(\boldsymbol{\theta})$[108]

$$\left(\boldsymbol{\theta}-\widehat{\boldsymbol{\theta}}\right)^{T}\left(\boldsymbol{B}^{T}\boldsymbol{B}\right)\left(\boldsymbol{\theta}-\widehat{\boldsymbol{\theta}}\right) \leq {s_R}^2 \frac{P}{N-P} F_{P,N-P}^{1-\alpha} \tag{2.31}$$

where $F_{P,N-P}^{1-\alpha}$ is the upper critical value of the F-distribution with significance level $\alpha = 0.05$ (confidence intervals of 95%), and P and $N-P$ are the number of parameters and the degrees of freedom, respectively.

The parameter correlation matrix $\boldsymbol{R_\theta}$ $(P \times P)$ was calculated from $\boldsymbol{V}_\theta$. The element of $\boldsymbol{R_\theta}$, r_{ij}, is related to the element of $\boldsymbol{V}_\theta$, v_{ij}, as

$$r_{ij} = \frac{v_{ij}}{\sqrt{v_{ii}\, v_{jj}}} \tag{2.32}$$

The approximate confidence intervals of the parameter θ_i $(i = 1, 2, \ldots, P)$ were determined using the t-test:

$$\hat{\theta}_i - t_{\alpha/2,(N-P)}\sqrt{v_{ii}} < \theta_i < \hat{\theta}_i - t_{\alpha/2,(N-P)}\sqrt{v_{ii}} \tag{2.33}$$

The hyper-ellipsoid confidence region (Eq. 2.31) consist of an approximation of the true confidence region, which is only exact for linear model parameters[109]. Therefore, to obtain better accurate confidence regions to the nonlinear model parameters, the true confidence region was determined in this work as

$$\Omega(\boldsymbol{\theta}) \leq \Omega\left(\widehat{\boldsymbol{\theta}}\right)\left(1 + \frac{P}{N-P} F_{P,N-P}^{1-\alpha}\right) \tag{2.34}$$

also using $\alpha = 0.05$. The nonlinear confidence region was then determined using a more exploratory particle swarm optimization algorithm. In this case, due to the high computational cost to construct the true confidence region, successive passes using the tuning parameters of 1000 generations and a population of 500. were performed until convergence of the shape of the confidence region, which was evaluated by analyzing plots of pairs of parameters.

2.4 Results and Discussion

2.4.1 Crystal shape investigation

During the experiments, measurements of two lengths d_{F^+} and d_{F^-} are performed, as discussed in Section 2.2.3. Thus, we preliminarily investigated crystal morphology using these two variables.

The aspect ratio, defined by $AR = d_{F^-}/d_{F^+}$, can represent the crystals' shape. Its distribution was monitored during each experiment. We observed that the distributions of AR was invariant with time, with significant values for AR around 0.445 ($\approx 15\%$) and 0.705 ($\approx 40\%$). These two more expressive values for AR can be explained by the different spatial orientations of the crystals when measured in the analyzer's flow cell. Similar behavior was observed when comparing the profile between the experiments (Figure 2.6), indicating that, under the studied conditions, the population of K_2SO_4 crystals presents a similar shape in the face of nucleation and growth phenomena. Figure 2.6 shows the AR distributions for the experiments Exp1, Exp5, and Exp10 (chosen in different time instants). The AR profiles are pretty similar, even for the lowest percentages shown in the inner frame of Figure 2.6.

In this way, the modeling that considers only one length to characterize the crystals is adequate for the case of K_2SO_4 in the performed experimental conditions. The result obtained in this work indicates that, for the evaluated experimental conditions, the crystal growth rate in different directions is quite similar, being possible to use one characteristic length as an internal variable of the PBM.

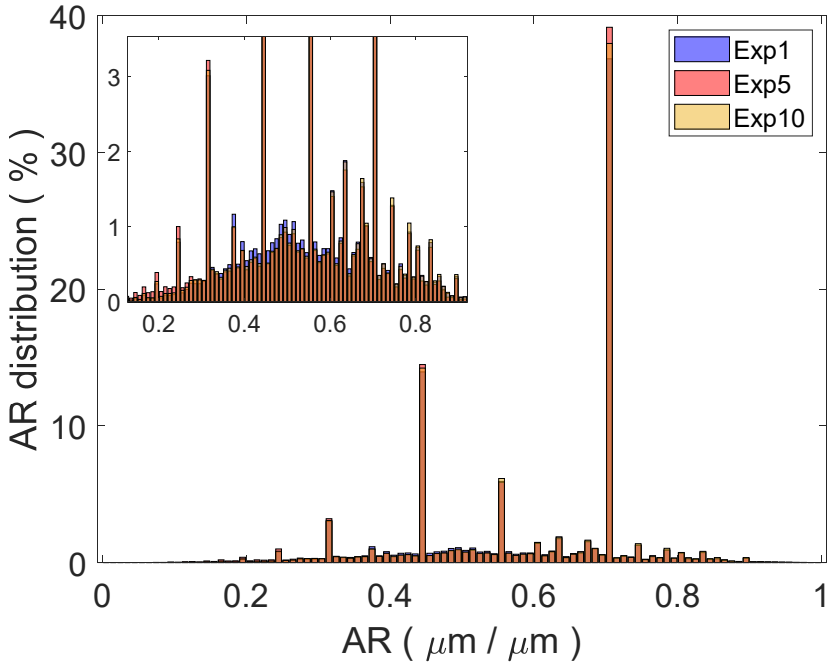

Figure 2.6 - Aspect ratio (AR) distribution for Exp1 (blue), Exp5 (red), and Exp10 (yellow).

2.4.2 Parameter estimation of the PBM

Using model structure presented in Section 2. 3.1, the hybrid procedure for parameter estimation proved to be efficient. The minimum value of the objective $\Omega(\widehat{\boldsymbol{\theta}})$ was improved throughout the series of the optimization algorithms: 0.1270 for the PSO, 0.1019 for the Nelder-Mead method, and 0.1013 for the SELEST. Notably, the low values found also reflect the effect of normalization on the output values. Regarding SELEST, all parameters were considered identifiable and, thus, re-estimated. The numerical procedure ranked the parameters based on two identifiability criteria: the influence of the parameters on the predictions and the influence of the parameters among themselves. The selection order found was $\{b > g > \beta > k_b > k_V > k_g > \gamma > E_{Ab} > E_{Ag}\}$. Thus, using the SELEST algorithm corroborates the good identifiability of the parameters by meeting the prediction quality criteria and the non-correlation for most of them.

Table 2.4 presents the estimated parameters and the 95% confidence intervals determined by Eq. 2.33.

Table 2.4 - Estimated parameters and the respective meaning and confidence intervals

Parameter	Meaning	Value	95% CI
k_b	nucleation rate constant $[(min \cdot cm^3)^{-1}(L/g)^b(cm^3/\mu m^3)^\beta]$	0.9341	± 0.0192
E_{Ab}/R	nucleation activation energy $[K]$	6.8740 $\times 10^3$	± 7.6237
b	nucleation supersaturation exponent $[-]$	0.8361	± 0.0200
β	nucleation third moment exponent $[-]$	1.3728	± 8.0329 $\times 10^{-4}$
k_g	growth rate constant $[(\mu m/min)(L/g)^g]$	3.7792$\times 10^5$	± 1.6474$\times 10^5$
E_{Ag}/R	growth activation energy $[K]$	4.8654 $\times 10^3$	± 138.7787
g	growth supersaturation exponent $[-]$	1.6228	± 0.0354
γ	size-dependent growth constant $[1/\mu m]$	2.3895$\times 10^{-3}$	± 7.6281$\times 10^{-5}$
k_V	volume shape factor $[-]$	1.3486	± 0.1303

This parameter uncertainty analysis is limited only under the evaluation of confidence intervals. For this reason, the parameter correlation matrix and the confidence regions were also presented in this work. The confidence regions delimited by hyper-ellipsoid (Eq. 2.31) are still a linear approximation for the model parameters. Even so, they present additional relevant information for the correlation between the parameters, indicated by the slope of the ellipses. Figure 2.7 shows the parameter correlation matrix, presenting a low correlation among

most of the pair of parameters, which is also evidenced by the shape of the ellipses in Figure 2.8 and 9 (orange line). The activation energies $E_{A,g}$ and $E_{A,b}$ show a strong correlation with the parameters k_g and k_b, respectively, which is a well-known behavior due to the structure of the Arrhenius equation. On the other hand, the activation energy $E_{A,b}$ shows a low correlation with the other parameters, which is illustrated by some of the ellipses in Figure 2.8.

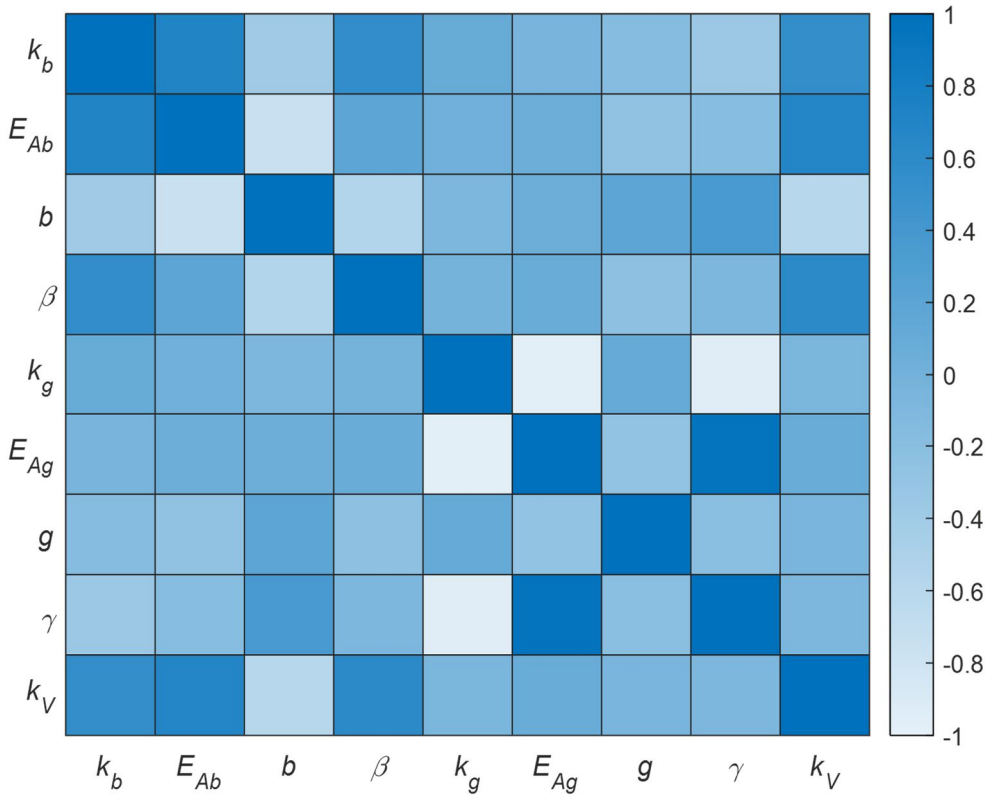

Figure 2.7 - Parameter correlation matrix

The confidence regions for non-linear models in the parameters are presented in Figure 2.8 and 9 by the regions delimited by the high density of points obtained using the exploratory PSO. For the construction of the regions, four successive passes in the algorithm were necessary for convergence, and a total of 468,513 particles composed the confidence regions for the established cutoff criterion. With such regions, an adequate description of the estimated parameters

that describe the experimental data can be acquired, highlighted by the significant difference compared to the elliptical approximations for some cases.

Analyzing the regions delimited by pairs of parameters, some behaviors are discussed. First, the strong correlations between the pairs $E_{A,g}$-k_g and $E_{A,g}$-γ are not observed for the respective true confidence regions in Figure 2.9. For the pair $E_{A,g}$-γ, it is worth noting that the range delimited by both regions is close, differing by the observed inclination for the ellipse. In particular, the regions involving the parameter $E_{A,g}$ are overestimated when using the approximated approach.

In general, the true confidence regions showed the non-correlation between the estimated parameters, except, curiously, for the pair $E_{A,b}$-β. This pair, as evidenced by the underestimation of the region delimited by the ellipse, showed no evident correlation for the approximation of linear model parameters. Notably, the activation energies $E_{A,b}$ and $E_{A,g}$ were the last parameters selected by SELEST.

It is clear, therefore, that the evaluation of the trust region through Eq. 2. 29, although computationally expensive, offers advantages over the linear approximation. Notably, the estimation of activation energies provided a more significant discrepancy between the two approaches.

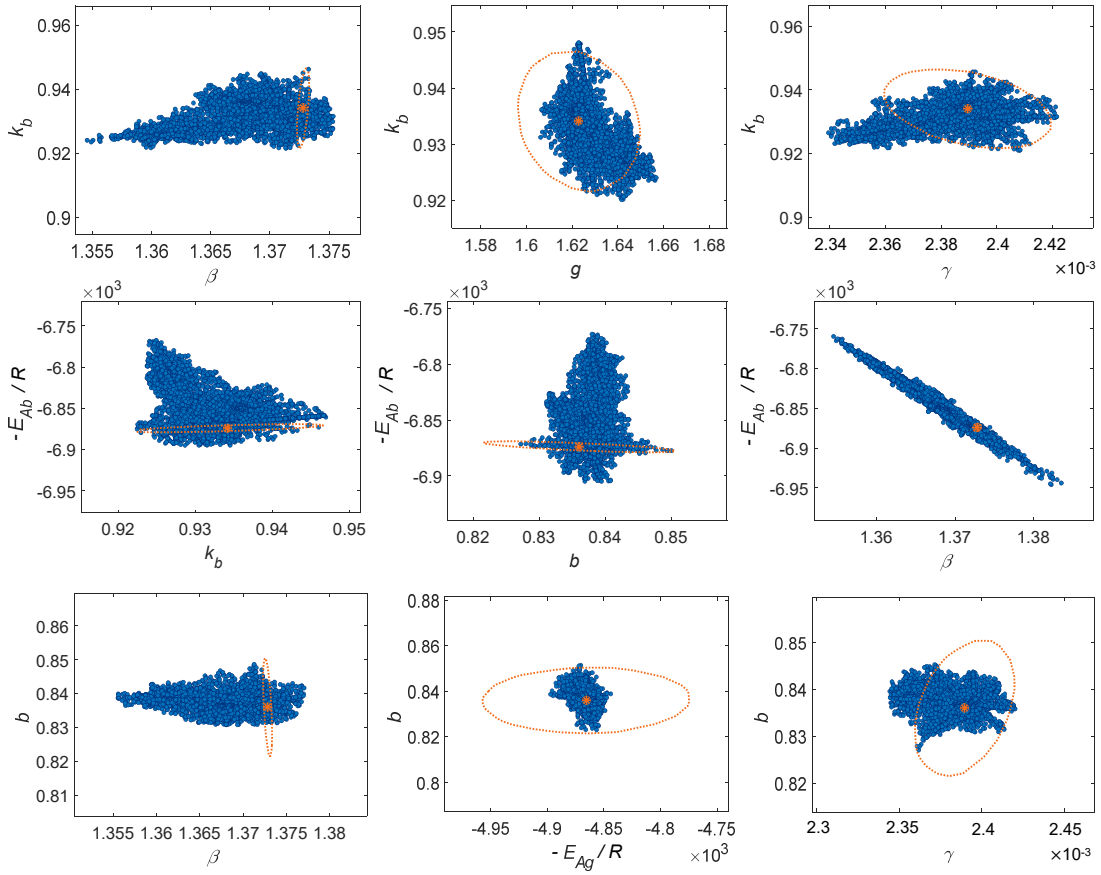

Figure 2.8 - Some confidence regions of pair of parameters: for k_b (first row), E_{Ab} (second row), and b (third row). The ellipse approximations are in orange, and the true confidence region points in blue.

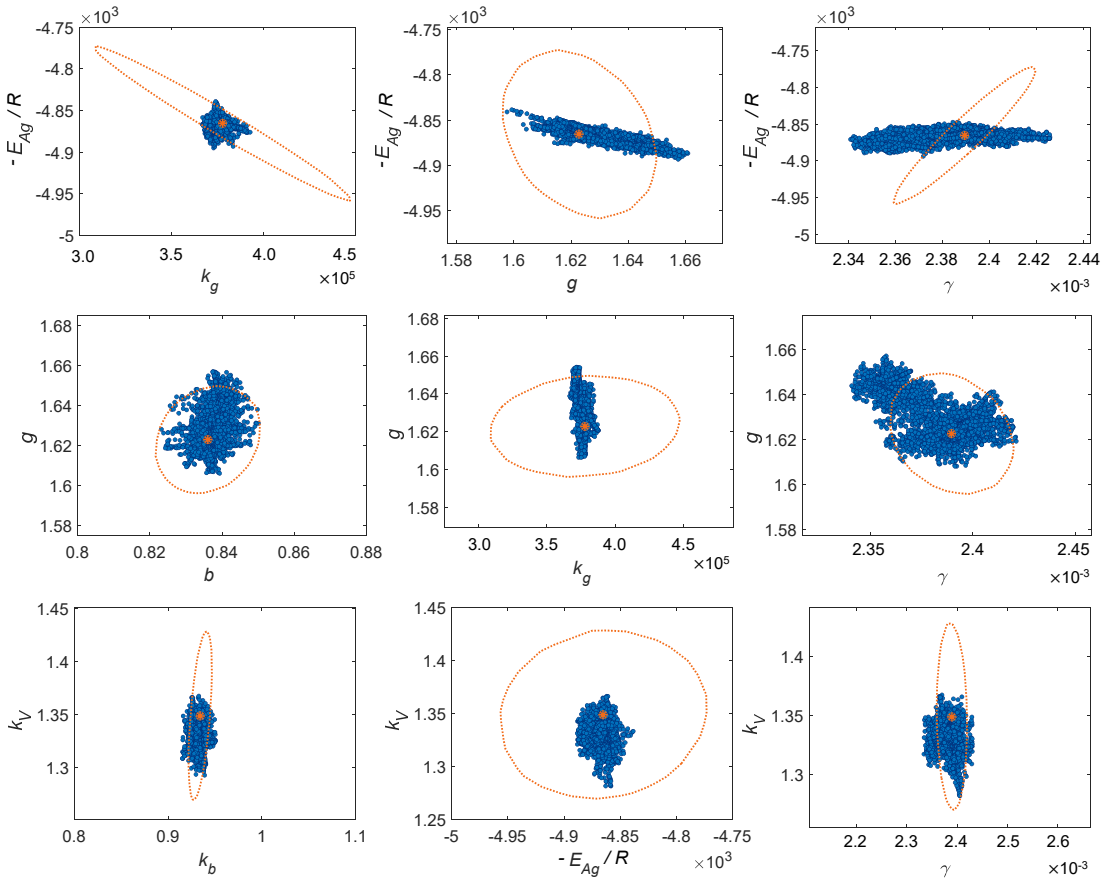

Figure 2.9 - Some confidence regions of pair of parameters: for E_{Ag} (first row), g (second row), and k_V (third row). The ellipse approximations are in orange, and the true confidence regions points in blue.

Figure 2.10 shows the temperature profiles (inputs in the parameter estimation problem) and the comparison between the experimental data and the predicted values over time for the different batches. The good prediction of the model can be evidenced for all the experiments used in the calibration.

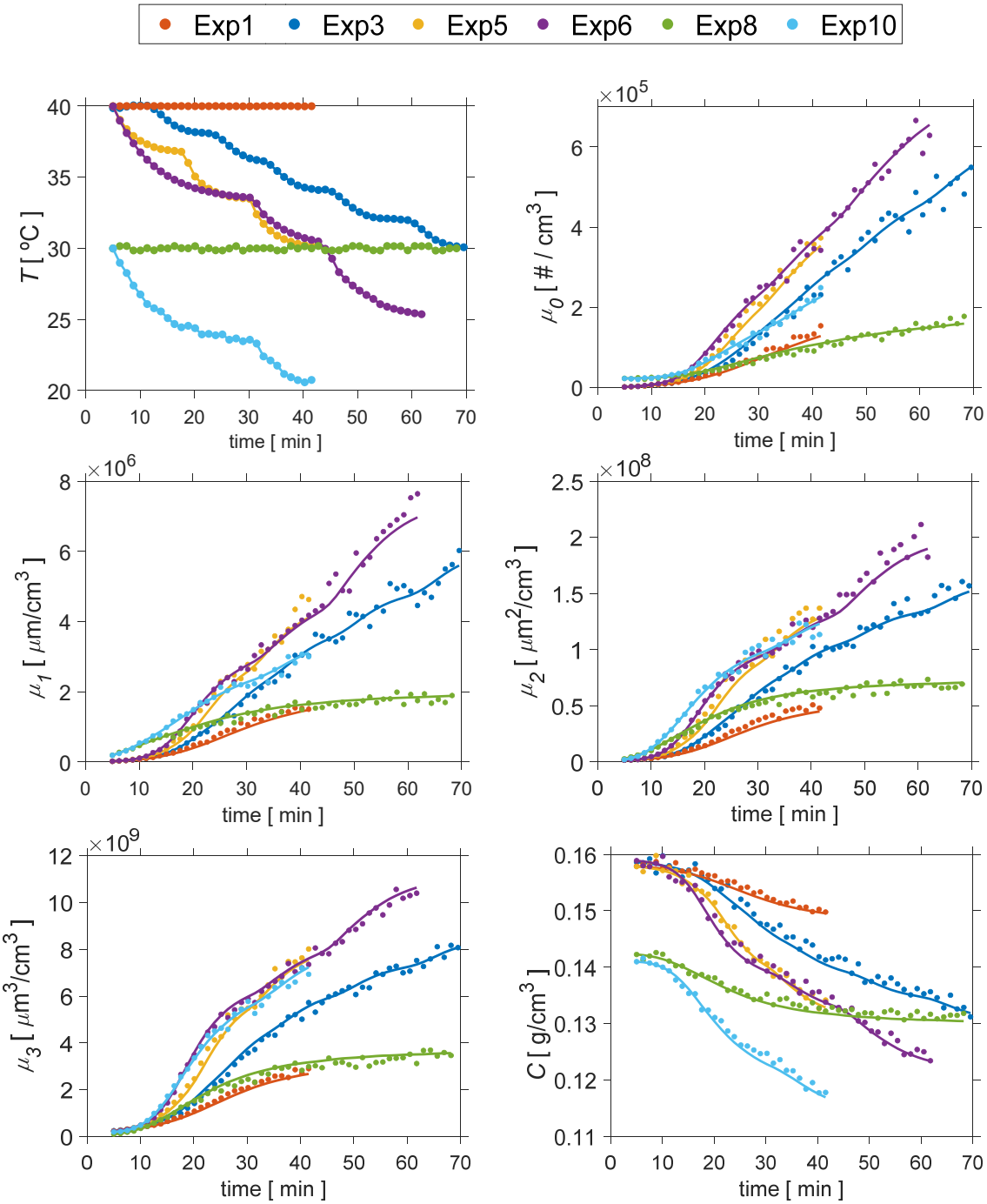

Figure 2.10 - Experimental temperature policies performed and comparison between the experimental data and the fitted model values of $\mu_0, \mu_1, \mu_2, \mu_3$, and C for the calibration experiments.

In this regard, the adopted approach that the residual variance between experimental data and predicted values was used to approximate the measurement variance to overcome the lack of a complete measurement variance

was relevant. The value of the residual variance found after estimation by SELEST, $s_R{}^2 = 8.5428 \times 10^{-5}$, presents a good approximation of the value of the measurement variance (Figure 2.11) for the experiments in triplicate. Figure 2.11 presents the value of measurement variance for all sampling times for the triplicates Exp4, Exp5, and Exp6, considering all variables in normalized form. The time average for the measurement variance for all points in Figure 2.11 is 5.7747×10^{-5}, a value close to the $s_R{}^2$ found.

.

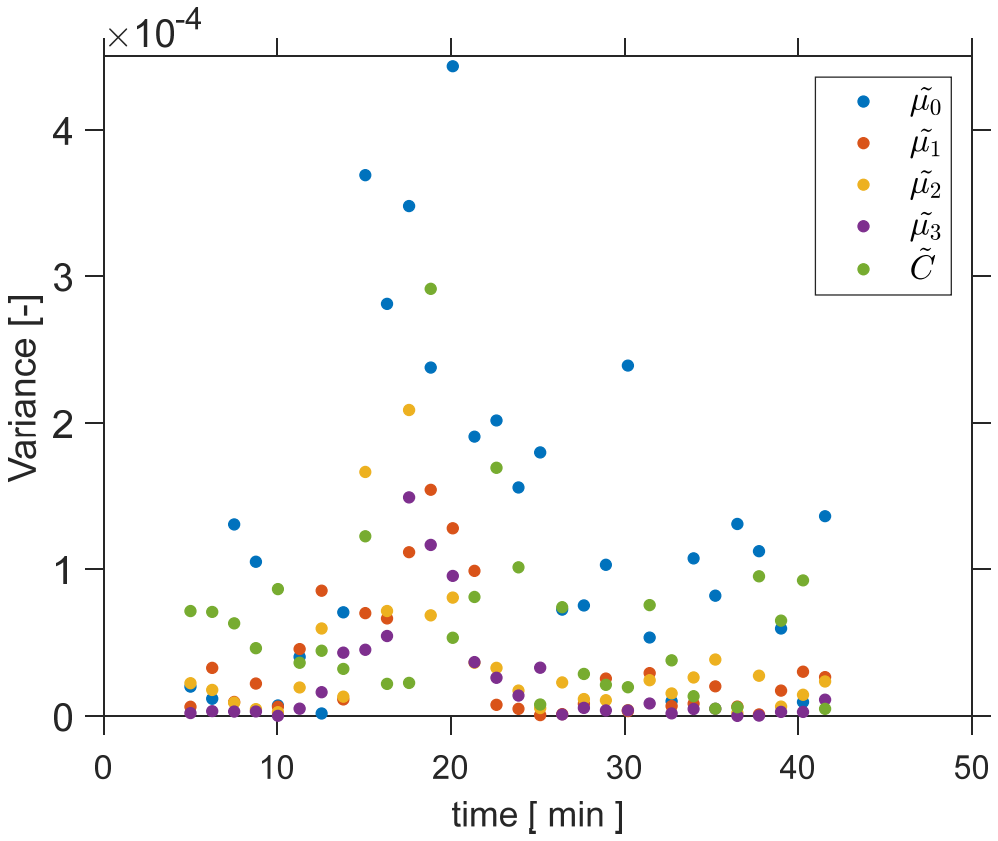

Figure 2.11 - Measurement variances of the normalized variables $\tilde{\mu}_0, \tilde{\mu}_1, \tilde{\mu}_2, \tilde{\mu}_3$, and $\tilde{C}$ along over time for the triplicate batch experiments Exp4, Exp5, and Exp6.

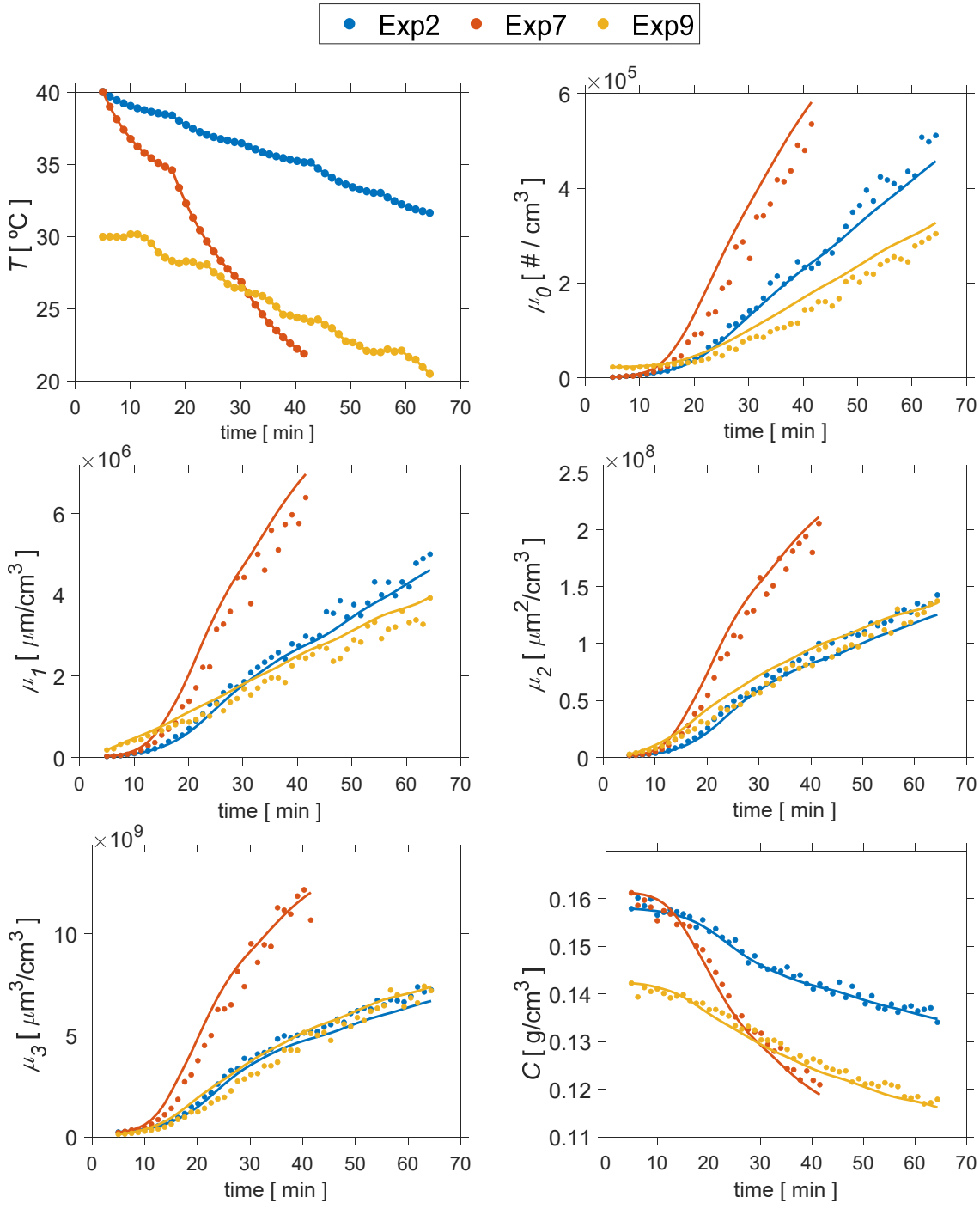

Figure 2.12 - Experimental temperature policies performed and comparison between the experimental data and the fitted model values of $\mu_0, \mu_1, \mu_2, \mu_3$, and C for the validation experiments.

Figure 2.12 compares the experimental and predicted values over time for experiments not used in parameter estimation, i.e., validation experiments. The result shows the validation of the predictive model.

The results showed the size-dependent growth rate expression used (Eq. 2.10) for K_2SO_4 in water is adequate for the analyzed conditions.

2.5 Conclusions

We performed experiments for batch crystallization of potassium sulfate in water using dynamic image analysis data to obtain the solid phase information. A phenomenological model was developed considering the crystals' nucleation and size-dependent linear growth rate. Experimental data from calibration experiments were used to process the data from dynamic image analysis for the crystal phase information to estimate the model parameters. The expression for growth rate with a linear dependence on the size of the crystals proved to be adequate for the evaluated experiments, allowing a good correlation for experiments in which there are small crystals.

In addition to the confidence interval representation for the parametric uncertainty, the confidence regions were obtained by an exploratory particle swarm algorithm and compared with the approximate ellipsoid regions, highlighting the difference between the approaches when dealing with nonlinear models, as in the present case. The estimated parameters showed mostly low correlation and narrow confidence regions. The estimation of the parameters adopting three optimization algorithms in series made it possible to refine the optimal solution and have the parameters' selection order by identifiability analysis. The values observed for the measurement variance of replications and the residual variance were close, which made it possible to confirm the hypothesis used, often adopted without proper checking in the literature.

The developed model underlines the potential of using real-time image analysis in an ex-situ sampling loop. The good prediction of the experimental data, both in the calibration and validation experiments, enabled using a digital twin model for the studied process.

Chapter 3

Model-Based Optimal Control of Supersaturation, Size, and Shape in Crystallization Processes

The chapter presents different studies carried out to control batch crystallization processes. Section 3.1 presents the experimental results of open-loop control of supersaturation for K_2SO_4 in water using the apparatus and model in Chapter 2. Section 3.3 discusses the use of neural networks for the crystallization of K_2SO_4 presented in Chapter 2, comparing the predictive control strategies using the phenomenological model presented in Chapter 2 (BP-NMPC) and a recurrent neural network, Echo State Network (ESN-NMPC), based on this model. Section 3.3 extends the control study to the crystallization of KDP, presenting the results of the modeling and control simulations investigated.

This chapter was mainly adapted from the following published works:

i. Moraes, M. G. F.; Secchi, A. R.; Lage, P. L. C.; Souza Jr., M. B. Controle Ótimo da Supersaturação em Processos de Cristalização com Análise de Imagens. In: XXIII Congresso Brasileiro de Engenharia Química, 2021, Gramado. COBEQ 2021, 2021.v. 1. p. 1-4.

ii. de Moraes, Marcellus G.F.; Grover, Martha A.; de Souza, Maurício B.; Lage, Paulo L.C.; Secchi, Argimiro R. Optimal Control of Crystal Size and Shape in Batch Crystallization Using a Bivariate Population Balance Modeling. IFAC-PAPERSONLINE, v. 54, p. 653-660, 2021.

The application of recurrent neural network to crystal size control was adapted from the following paper recently submitted to Industrial & Engineering Chemistry Research:

iii. de Moraes, M. G. F.; Lima, F. A. R. D; Lage, P. L. C.; de Souza Jr., M. B.; Barreto Jr., A. G; Secchi, A. R. Modeling and Predictive Control of Cooling Crystallization by Dynamic Image Analysis: Combining Population Balance Model and Recurrent Neural Networks-Based Approaches.

3.1 Open-loop supersaturation control in K_2SO_4 Cooling Crystallization

3.1.1 Introduction

Supersaturation is one of the most important variables in crystallization processes, corresponding to the driving force of this process. Supersaturation control is a widely used strategy in crystallization processes, used to balance the simultaneous occurrence of crystal growth and primary or secondary nucleation, thus reflecting on better achievement of the specification of the crystals to be produced.

The supersaturation control was obtained by applying the optimal temperature policy obtained from the process model for cooling-batch crystallization in an open-loop, adjusted with data from image analysis. The predicted and experimentally realized temperatures for three different supersaturation levels are presented for the crystallization of potassium sulfate.

The maintenance of these levels was achieved for the cases studied, and experimental values were also obtained for the average particle size in good agreement with the predicted ones, indicating good adequacy of the model for the control of supersaturation and its influence on the size of the crystals.

For supersaturation control, the predictive model proposed in Chapter 2 was solved to provide the temperature policy that should be implemented experimentally. The analysis of images by video microscopy was used to monitor the solid phase during the experiments carried out, with the interpretation of data being facilitated and the most accurate measurements possible to be obtained with this technique. Thus, the optimal control of supersaturation was experimentally carried out for the crystallization of potassium sulfate.

3.1.2 Methodology

The experiments were carried out in the same experimental setup describe in Section 2.2. The set of ODEs is solved to obtain the temperature policy to be implemented. The supersaturation $\Delta C = C - C_s$ is wanted to be constant, i.e., $(\Delta C)/dt = 0$. As $C_s = C_s(T)$:

$$\frac{\mathrm{d}C}{dt} = \frac{\mathrm{d}C_s}{dt} = \frac{\mathrm{d}C_s}{dT}\,\frac{\mathrm{d}T}{dt} \tag{3.1}$$

where C_s is a polynomial of the form $C_s(T) = A\,T^2 + B\,T + C$ (Eq. 2.12), implying that

$$\frac{dT}{dt} = \frac{1}{(2\,AT + B)}\,\frac{\mathrm{d}C}{dt} \tag{3.2}$$

Eq. 3.2 is used with the process model to obtain the temperature policies to control supersaturation. Three different levels of supersaturation were defined

for a final batch time of 60 minutes, as shown in Table 1. Seeds with an average size of 170 µm, produced in a previous test, were used. The same initial concentration of K_2SO_4 ($C_0 = 0.1586\ g/cm^3$) was adopted in all experiments.

Table 3.1 - Variables' levels used in the experiments of supersaturation control

Supersaturation (g/cm³)	1.135×10^{-2}	2.909×10^{-2}	4.742×10^{-2}
Initial Temperature (°C)	40	30	20

3.1.3 Results and Discussion

Figure 3.1 (left) shows the calculated temperature variation policies (solid lines) and the experimentally implemented (dotted lines) for the three desired supersaturation levels and the measured supersaturation levels (right).

In Figure 3.1, the temperature policies carried out could correctly represent the transitions in the model, using the internal control of the experimental thermoregulator of the process. The supersaturation level was maintained, presenting minor errors compared to the desired set points. It is noticeable that for the case of a higher level of supersaturation, the deviations are more pronounced, which can be explained by the model having been extrapolated to this high level of supersaturation.

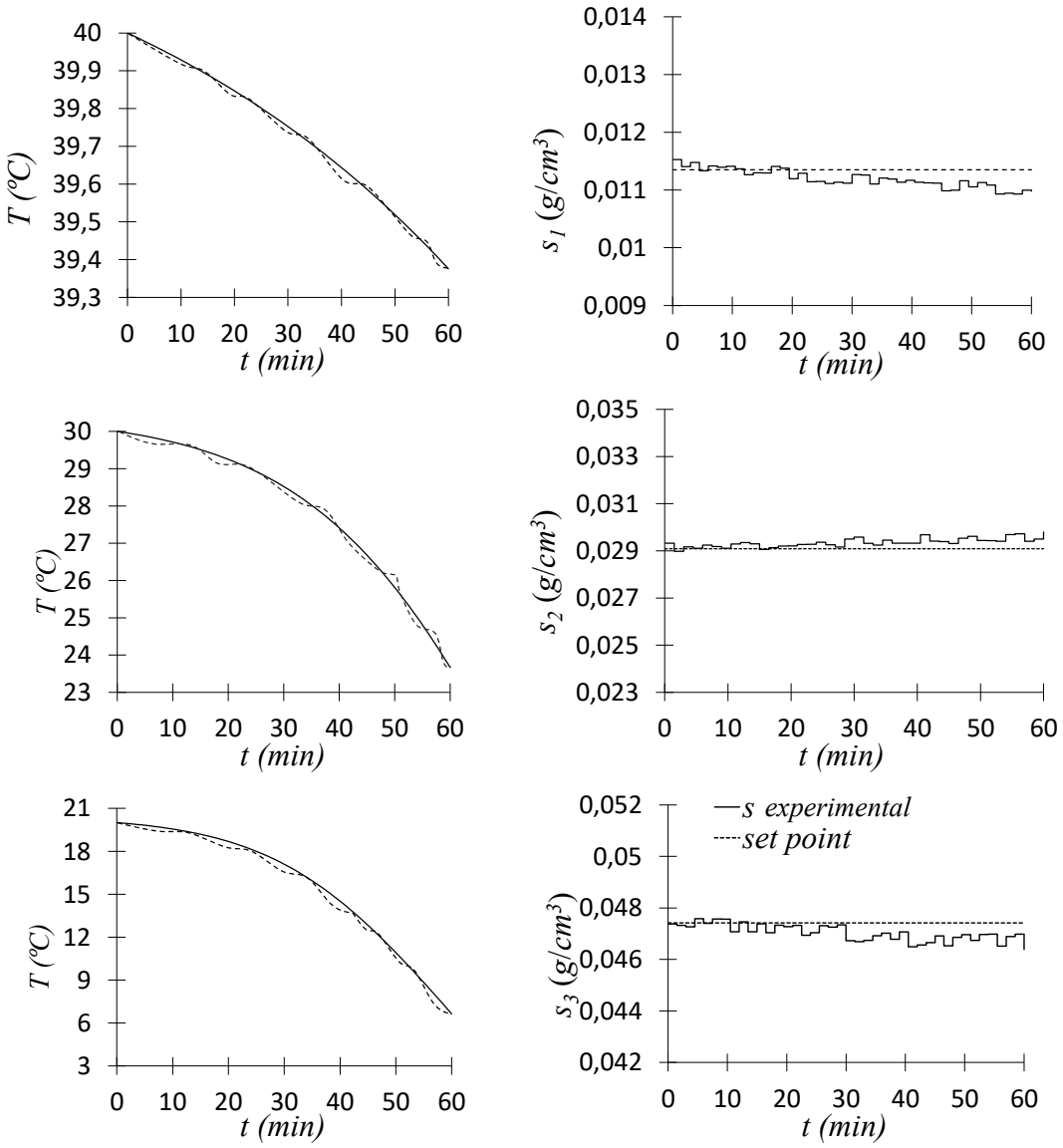

Figure 3.1 - Temperature policies (left) and the respective measured supersaturation (right).

Figure 3.2 shows the evolution of the number-average crystal size ($\bar{L}_n$) for the three different levels of supersaturation. For each sampling time interval, the measured particles passing through the cell were randomly divided into four groups. The circles in Figure 2 represent the mean values for $\bar{L}_n$. Standard deviations were calculated from the mean values for each group. For a confidence level of 95% and a degree of freedom equal to 3, the data were considered normally distributed, following the t-distribution for computing the errors, represented by the bars in Figure 3.2.

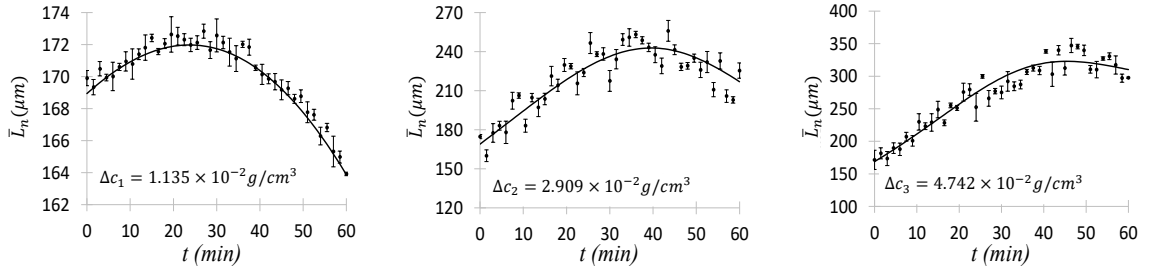

Figure 3.2 - Number-average characteristic size $\bar{L}_n$ for open-loop supersaturation control: experimental points (circles) and predicted values (solid line).

It is observed in Figure 3.2 that the experimental values follow the trend predicted by the model for $\bar{L}_n$, which is better evidenced considering the experimental error presented. The observed variations can be attributed to modeling errors, measurement errors, and the open-loop control strategy, which is susceptible to the significant influence of disturbances.

3.1.4 Conclusions

The model developed in Chapter 2 proved adequate for the optimal control of supersaturation for the crystallization of potassium sulfate in cooling batches. The influence on the crystal size was also investigated, showing good prediction of values over time for the experiments carried out.

3.2 Neural Network-based Predictive Control of Crystal Size in K_2SO_4 Cooling Crystallization

3.2.1 Neural Networks and Echo State Network

The neural networks can be classified into two kinds depending on how the data flows through the network: the feedforward and the feedback network. In the first one, the information entering the network always goes to the next layer, never returning to the previous one. The structure of the feedforward network

(Figure 3.3a) is composed of an input layer, an output layer, and one or more hidden layers[110]. The multilayer perceptron (MLP) is a feedforward network and is the most applied in the literature because of its simplicity[111].

The feedback network presents a different structure from the previous type (Figure 3.3b), composed of a hidden state and a feedback loop of hidden states[112]. This feedback loop introduces previous information to the current state and uses it to update the current hidden state[113]. This structure allows the network to simulate time series and predict dynamic behaviors[114]. The feedback network is also known as a recurrent neural network (RNN).

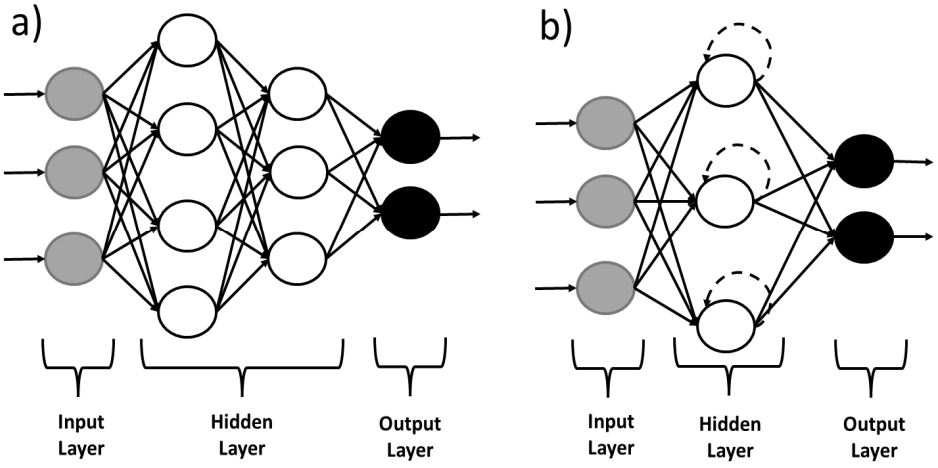

Figure 3.3 - Typical structure of: a) a feedforward network; b) a feedback network.

For the RNNs, the gradient update of the model parameters that minimize the loss function is calculated using a backpropagation through time (BPTT) algorithm. This method calculates and saves the difference between the target and the output for each past time step. Then, the weight gradient updates are calculated as the network is feedback[115]. However, RNNs trained with this algorithm can present vanishing or explosion to infinity gradient issues[116], introducing a necessity to improve this algorithm and create new structures of RNN, such as the echo state network (ESN)[112].

The ESN comprises an input layer, a dynamical reservoir, and an output layer, as shown in Figure 3.4, in which W represents the weight vectors for each layer[117]. First, the network inputs are fed into the input layer and then sent to the reservoir layer. The reservoir layer is the recurrent part, where the outputs of the reservoir and output layers are feedback[118]. Moreover, the weights of the reservoir layer were not obtained by the training step but are randomly fixed, avoiding local minimum problems[119]. Equation 3.3 represents the mathematical modeling of the reservoir layer[120]. Therefore, u, x and y are the input, state and output vectors at time k; W is the weight vector for each layer as represented in Figure 3.4; f is the activation function, usually, a hyperbolic tangent; φ is known as the leak rate, and is the complementary percentage of a current state $x(k)$ that is transferred into the next state $x(k+1)$.

$$x\,(k+1) = (1-\varphi)x(k) + \varphi f\left(W_{ux}u(k) + W_x x(k) + W_{yx}y(k)\right) \tag{3.3}$$

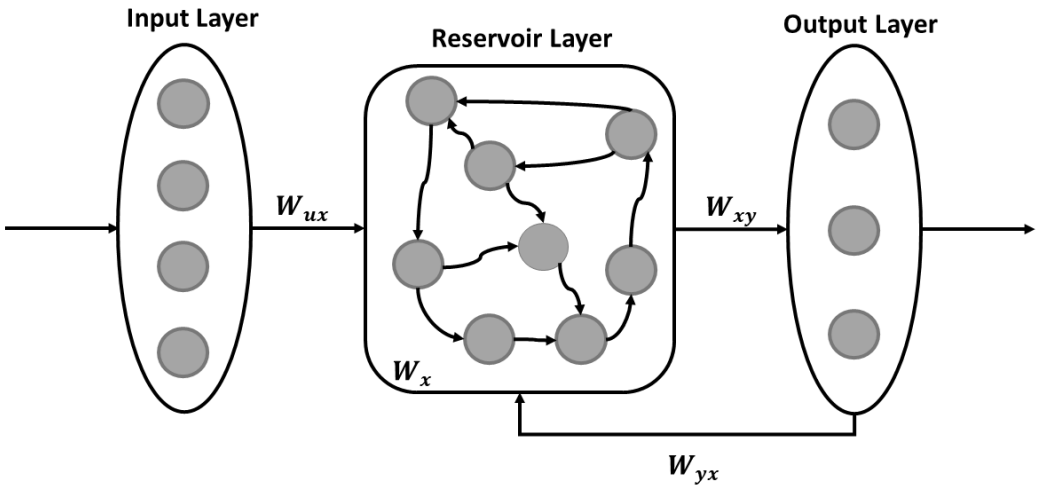

Figure 3.4 - Structure of an ESN.

The results of the reservoir layer are sent to the output layer in order to calculate the expected responses. The mathematical modeling of the output layer is given by

$$y(k+1) = W_{hy}\, x(k+1) \tag{3.4}$$

The neural network models developed in this study were based on the ESN. Therefore, four different networks were developed to predict the moments' values in the future, and the inputs and outputs of each network are presented in Table 3.2, where k indicates the timestep. The ESNs were implemented using the library pyESN developed by Korndörfer[121], and all hyperparameters chosen for the neural networks were defined by trial and error. The ESNs were initially defined using a reservoir layer with 10 neurons, a random state of one, a noise value of 0.01, and a linear activation function for the output recurrence and the output layer. Then, the hyperparameters were changed in order to achieve the R^2 values close to one for the test samples. This procedure was carried out to predict one sampling time forward for all moments.

Table 3.2 - Inputs and outputs of the developed neural networks

Neural Network	Inputs	Outputs
ESN 1	$\mu_0(k), T(k)$	$\mu_0(k+1), \dots, \mu_0(k+n)$
ESN 2	$\mu_0(k), \mu_1(k), T(k)$	$\mu_1(k+1), \dots, \mu_1(k+n)$
ESN 3	$\mu_1(k), \mu_2(k), T(k)$	$\mu_2(k+1), \dots, \mu_2(k+n)$
ESN 4	$\mu_2(k), \mu_3(k), T(k)$	$\mu_3(k+1), \dots, \mu_3(k+n)$

In order to obtain the surrogate model using ESNs, the training dataset was defined using the co-teaching learning algorithm. This strategy takes advantage of noisy-free data, using a dataset composed of noisy-free and noisy data[122]. In particular, the current work applies a symmetric co-teaching algorithm, which uses a mixed dataset containing noisy and noise-free data. Initially, a mini-

batch is chosen from the original dataset at each epoch. Then, each model analyzes its data sequences and produces a small dataset containing all the data with a low error function value. This new dataset is sent to the peer network, and this process is repeated until the end of the training epochs[123].

The training set comprised of one experimental batch and simulated data, representing a 200 min batch crystallization. Only one experiment was chosen for the training dataset because the dataset has to be ordered according to the time process, and each batch is a different time series. The simulated data was generated by applying the phenomenological model presented in Chapter 2. This way, the validated PBM was used with the machine learning model in the training phase using coteaching. We chose experiment Exp4 because it has the largest number of experimental points with the initial conditions listed in Table 3.3.

Table 3.3 - Initial condition of Exp4

$T\ (°C)$	$\mu_0\ (1/cm^3)$	$\mu_1\ (\mu m/cm^3)$	$\mu_2\ (\mu m^2/cm^3)$	$\mu_3\ (\mu m^3/cm^3)$	$C\ (g/cm^3)$
39.38	1559.23	21237.53	1847000.97	234067271.73	0.1605

The training dataset can be divided into three parts according to the temperature behavior. The first occurs from the initial moment until 81.23 min. It comprises a mixture of 61 experimental and 2000 simulated data lines, each with the temperature values and the four moments at a given sampling time. This first part of the dataset represents what happens with the moments when the vessel is cooled from 40°C to 20°C. The second part appears from 81.23 min until 141.23 min, composed of 2000 simulated data lines, for which the temperature is kept at 20°C. This second part was designed for the network to learn what happens when the temperature is maintained constant. Finally, the last part occurs from 141.23 min until the end of the batch and is composed of 2000

simulated data lines. This last part was designed for the network to learn the moments' behavior from 20 to 0°C.

The test dataset was also composed of simulated and experimental data, but a different approach from the training dataset was used. The nine remaining batches (Exp1, Exp2, Exp3, Exp5, Exp6, Exp7, Exp8, Exp9, Exp10) and three new simulation runs were used to compose the test dataset. Unlike the training dataset, the test did not mix the 418 experimental and the 3000 simulated data lines for the analysis. The simulation runs are named Simu1, Simu2, and Simu3. Each experiment and simulation was studied apart.

Each simulation run of the test dataset is composed of results for pre-defined batch temperature profiles and departs from different initial conditions according to the experiments. The temperature profiles for each simulation were defined by linear regression according to the experimental values. The conditions applied for the three simulations are shown in Table 3.4.

Table 3.4 - Conditions used for the three simulation runs.

Conditions	**Simu1**	**Simu2**	**Simu3**
Initial T (°C)	40.00	39.99	29.99
Initial μ_0 $(1/cm^3)$	1468.51	1534.31	23013.90
Initial μ_1 $(\mu m/cm^3)$	22775.44	20715.19	193974.30
Initial μ_2 $(\mu m^2/cm^3)$	1621714.42	1676956.24	2879288.76
Initial μ_3 $(\mu m^3/cm^3)$	239513860.62	223640524.96	101115869.96
Initial C (g/cm^3)	0.1578	0.1579	0.1423
Batch Time (min)	75.00	75.00	75.00
Final Temperature (°C)	40.00	20.00	15.00

3.2.2 Nonlinear Model Predictive Controller

Model predictive control (MPC) consists of an approach that applies an internal model of the process to predict the system's behavior and account for this information for the application of the control action[124]. In this controller, the model is initially fed with the past inputs and outputs and the future inputs given by the optimizer. Therefore, the model uses this information to predict future output variables values. The predictions are compared to a reference trajectory, and the future errors are calculated[125]. The optimizer minimizes the objective function obtained based on the calculated errors and considers the process constraints. The optimizer obtains the future control actions, which the model uses, and the first control action is applied to the process.

The controlled variables chosen for the optimization problem were the coefficient of variation (CV) and the number-average crystal size ($\bar{L}_n$), which can be calculated by Eq. 3.5 and Eq. 3.6, respectively.

$$CV = \sqrt{\frac{\mu_2 \mu_0}{\mu_1^2} - 1} \tag{3.5}$$

$$\bar{L}_n = \frac{\mu_1}{\mu_0} \tag{3.6}$$

The temperature was the input variable because it was the only manipulated variable available. The NMPC goal is to minimize the process performance index J, the objective function of the problem shown in Eq. 3.7

$$J = \sum_{j=1}^{H} \delta[CV(k+j) - CV^{RT}(k+j)]^2 + \psi\left[\bar{L}_n(k+j) - \bar{L}_n{}^{RT}(k+j)\right]^2 + \zeta[\Delta u(k)]^2 \tag{3.7}$$

where the parameters δ and ψ are the weights of the outputs, and the parameter ζ is the weight of the increment input; the superscript RT indicates reference trajectory. The parameters δ, ψ and ζ were defined by trial and error, testing which parameters return answers with smaller offsets for the first trajectory studied. The input increment is defined by $\Delta u(k)$. H is the prediction horizon defined by analyzing the neural network's performance. The control horizon was defined as one.

The optimization constraints are given by Eq. 3.8 and Eq. 3.9, where C is the solute concentration, and C_s is the solute equilibrium concentration (Eq. 2.12). The process temperature was restricted to the range of 0 to 40 °C because it was the range applied in the training dataset. The constraint defined by Eq. 3.8 was defined to avoid sudden changes in temperature. Also, the constraint indicated by Eq. 3.9 was necessary because the phenomenological model was developed in supersaturation conditions for nucleation and growth.

$$-1\ °\mathrm{C} \leq \Delta u(k) \leq 1\ °\mathrm{C} \tag{3.8}$$

$$\frac{C(k)}{C_S(k)} \geq 1 \tag{3.9}$$

First, an NMPC controller was proposed using the developed ESNs as its internal model, called ESN-NMPC. In the control loop, the variables μ_0, μ_1, μ_2, μ_3, and C are measured at each sampling time. These measurements come from the PBM which represents here the real process. These results for moments are input for the four neural network models, which are the internal models for the controller. Then, an iterative procedure is carried out in which the network predicts the moment values several steps ahead using the given future temperature values. The neural network outputs are compared to the desired reference trajectory, composing the objective function. The optimizer applies the

Successive Quadratic Programming (SQP) algorithm to achieve the optimum temperature value for the control action. After convergence, the first control action is implemented. All cases were simulated for crystallization processes ending with 60 minutes in Python. The initial and final conditions of the simulations were based on Experiment 1 presented in the test dataset. The optimization problem was solved using the function *minimize* from the *SciPy* library[126]. The tolerances used in this optimizer were 10^{-10} for the absolute accuracy and 10^{-8} for the relative accuracy.

The performance of the ESN-NMPC was compared to an NMPC that uses the PBM as its internal model. Therefore, this controller was called PB-NMPC. The PB-NMPC was developed in Python using the Casadi library[127]. The control loop and the initial conditions were similar to the previous case. The optimization problem was solved using the IPOPT (Interior Point Optimizer) approach, defining a tolerance of 10^{-8}.

The controllers' performance was tested for three different set points. The first set-point chosen was $\bar{L}_n = 15\,\mu m$, and $CV = 1.05$, selected to study the controllers' performance in maintaining the crystal size close to the initial condition. Then, the controllers' performance was tested for maintaining the crystal size higher than the initial condition, defining a set point of $\bar{L}_n = 16.5\,\mu m$ and $CV = 1.0$. The final set point was selected to see the controllers' behavior for a crystal size smaller than the initial one, choosing a set point of $\bar{L}_n = 11\,\mu m$ and $CV = 1.2$.

3.2.3 Results and Discussion

The hyperparameters chosen for all networks were the same due to the R2 values near one for predictions one step forward for all train samples. Therefore, the four ESNs were designed to contain a single reservoir layer with 50 neurons, defining a noise value of 0.5 and a random state equal to 1.0. Also, the R^2 values were higher than 0.9 for all test samples and predictions one sampling time ahead.

The results for these networks are illustrated in Figure 3.5, where it is clear that the points are close to the black lines. This observation demonstrates that the proposed model can efficiently predict the moments one sampling time forward.

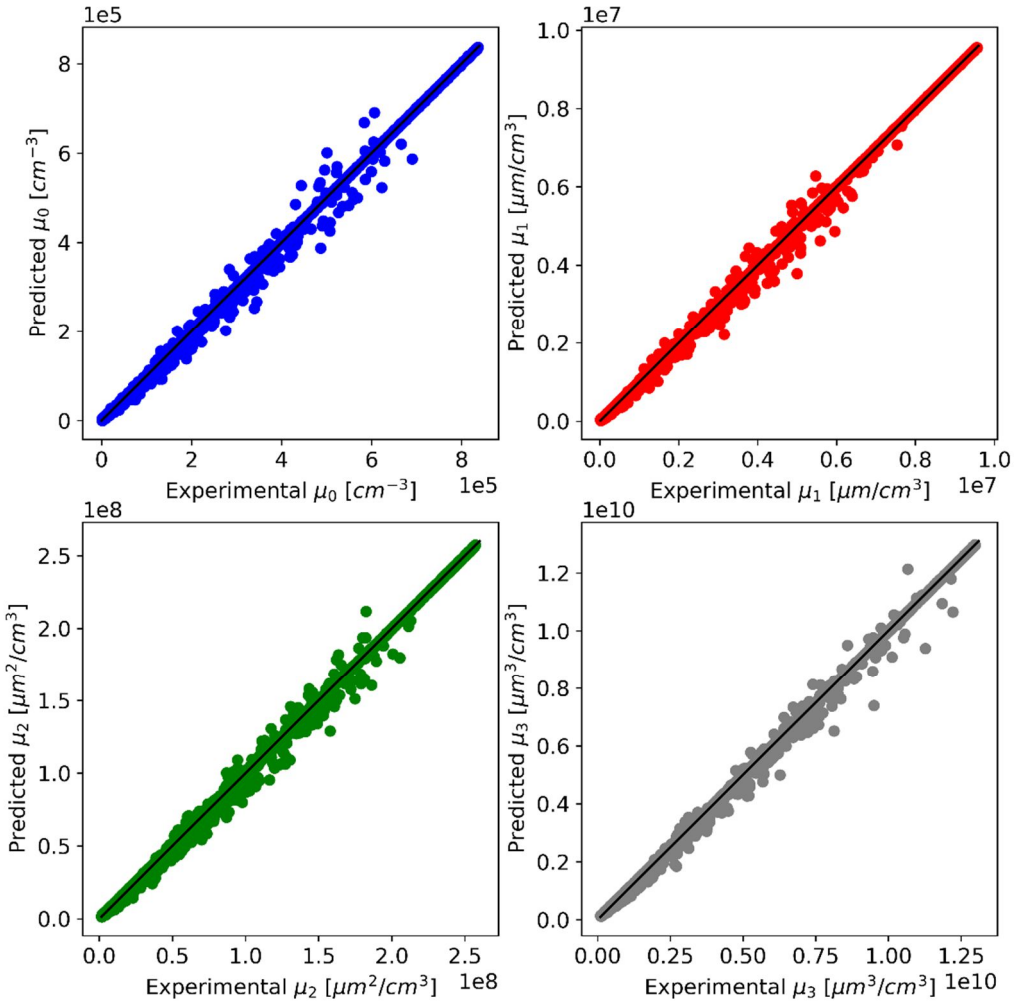

Figure 3.5 - Echo state networks performance for the moments' prediction one sampling time ahead, each color of dots representing the networks: blue for ESN 1, red for ESN 2, green for ESN 3, and gray for ESN 4.

The performance of the networks was tested for larger prediction horizons, making predictions of the moments two and five steps ahead. The results of this analysis are shown in Figure 3.6, presenting R^2 values higher than 0.7 for all networks, with a reasonable performance of the proposed approach. While

analyzing Figure 3.6, it is evident that the neural networks' performance deteriorates with the increase of the prediction horizon. The R^2 values are higher than 0.9 for predictions two steps ahead. The proposed approach did not present acceptable results for predictions higher than five steps compared to the current cases. The five-steps forward ESNs showed good prediction efficiency and were chosen as the surrogate model. This model was used as the internal model of the proposed NMPC to test the effectiveness of this approach with the PBM as the real process.

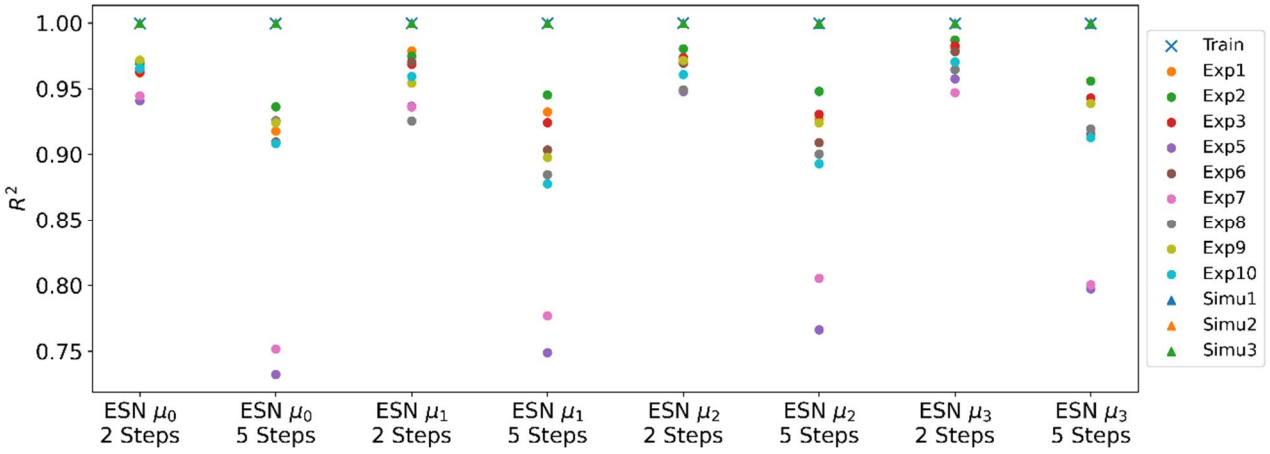

Figure 3.6 - R^2 values considering the four echo state networks predicting the moments two and five steps forward.

As shown in Eq. 3.7, we tuned the δ, ψ, and ζ parameters to 55, 10, and 0.002 for both controllers. Moreover, we used a control horizon of 1 and a prediction horizon of 5 in both cases. The results for all set points are shown in Figure 3.7. The controllers presented efficient performances for maintaining the controlled variables in their respective set points. For the CV, the ESN-NMPC presented an undershooting before reaching the trajectories in all cases, while the PB-NMPC just presented this behavior for the third case. However, both controllers could efficiently achieve the desired CV in all cases, being the PB-NMPC smoother in the trajectories. Considering the controlled variable $\bar{L}_n$, the controllers' responses presented oscillations before achieving the set points but all

the desired crystal sizes were efficiently reached. The behavior of the process temperature and the relative supersaturation ratio $C(k)/C_S(k)$ respected all the imposed constraints. Moreover, the ESN-NMPC presented comparable performance to the PB-NMPC in all cases, demonstrating the potential of the ESN-based approach.

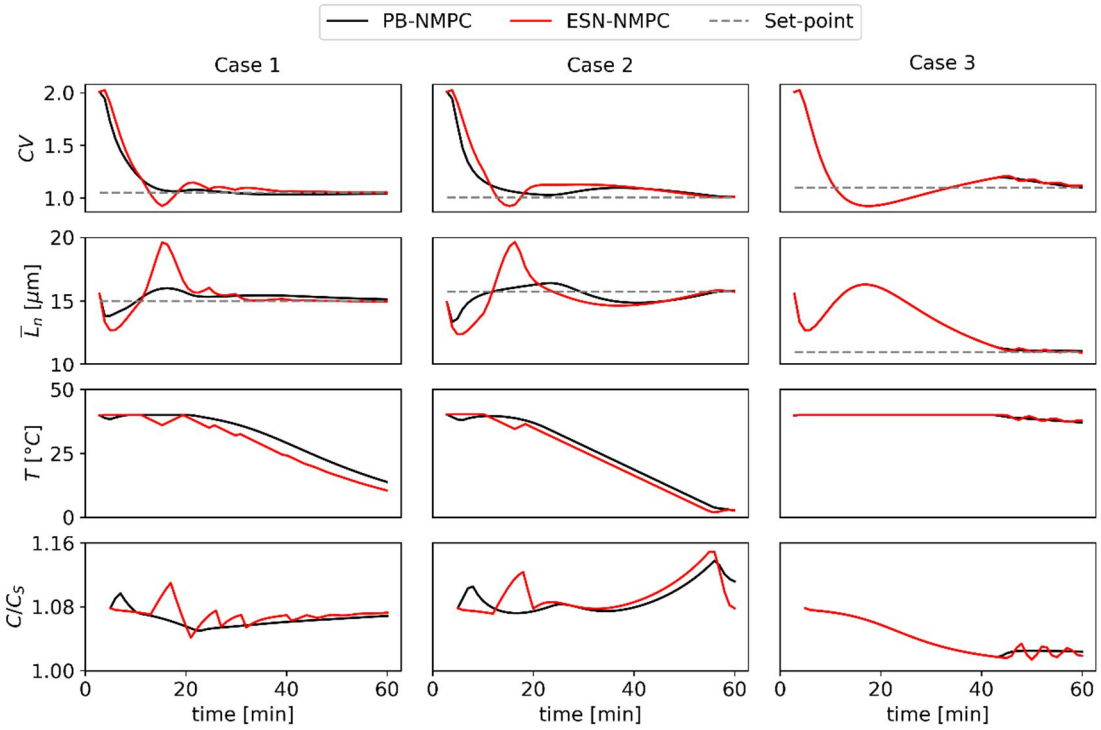

Figure 3.7 - Performance of the nonlinear model predictive controller based on population balance model (PB-NMPC) and the nonlinear model predictive controller based on echo state networks (ESN-NMPC) for the three cases of different set-points. Each column is a different scenario of set-points.

Table 3.5 shows the mean squared error (MSE) values calculated for both control approaches and all set points. In all cases, the controller based on the phenomenological model presented smaller MSE values. For the controlled variable CV, the MSE values were smaller because the PB-NMPC reached the set points faster than the ESN-NMPC. Considering the controlled variable L, the ESN-NMPC presents a peak before achieving the set points in all cases, which is

not observed in all cases of the PB-NMPC. However, the results presented in Table 3.5 are close for both approaches, demonstrating the good strategy developed using the ESN-NMPC.

Table 3.5 - Mean squared error for both control approaches and all set-points.

Set-point	PB-NMPC	ESN-NMPC
$\bar{L}_n = 15\ \mu m$	0.2856	1.9051
$\bar{L}_n = 16.5\ \mu m$	0.6317	2.9074
$\bar{L}_n = 11\ \mu m$	8.4324	8.4318
$CV = 1.05$	0.0507	0.0510
$CV = 1.0$	0.0542	0.0809
$CV = 1.2$	0.0479	0.0481

3.2.4 Conclusions

The proposed surrogate models based on ESNs could efficiently predict the four moments of the population balance model for the potassium sulfate batch crystallization, one, two, and five steps forward. For predictions one and two steps forward, the four ESNs presented R2 values higher than 90% for all test samples. Considering the ESNs for predictions five steps forward, the performance of the networks was worse compared to shorter horizons, but the R2 values were higher than 70% for all cases.

The developed ESNs were used as the internal model of an NMPC to maintain the coefficient of variation and the crystal's length in the desired values, manipulating the cooling temperature. The proposed NMPC could efficiently maintain the controlled variables in the desired set points. Moreover, the performance of the proposed NMPC was close to an NMPC based on the phenomenological model for the three set points. However, the NMPC based on

the phenomenological model presented lower MSE values in all cases. The benefits of using the developed surrogate neural network models for prediction and control can be highlighted since the ESNs are trained by applying a simple linear regression approach – also showing potential to be used in adaptative control schemes. At the same time, the phenomenological model needs more complex methods in the parameter estimation step.

3.3 Optimal Control of Crystal Size and Shape in Batch Crystallization

3.3.1 Introduction

In addition to the concern with the particle size, modeling for the shape (crystal habit) may be necessary and of progressive use in the development of predictive modeling and control of crystallization processes. However, controlling the particle shape presents an additional difficulty, both from the point of view of the model design and the measurement of important variables during the process. The number of control studies related to crystal shape is yet limited[49]. For these cases, the use of multidimensional PBM, in turn, presents greater complexity, mainly due to the difficulty of experimental measurements of the size of the crystals in multiple directions combined with possible computational difficulties for their solution.

The use of temperature cycling experiments (using growth-dissolution cycles) as a strategy to modify the crystal shape was studied in the past. Jiang et al. estimate both size-dependent growth and dissolution kinetics parameters in a 2D-PBM solved using the method of characteristics[128]. In that study, the authors predicted the crystal shape for the monosodium glutamate. Eisenschmidt et al. developed an optimal control scheme based on the temperature cycling strategy, showing experimentally the efficiency of controlling the crystal shape through two

dimensions of crystals of potassium dihydrogen phosphate (KDP)[46]. The size-independent growth and dissolution kinetics for KDP were previously estimated from experiments at constant supersaturation and undersaturation levels[129]. In that study, the authors defined a region in state space to track only the seed crystal evolution, thus disregarding nucleation and disappearance phenomena.

Regarding crystal shape control, a simulation control study that evaluated the effects of optimal control policies and spatial variations on crystal shape was performed[130]. A 2D-PBM considering only growth phenomenon for the L-glutamic acid was developed and applied experimentally in closed-loop feedback control for experiments with different control targets[131]. Using this same approach and still taking into account only the phenomenon of crystal growth, optimal temperature control, and optimal supersaturation control were compared in terms of performance in achieving the shape control targets in a real crystallizer for the L-glutamic acid[48]

A simulation study applying a less complex size and shape control approach that does not need kinetic models for a crystallization process considering only growth proves efficient[49]. This model-free approach, called path following control (PFC) proved attractive compared with more complex schemes such as NMPC (Nonlinear Model Predictive Control) that require the availability of growth rates. The experimental validation of PFC as a suitable feedback control scheme for shape was obtained for the β L-glutamic acid crystallization[132].

For crystal shape control in a continuous process, an NMPC was developed by Kwon et al. to control the shape of lysozyme crystals using a mixed suspension mixed product removal (MSMPR) reactor with a fine-particle trap[133]. Good results were obtained for the regulation of the average crystal aspect ratio operating in a growth cycle. The authors employed an 1D moment model for the crystal volume distribution. A feed-forward control was designed by Kwon et al. for the lysozyme crystals using a plug flow configuration, producing crystals with desired size and shape under feed flow disturbance rejection[134].

In this study, a bivariate population balance model (2D-PBM) was developed for KDP. The 2D-PBM was developed for supersaturated and undersaturated conditions, making it possible to use temperature cycling to achieve the desired product specification. The good agreement of the model prediction with experimental results makes the 2D-PBM approach attractive in optimal control strategy to reach targets of mass, size, and shape of KDP crystals.

3.3.2 Modeling and numerical approach

For modeling the morphology of KDP crystals, two characteristic dimensions called L_1 and L_2 were used as internal coordinates of the population balance equation (PBE). KDP crystals have a crystalline habit, as shown in Figure 3.8, and the choice of the two characteristic lengths was also used by Ma et al.[130] , Gunawan et al.[135] and Yang et al.[136].

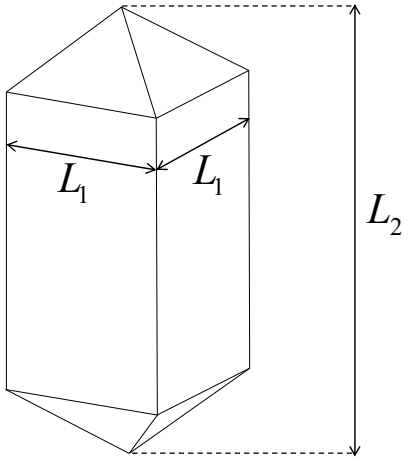

Figure 3.8 - KDP crystal and the characteristics lengths.

Taking into account these two internal variables in the state space, a bivariate number density distribution $n(L_1, L_2, t)$ is established, in $[(\mu m^2 \cdot cm^3\ of\ solvent)^{-1}]$. In this work, the relative supersaturation was considered as the driving force and input variable:

$$S = \frac{C}{C_s} \tag{3.10}$$

where C is the solute concentration and C_s is the solute equilibrium concentration, in $[g\ of\ solute\ /\ cm^3\ of\ solvent]$. The variation of the solvent density with temperature was neglected.

First, for supersaturated conditions ($S > 1$), the phenomena considered were the crystal growth and nucleation, and the PBE applied to the batch crystallizer yields:

$$\frac{\partial n}{\partial t} + \frac{\partial (G_1 n)}{\partial L_1} + \frac{\partial (G_2 n)}{\partial L_2} = B\ \delta(L_1)\ \delta(L_2) \qquad (S > 1) \tag{3.11}$$

where G_1 (Eq. 3.12) and G_2 (Eq. 3.13) are the crystal growth rates in $[cm/min]$; B (Eq. 3.14) denotes the nucleation rate in $[\#\ /\ (min\ \cdot\ cm^3\ of\ solvent)]$; and $\delta(\cdot)$ is the Dirac delta function.

$$G_1 = k_{g1} \exp\left(-\frac{E_{g1}}{RT}\right) (S-1)^{\alpha_{g1}} \tag{3.12}$$

$$G_2 = k_{g2} \exp\left(-\frac{E_{g2}}{RT}\right) (S-1)^{\alpha_{g2}} \tag{3.13}$$

$$B = k_b \exp\left(-\frac{E_b}{RT}\right) (S-1)^{\alpha_b}\ {M_T}^{\beta} \tag{3.14}$$

where k_{g1}, k_{g2}, and k_b are pre-exponential constants; E_{g1}, E_{g2}, and E_b are activation energies; M_T is the mass of crystals per solvent volume; α_{g1}, α_{g2}, α_b,

and β are exponent parameters; R is the universal gas constant; and T is the suspension temperature.

For undersaturated conditions ($S < 1$), the PBE yields:

$$\frac{\partial n}{\partial t} + \frac{\partial (D_1 n)}{\partial L_1} + \frac{\partial (D_2\, n)}{\partial L_2} = 0 \qquad (S < 1) \tag{3.15}$$

where D_1 (Eq. 3.16) and D_2 (Eq. 3.17) are the crystal dissolution rates in $[cm/min]$:

$$D_1 = -k_{d1} \exp\left(-\frac{E_{d1}}{RT}\right)(1 - S)^{\alpha_{d1}} \tag{3.16}$$

$$D_2 = -k_{d2} \exp\left(-\frac{E_{d2}}{RT}\right)(1 - S)^{\alpha_{d2}} \tag{3.17}$$

where k_{d1} and k_{d2} are pre-exponential constants; E_{d1}, E_{d2} are activation energies; α_{d1} and α_{d2} are exponent parameters.

In this case of S $<$ 1, the solute concentration is lower than the solubility, and crystals can dissolve continuously and in the extremal case, some fines may disappear.

Moments of the crystal size distribution were decided to be used as state variables (and also measured variables by image analysis) for the purpose of the crystal size and shape control in this work. Using the method of moments, the cross-moments $\mu_{i,j}$ defined in the space of two dimensions are given by:

$$\mu_{i,j} = \int_0^\infty \int_0^\infty {L_1}^i\, {L_2}^j\, n(L_1, L_2, t)\, dL_2 dL_1 \tag{3.18}$$

When applying the cross-moment integral transform operator to Eq. 3.11 and Eq. 3.15, the following cross-moment set of ODEs is obtained.

For $i, j \geq 1$:

$$\frac{d\mu_{i,j}}{dt} = i\, G_1\, \mu_{i-1,j} + j\, G_2\, \mu_{i,j-1} \qquad , \quad i,j \geq 1 \qquad (S \geq 1)$$
$$\frac{d\mu_{i,j}}{dt} = i\, D_1\, \mu_{i-1,0} + j\, D_2\, \mu_{i,j-1} \qquad , \quad i,j \geq 1 \qquad (S < 1) \tag{3.19}$$

The integral transformation for the moment equations of $\mu_{i,0}$ yields:

$$\frac{d\mu_{i,0}}{dt} = i\, G_1\, \mu_{i-1,0} \qquad (S \geq 1)$$
$$\frac{d\mu_{i,0}}{dt} = i\, D_1\, \mu_{i-1,0} + D_2 \int_0^\infty {L_1}^i\, n(L_1, 0, t)\, dL_1 \qquad (S < 1) \tag{3.20}$$

In the same way, for $\mu_{0,j}$:

$$\frac{d\mu_{0,j}}{dt} = j\, G_2\, \mu_{0,j-1} \qquad (S \geq 1)$$
$$\frac{d\mu_{0,j}}{dt} = j\, D_2\, \mu_{0,j-1} + D_1 \int_0^\infty {L_2}^j\, n(0, L_2, t)\, dL_2 \qquad (S < 1) \tag{3.21}$$

For the zeroth order cross moment $\mu_{0,0}$:

$$\frac{d\mu_{00}}{dt} = B \qquad (S \geq 1)$$
$$\frac{d\mu_{0,j}}{dt} = D_2 \int_0^\infty n(L_1, 0, t)\, dL_1 + D_1 \int_0^\infty n(0, L_2, t)\, dL_2 \qquad (S < 1) \tag{3.22}$$

For undersaturated conditions ($S < 1$), it was experimentally observed that $L_2 < L_1$ at any time (see Section 3.3.4) Therefore, the outgoing particle flux at the $L_2 = 0$ boundary, that is, $D_2\, n(L_1, 0, t)$ is zero, and the characteristic curves

leave the domain only at the $L_1 = 0$ plane. Consequently, the terms $D_2 \int_0^\infty {L_1}^i \, n(L_1, 0, t) \, dL_1$ in Eq. 3.20, and $D_2 \int_0^\infty n(L_1, 0, t) \, dL_1$ in Eq. 3.22 are null. Additionally, under the assumption that L_2 is close enough to zero when $L_1 = 0$, the high-order $(j > 0)$ moment fluxes $D_1 \int_0^\infty {L_2}^i \, n(0, L_2, t) \, dL_2$ in Eq. 3.21 can be neglected.

However, the evaluation of the flux $D_1 \int_0^\infty n(0, L_2, t) \, dL_2$ is needed in Eq. 3.22 to close the model. Defining the marginal density distribution $n_{L_1}(L_1, t)$ as

$$n_{L_1}(L_1, t) = \int_0^\infty n(L_1, L_2, t) \, dL_2 \tag{3.23}$$

this particle flux is given by $D_1 \, n_{L_1}(0, t)$. The equation for n_{L_1} is obtained by integrating Eq. 3.15 in the whole L_2 domain, being given by

$$\frac{\partial n_{L_1}}{\partial t} + D_1 \frac{\partial n_{L_1}}{\partial L_1} = 0 \qquad (S < 1) \tag{3.24}$$

where the particle flux $L_2 = 0$ was again not considered due to the experimental evidence that $L_2 > L_1, \forall \, t$. The numerical calculation of Eq. 3.24 is less laborious and have a lower computational cost when compared to the calculations of using Eq. 3.15. For Eq. 3.24, the high-resolution finite volume method ("HR-κ= -1 scheme") by Qamar et al. (2006) was employed. In this way, having the marginal density distribution at the boundary $L_1 = 0$ by solving Eq. 3.24, the number of particles that leave the domain per solvent volume, $N_d \, [1/cm^3]$, can be accounted during a sampling time Δt by the following integral

$$N_d \, (t) = - \int_{t - \Delta t}^{t} D_1 \, n_{L_1}(0, \xi) d\xi \tag{3.25}$$

Thus, Eq. 3.22 for $S < 1$ can be explicitly integrated in one time step to give

$$\mu_{0,0}(t) = \mu_{0,0}(t - \Delta t) - N_d \tag{3.26}$$

In order to relate third order cross-moments with the mass of crystals and solute concentration, the volume of a single KDP crystal, V_c, can be expressed by[130]

$$V_c(t, L_1, L_2) = L_2 {L_1}^2 - \frac{2}{3} {L_1}^3 \tag{3.27}$$

In this way, the mass of crystal per solvent volume M_T can be expressed by:

The crystal mass balance can be defined, in the same manner by:

$$\frac{dm_c}{dt} = \rho_c \frac{dV_c}{dt} \tag{3.28}$$

Using Eq. 3.27 and the definition of the growth/dissolution rates:

$$\begin{aligned} \frac{dm_c}{dt} &= \rho_c \left[\left(2L_1 L_2 - {L_1}^2 \right) \right] G_1 + {L_1}^2 G_2 \qquad (S \geq 1) \\ \frac{dm_c}{dt} &= \rho_c \left[\left(2L_1 L_2 - {L_1}^2 \right) \right] D_1 + {L_1}^2 D_2 \qquad (S < 1) \end{aligned} \tag{3.29}$$

By a mass balance and integrating Eq. 3.29 in the whole internal variable domain, the solute concentration equation can be represented by:

$$\frac{dC}{dt} = \rho_c \left(2\, G_1 \mu_{1,1} - G_1\, \mu_{2,0} + G_2\, \mu_{2,0} \right) \qquad (S \geq 1) \tag{3.30}$$

$$\frac{dC}{dt} = \rho_c(2\,D_1\mu_{1,1} - D_1\,\mu_{2,0} + D_2\,\mu_{2,0}) \qquad (S < 1)$$

By switching the model for each zone, the developed approach can describe the system behavior as the temperature is increasing, causing dissolution and disappearance of KDP crystals, and decreasing, causing crystal growth and nucleation.

Crystallization and dissolution experiments for KDP (Synth, $>$ 99%) in distilled water were performed in the same crystallization apparatus described in Chapter 2 (details in Section 2.2).

For the crystalline phase information, the moments that appear in the equations above, $\mu_{0,0}$, $\mu_{0,1}$, $\mu_{1,0}$, $\mu_{1,1}$, $\mu_{2,0}$, $\mu_{2,1}$, and $\mu_{3,0}$ were processed from the results of the image analysis, now taking into account the two Feret diameters d_{F^+} and d_{F^-} for the bivariate distribution n ($d_{F^-} = L_1, d_{F^+} = L_2$).

Based on the structure of the models presented in this section, the kinetic parameters for nucleation, growth, and dissolution were estimated for KDP for a given set of experiments in the same manner as described in details in Section 2.2.

Once the deterministic model was obtained, the dynamic optimization problem described by Grover et al. (2020) was solved to obtain optimal control policies to produce KDP crystals with desired mass, size, and shape for deterministic simulations. The supersaturation was used as the control input in this strategy.

In this way, with a primary objective of reaching a target state position, the optimal control input policy can be expressed as follows[137]

$$\{u_0{}^*, \dots, u_{N-1}{}^*\} = \operatorname{argmin}\left\{\sum_{\tau=0}^{N-1}[(t_\tau/t_N)^\gamma\, d(\boldsymbol{x}_\tau, \boldsymbol{x}^{\oplus}) + \rho\, u_\tau{}^2 + d(\boldsymbol{x}_N, \boldsymbol{x}^{\oplus})]\right\} \qquad (3.31)$$

$$s.t. \qquad \dot{\boldsymbol{x}}_\tau = \boldsymbol{f}(\tau, \boldsymbol{x}_\tau, u_\tau)$$

where $\{u_0{}^*, \ldots, u_{N-1}{}^*\}$ is the optimal control policy; ρ and γ are tuning parameters; $d(\boldsymbol{x}_\tau, \boldsymbol{x}^{\oplus})$ is the distance-to-target function; $\boldsymbol{f}$ is the model.

The control vector state for the KDP mass-size-shape-control was

$$\boldsymbol{x} = [m \quad \bar{L}_1 \quad \bar{L}_2]^T \tag{3.32}$$

where m is the mass of crystals; $\bar{L}_1$ and $\bar{L}_2$ are the number mean characteristic lengths:

$$\begin{aligned} \bar{L}_1 &= \mu_{1,0}/\mu_{0,0} \\ \bar{L}_2 &= \mu_{0,1}/\mu_{0,0} \end{aligned} \tag{3.33}$$

The dynamic optimization problem of Eq. 3.31 was solved offline for a discretized set of states, in Eq. 33, and input (supersaturation setpoints).

The solutions of Eq. 3.31, supersaturation policies, are stored for each time and state. For a practical control scheme, the temperature can be chosen as manipulated variable. For that, from the supersaturation policies, the temperature policies was obtained by inversion using the solubility equation.

Complementary deterministic simulations (ideal case with no process-model mismatch) for KDP mass-size-shape control were performed using the calculated control policies. Reachable targets that span a considerable portion of the state space were set and shown in Section 3.3.3.

In order to evaluate the polydispersity of the crystal size distribution, the coefficients of variation CV_1 and CV_2 of the marginal distributions n_{L_1} and n_{L_2}, respectively, were determined by Eq. 3.34.

$$CV_1 = \sqrt{\frac{\mu_{2,0}\,\mu_{0,0}}{{\mu_{1,0}}^2} - 1}$$

$$CV_2 = \sqrt{\frac{\mu_{0,2}\,\mu_{0,0}}{{\mu_{0,1}}^2} - 1} \tag{3.34}$$

3.3.3 Results and Discussion

Table 3.6 presents the kinetic parameters estimated. Based on experimental evidence that $L_2 > L_1, \forall\, t$, as mentioned in Section 3.3.2, tal observação pode ser facilmente verificada ao comparar as taxas de dissolução D1 e D2. Defining the relative dissolution rate by $D_{rel} = D_1 \,/\, D_2$, Figure 3.9 presents D_{rel} values for the operating range of supersaturation and temperature ($20 \leq T \leq 40$ e $0{,}8 \leq S \leq 1$).

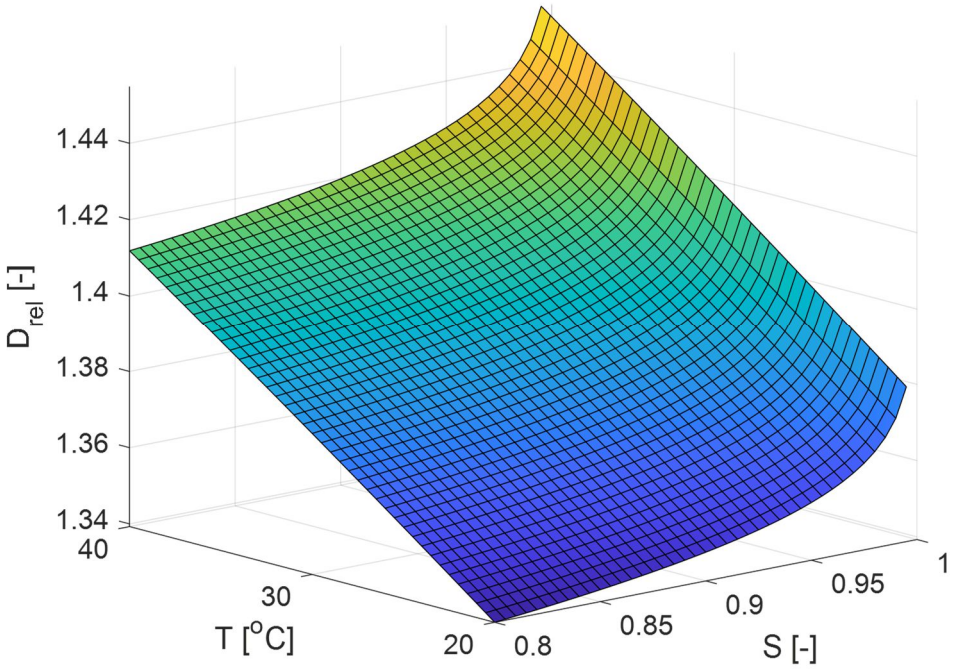

Figure 3.9 - Relative dissolution rate of KDP

Table 3.6 - Estimated parameters for KDP crystallization and dissolution

Parameter	Meaning	Value	95% CI
k_b	nucleation rate constant $[(min \cdot cm^3)^{-1}]$	3.0966×10^{15}	$\pm$ 2.9847×10^{13}
E_b	nucleation activation energy $[J/mol]$	5.8012×10^4	$\pm$ 2.9834×10^2
α_b	nucleation supersaturation exponent $[-]$	0.9658	$\pm$ 0.0085
β	nucleation M_T exponent $[-]$	1.964	$\pm$ 0.06041
k_{g1}	growth rate constant of L_1 $[(\mathrm{cm/min})]$	7.8354×10^4	$\pm$ 9.9410×10^2
E_{g1}	growth activation energy of L_1 $[J/mol]$	3.9144×10^4	$\pm$ 6.6217×10^2
α_{g1}	growth S exponent of L_1 $[-]$	1.5605	$\pm$ 0.04014
k_{g2}	growth rate constant of L_2 $[(\mathrm{cm/min})]$	4.5361×10^5	$\pm$ 3.4602×10^3
E_{g2}	growth activation energy of L_2 $[J/mol]$	4.1129×10^4	$\pm$ 3.2846×10^3
α_{g2}	growth S exponent of L_2 $[-]$	1.8104	$\pm$ 0.1002
k_{d1}	dissolution rate constant of L_1 $[(\mathrm{cm/min})]$	8.5032×10^2	$\pm$ 9.1474
E_{d1}	dissolution activation energy of L_1 $[J/mol]$	2.9068×10^4	$\pm$ 5.1746×10^3
α_{d1}	dissolution S exponent of L_1 $[-]$	0.9638	$\pm$ 0.01064
k_{d2}	dissolution rate constant of L_2 $[(\mathrm{cm/min})]$	2.8152×10^2	$\pm$ 6.9047
E_{d2}	dissolution activation energy of L_2 $[J/mol]$	2.7068×10^4	$\pm$ 2.4518×10^2
α_{d2}	dissolution S exponent of L_2 $[-]$	0.9719	$\pm$ 0.008149

In this way, D_1 is always greater than D_2 in the operating range under study. As the characteristic length L_2 is greater than L_1 in the initial times, this implies that L_2 will never be less than L_1 in the studied cases. Thus, when crystals disappear, they will disappear from the domain in the plane $L_1 = 0$.

To demonstrate the adequacy of the developed model, experimental results obtained for KDP crystallization/dissolution experiments in 2 experiments are presented for model validation in Figures 3.10. Supersaturation and undersaturation regions were investigated, respectively, showing satisfactory results for model predictions. The model adequately captured the growth and nucleation kinetics for supersaturation zones and dissolution and disappearance for undersaturation zones.

In Figure 3.10, it is possible to see that, in addition to the crystal growth (by increasing the characteristic lengths), an increase in $\mu_{0.0}$ indicates that the formation of new nuclei has occurred. For the 3–35-minute time interval, a notable deviation between predicted and experimental data in $\mu_{0.0}$ may be explained by the more significant deviation between the calculated temperature policy and that performed experimentally in that time interval. Experimentally, this may have occurred due to a nonuniform temperature field in the vessel since this large initial value of S requires a fast decrease in the cooling jacket temperature.

As for the undersaturation condition experiment in addition to the shrinkage of the crystals, it is exemplified that the strategy adopted in this work to deal with the disappearance of the crystals is effective, due to the good prediction of the model to decrease $\mu_{0.0}$. This strategy was well established because it is defined in the boundary condition for null lengths. It is a proper way to store the number of crystals that disappeared (leave the domain) and, thus, make it possible to correct the distortion at the zeroth order moment.

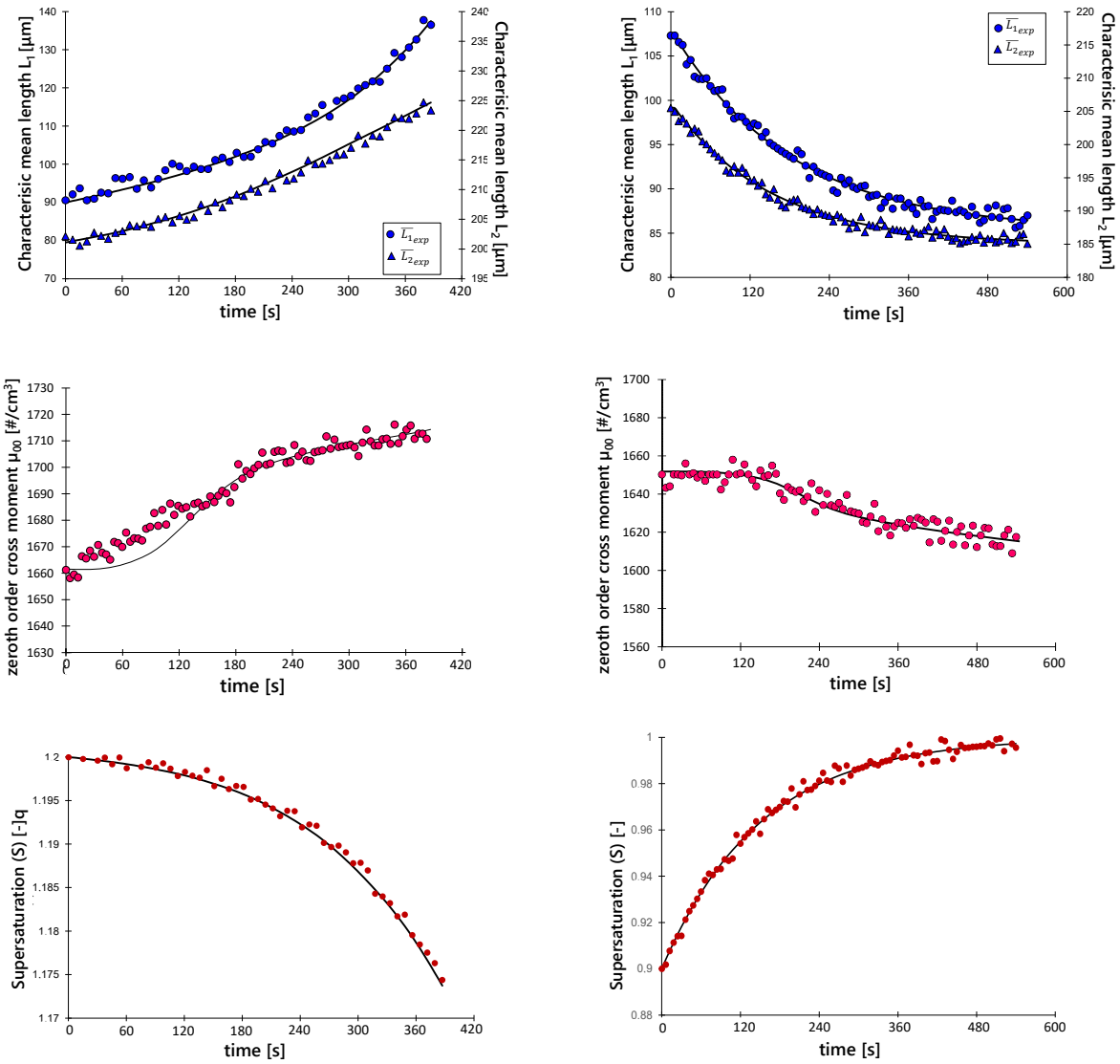

Figure 3.10 - Precited and experimental values for supersaturation zone experiment: characteristic mean lengths (left), zeroth order cross-moment (middle) and supersaturation (right). Black lines represent the values predicted by the model.

The simulation results for optimal control is now discussed. Table 3.7 shows the run targets and batch times for the 3 deterministic runs performed. The choice of the spatial orientation using the three variables in Eq. 3.32 allows better visualization of the crystallization trajectory. Using this plot, in addition

to checking the yield (mass) of the process, it is possible to follow both the average characteristic lengths $\bar{L}_1$ and $\bar{L}_2$ (indicating the crystal size).

Table 3.7 - Deterministic runs evaluated for KDP control

	target $x^{\oplus}$ [g, μm, μm]	Batch time [min]
Run 1	[6, 200, 400]	90
Run 2	[8, 60, 200]	90
Run 3	[10, 100, 150]	90

In this way, it is possible to monitor the relative position of $\bar{L}_1$ and $\bar{L}_1$ along the batch, which indicates the change in the crystal shape by altering the slope of the trajectory, analyzing the $\bar{L}_1 \times \bar{L}_2$ plane. It is illustrated by the simulation results for the three runs in Fig. 3.11.

It is possible to observe different behavior of the trajectory depending on the required final target due to the implemented inputs. For Run 1, it only operates in supersaturation, obtaining a more straight-forward trajectory, indicating both increased yield and growth of the crystals until they reached the desired size and shape. For Run 2 and Run 3, the trajectory is perceived in areas of supersaturation and undersaturation.

The temperature policies were obtained from the supersaturation optimal policies combining them with the calibration and equilibrium equations. Furthermore, the simulated control could eliminate the error in the final crystal specification (distance from the target is near zero).

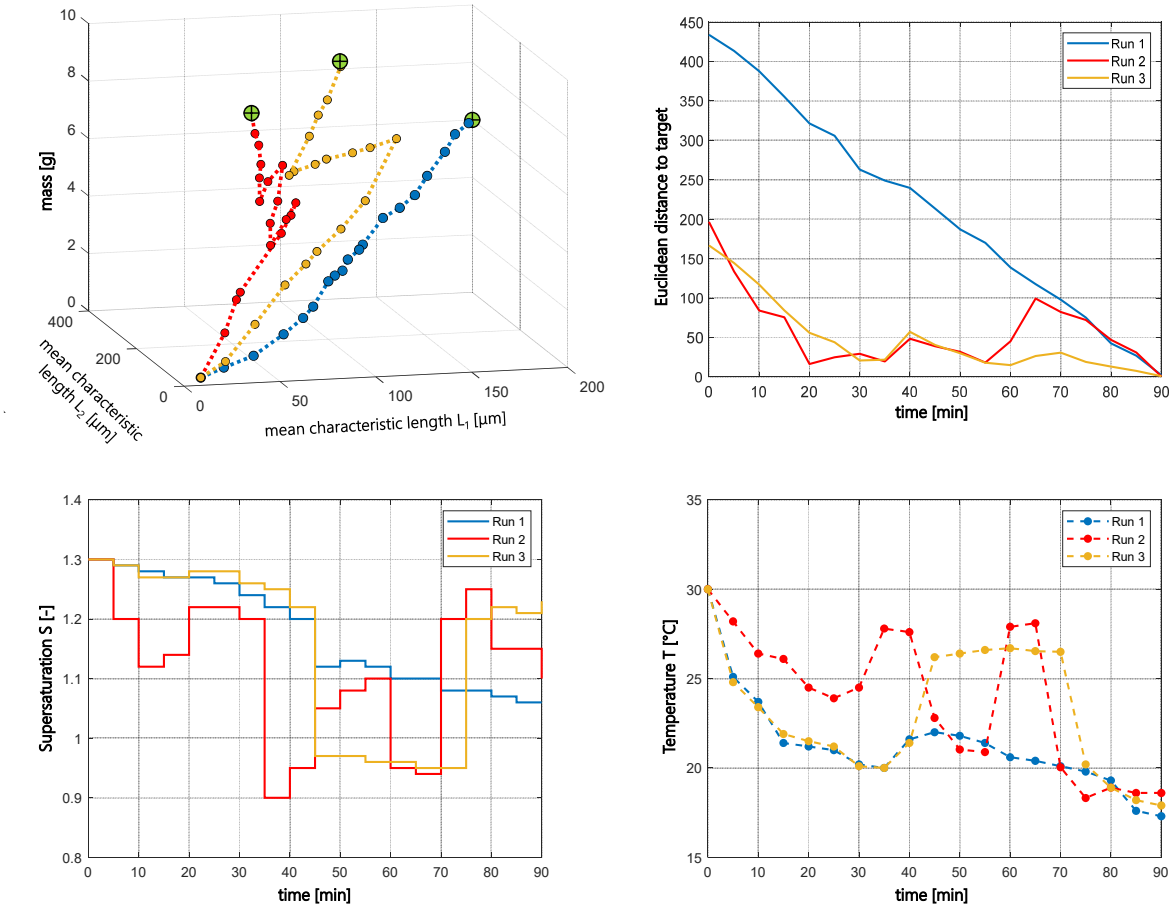

Figure 3.11 - Simulation results for optimal control of KDP. Above: state trajectories (left); Euclidean distance to target (right). Below: supersaturation optimal control actions (left); temperature policies calculated by supersaturation policies (right).

When verifying the crystal shape, Figure 3.12 shows that for Run 1, the crystal aspect ratio does not vary significantly over time, indicating that the crystal growth in both directions follows a similar rate while there is an increase in mass until the target is reached. For Run 2 and Run 3, the most pronounced variation in the trajectory inclination (i.e. aspect ratio) is noticeable when changes are made between the regions of $S > 1$ and $S < 1$.

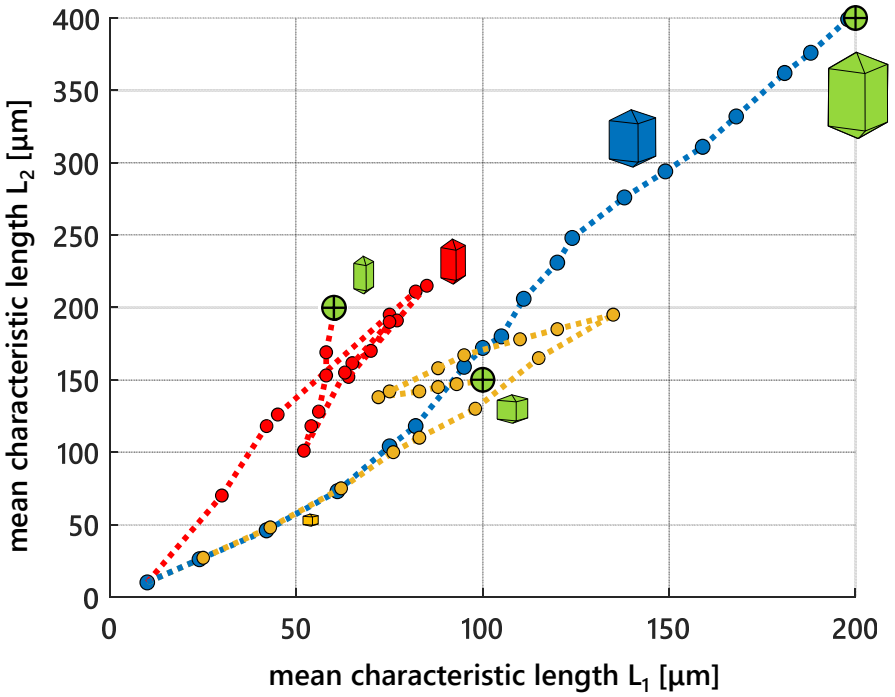

Figure 3.12 - L_1 x L_2 plot. Changes in trajectory slope indicate that aspect ratio changes. Targets are in green. Some scale representations of KDP crystals at different positions in space are shown

The evaluation of the crystals' polydispersity is shown in Figure 3.13. For the three runs, the coefficients of variation CV_1 and CV_2 show satisfactory results. The values at the end of the batches do not significantly vary compared to the values for the seeds (at the beginning of each run). Furthermore, individually for each run, the trends of CV_1 and CV_2 had a similar profile. Run 1, which operated only with cooling ($S > 1$), showed a more significant increase in the polydispersion of the final product. For Run 2 and Run 3, since the trajectory assumes regions of undersaturation ($S < 1$), maybe it might be possible to control the coefficients of variation for these regions where there is dissolution. It can be explained by the possibility of removing small-size crystals (fines removal), narrowing the crystal size distributions. When there is undersaturation, the sensitivity of CV_1 and CV_2 is indicated by the plateau regions in Figure 3.13. It is worth noting that for Run 2, the coefficients of variation for the final product

show less polydispersity, which can be explained by the fact that dissolution occurred twice during this batch.

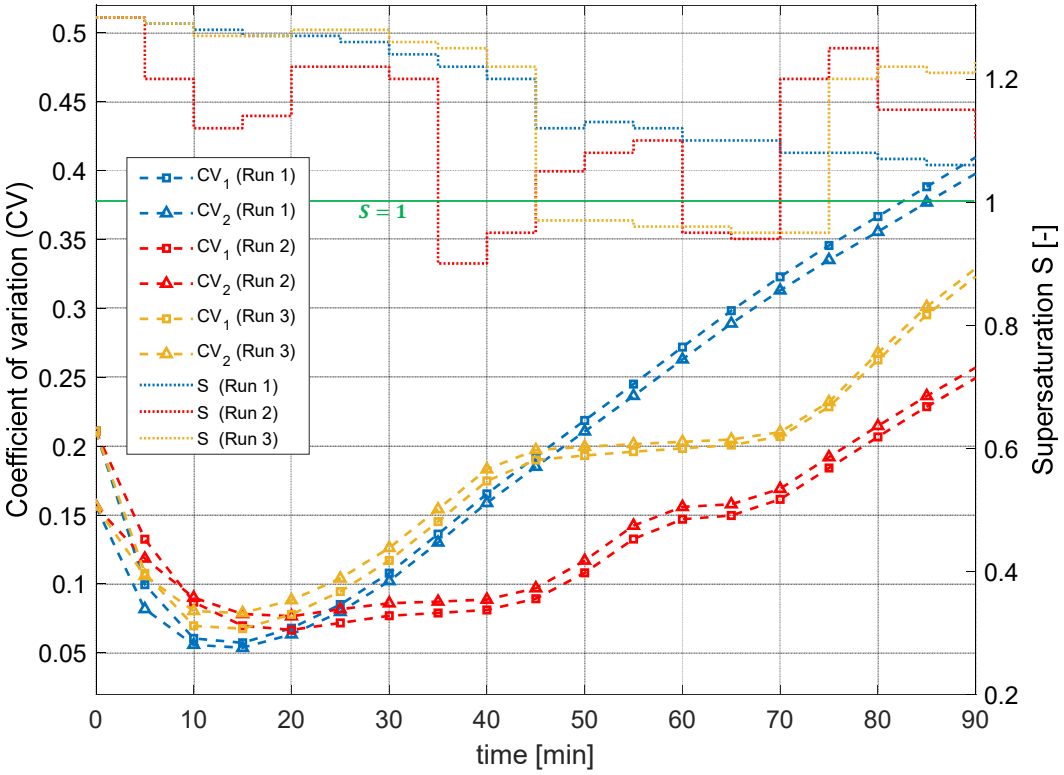

Figure 3.13 – Coefficients of variation CV_1 and CV_2 throughout the runs for the optimal control of KDP with the respective supersaturation (S) levels.

3.3.4 Conclusions

The theoretical model based on a 2D-PBM that incorporates nucleation and growth (in supersaturation zones) and dissolution and disappearance (in undersaturation zones) was obtained for KDP. It showed good predictions for open-loop batch crystallization experiments. The presented optimal control strategy application is suitable for closed-loop control, calculating the temperature setpoints based on the obtained optimal supersaturation policies. It is expected that this approach will be applied to different compounds and measuring techniques, to investigate not only the mass and size, but also the crystal shape.

Chapter 4

Polymorphism of Praziquantel by Cooling Crystallization

This chapter presents a systematic study to investigate the polymorphism of praziquantel – an anthelmintic first-line drug – using cooling crystallization experiments under different conditions not yet explored in the literature for this compound. All forms previously reported, obtained via mechanochemistry and the hydrate found through supercritical CO_2 processing, were accessed in the present work. A novel dimethylacetamide (DMA) solvate was obtained, and a new form was discovered after desolvation of the DMA solvate by aging and exposure to a water-vapor atmosphere. Toluene and triethylamine were solvents capable of enabling the formation of different forms depending on the employed experimental condition. A new form was discovered using triethylamine as the solvent, which differs from all known polymorphs. The results demonstrate that solvent selection and variation in the rate of supersaturation generation can generate forms obtained from more complicated techniques and potentially finding new forms.

The chapter was adapted from the following published paper:

i. de Moraes, M. G. F.; Barreto, A. G.; Secchi, A. R.; de Souza, M. B.; Lage, P. L. da C.; Myerson, A. S. Polymorphism of Praziquantel: Role of Cooling Crystallization in Access to Solid Forms and Discovery of New Polymorphs. Crystal Growth & Design **2023**, 23 (2), 1247–1258.

4.1 Introduction

Regarding using crystallization methods for exploring new polymorphs of praziquantel, Toro et al. unsuccessfully tried to obtain polymorphic modifications of praziquantel by slow evaporation with different solvents (water, ethanol, methanol, 2-propanol, 1,2-ethanediol, and DMSO, among others), obtaining the original Form A in all experiments[138]. Saikia et al. also reported data on PZQ polymorph screening by slow evaporation crystallization, obtaining only Form A[66]. Therefore, the polymorph screening using solution crystallization was reported for the slow evaporation of a few solvents, not exploring other crystallization methods.

In this work, we applied cooling crystallization to investigate the polymorphism of racemic praziquantel using different solvents and using a medium-throughput systematic screening methodology. The choice of solvents with different properties were done based on reported grouping techniques by statistical analysis[139,140]. The authors took into account cluster statistical analysis to separate a large number of solvents into groups, taking into account parameters such as hydrogen bond acceptor propensity, hydrogen bond donor propensity, polarity/dipolarity, dipole moment, dielectric constant, viscosity, surface tension and cohesive energy density[140], and used 24 solvent descriptors to obtain self-organizing maps[139].

Our investigation led to the discovery of a DMA monosolvate (named PZQ-DMA) and two new anhydrous forms (named Forms G and H, following the naming convention by the last works). In addition, all previous well-characterized forms could be obtained for the first time via solution crystallization techniques: Forms B, C, two hydrates, and the acetic acid monosolvate. We confirmed that the hydrate first obtained through supercritical CO_2 processing[86] is a second hemihydrate besides the hemihydrate PZQ-HH indexed as WUHQAU[70]. The obtained Form G was only possible via desolvation of PZQ-DMA, more efficiently

via exposure to a water vapor atmosphere. Desolvation is known to be even the only way to prepare new polymorphs previously not accessed by crystallization methods[141-145].

As such, the praziquantel case study evidenced the role of cooling crystallization as an excellent method to access and discovers new forms for APIs. Our work highlights the advantages of using cooling crystallization over grinding techniques to obtain better reproducibility and easy-to-run experiments for a systematic polymorph screening.

4.2 Experimental Section

4.2.1 Materials

Praziquantel ($C_{19}H_{24}N_2O_2$), 2-(cyclohexanecarbonyl)-3,6,7,11b-tetrahydro-1H-pyrazino[2,1-a]isoquinolin-4-one, was purchased from TCI America™ (>98.0%, HPLC). This commercial praziquantel was the starting solid for the experiments and corresponds to Form A (indexed as TELCEU in the Cambridge Structural Database). Ultrapure water from a purification system (Thermo Scientific™ Barnstead™ Micropure™ UV) and HPLC-grade solvents from Sigma-Aldrich® were used for crystallization experiments.

4.2.2 Analytical instruments and characterization

Powder X-ray diffraction (PXRD) patterns were obtained using a PanAnalytical X'Pert Pro diffractometer. Differential scanning calorimetry (DSC) and Thermogravimetric analyses (TGA) were carried out using a DSC Q2000 (TA Instruments, USA) and a TGA Q5000 (TA Instruments, USA), respectively. The methodology details can be found in the Appendix A.

Karl Fischer (KF) coulometric titration was conducted to determine the water content in hydrates using a Metrohm 831 KF Coulometer and Aquastar™

CombiCoulomat Fritless KF Reagent (Merck). Procedure details with samples, blank and the water standard are in Appendix A.

The morphology of some of the PZQ crystals was characterized with scanning electron microscopy (SEM) using Zeiss Merlin® High-resolution SEM (details in Appendix A).

4.2.3 Cooling crystallization of PZQ from single solvents

Crystal16™ device (Technobis Crystallization Systems) was used for all the cooling crystallization conditions performed in the polymorph screening. This medium-throughput screening equipment used microvial crystallizers of 1.5 mL (11.5 mm diameter, flat-bottomed).

In the first screening, a total of $4 \times 19 = 76$ solutions of PZQ were prepared. The 19 pure solvents are listed in Table A.1. For the experimental design, two levels for the initial concentration (low and high, see Table A.1) and two for the cooling rate were defined. Slow (0.2 ^{o}C/min) and fast (5 ^{o}C/min) cooling rate levels were adopted.

The solutions were prepared by weighing the amount of PZQ and solvent in the microvials. In order to estimate the initial concentration, exploratory solubility tests were carried out using the Crystal16™ device for all solvents. The estimated concentration values can be found in Appendix A (Table A.2).

The saturation temperatures corresponding to the initial condition levels are shown in Table A.1 for the different solvents. The solutions were heated to 5 ^{o}C above the saturation temperature, and maintained at this value for 60 min to ensure complete dissolution. The light transmission was also monitored as a sign of solubilization of the clear solutions (100% transmission). The high temperature levels took into account the operation below the boiling point of the solvents. All the solutions were then filtered using heated 0.2 µm PTFE syringe filters and 1 mL syringes and placed in new clean heated vials at the same temperature to ensure starting from clear solutions. Stirring was kept constant at 700 rpm using

magnetic stirring with PTFE agitation bars throughout the experiments. Then, solutions were cooled to the final temperatures at the specified cooling rate. The final temperature set for the cooling ramps was mostly -10 °C, and this value was changed for some solvents to ensure a temperature higher than their melting points (Table A.1).

The Crystal16™ device detected the nucleation event as a drop in light transmission through each vial. Once the crystals were formed in a reasonable amount for further analysis and characterization, they were harvested and put in a vacuum system to rapidly eliminate all the remaining solution. The crystals were immediately analyzed by PXRD, DSC and TGA.

4.2.4 Cooling crystallization of PZQ from alcohol/water mixtures

Based on some observations from the experiments in Section 4.2.3, mixtures of water/methanol and water/ethanol at water volume fractions of 10, 20, 30, 40, and 50 v% were chosen as the solvent for the praziquantel cooling crystallization using a fast cooling rate (5 °C/min). The initial solution was saturated at 40 °C and then heated to 45 °C to ensure complete dissolution. The filtration procedure described in Section 4.2.3 was performed to ensure initial clear solutions. The final temperature set for the cooling ramp was -10 °C. The crystals were rapidly dried upon crystallization and subjected to PXRD, DSC, and TGA analysis.

4.2.5 Water vapor diffusion experiments

The two solvates obtained by the cooling crystallization described in Section 4.2.3 were DMA and acetic acid (AA) solvates (see Section 4.3.1). In order to better study the role of the solvents in the crystal structures, the two solvates were subjected to water vapor diffusion experiments. The materials were left in contact with the water vapor overnight. Details about the apparatus and vapor diffusion procedure can be found in SI

4.3 Results and Discussion

4.3.1 Polymorphic outcome from single solvents

Once the drop of the transmission confirmed the nucleation through the microvials, all the outcome crystals were characterized by PXRD analysis. In the single solvent screening, the observed forms of praziquantel are presented in Table 4.1 for each experimental condition. The more stable form (Form A) was mainly observed for the different solvents and adopted levels of the cooling ramp and initial concentration. For PZQ, in the literature, only Form A was obtained in crystallization experiments, but only crystallization by solvent evaporation was performed in those works[66,138].

Among the results presented in Table 4.1, the experiments using the following solvents stand out: DMA, acetic acid, toluene, and triethylamine. Using DMA, the formation of a novel solvate (PZQ-DMA) was observed under rapid cooling conditions. The effect of the cooling rate using DMA as solvent is decisive, with the stable Form A being favored when the cooling rate is slower Figure 4.1 shows the PXRD pattern for the novel DMA solvate compared to the simulated powder patterns of the anhydrous forms of PZQ, allowing a clear identification of this polymorph due to the pattern differences.

Table 4.1 - Polymorph screening results of PZQ in different solvents

Solvent	Fast cooling (5 °C / min)		Slow cooling (0.2 °C / min)	
	Initial concentration			
	Low	High	Low	High
Acetone	A	A	A	A
Methanol	A	A	A	A
Ethanol	A	A	A	A
1-Propanol	A	A	A	A
Isopropanol	A	A	A	A
1-Butanol	A	A	A	A
Ethyl acetate	A	A	A	A
Dimethylformamide	A	A	A	A
Dimethylacetamide	PZQ-DMA	PZQ-DMA	A	A
Tetrahydrofuran	A	A	A	A
Acetonitrile	A	A	A	A
Toluene	A	A/C	A	A
1,4-dioxane	A	A	A	A
Acetic Acid	PZQ-AA	PZQ-AA	PZQ-AA	PZQ-AA
Triethylamine	C	C	C	C
Dichloromethane	A	A	A	A
Anisole	A	A	A	A
Dimethyl sulfoxide	A	A	A	A
2-butanone	A	A	A	A

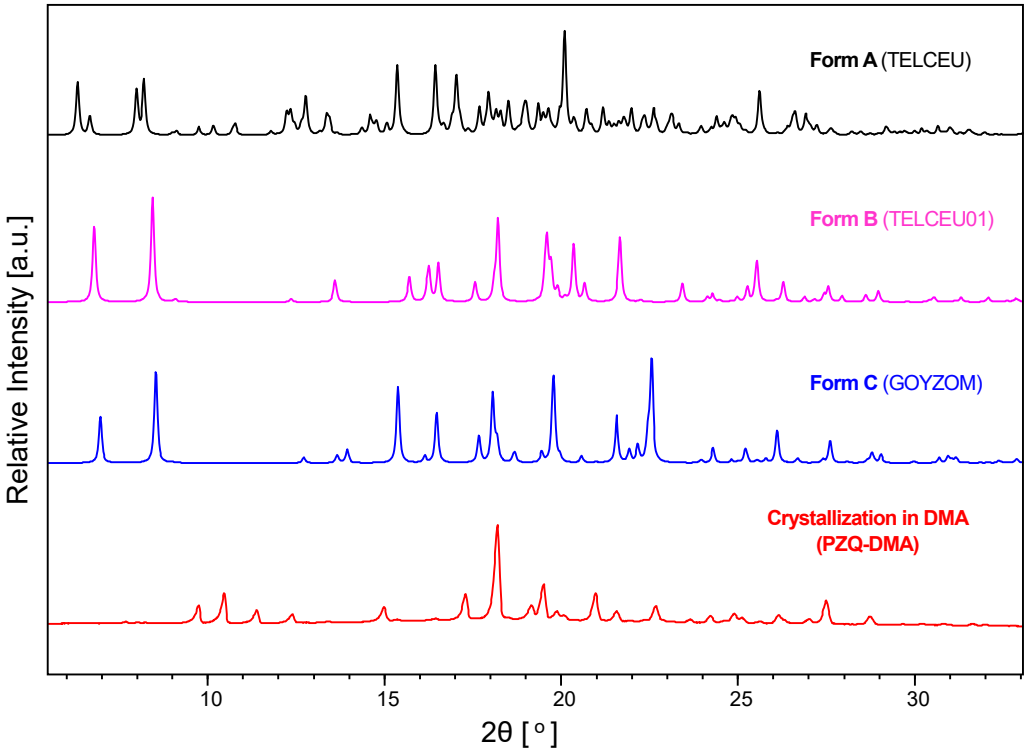

Figure 4.1 - PXRD pattern for PZQ-DMA and comparison with Forms A, B, and C.

Through thermal analysis (Figure 4.2), it was possible to prove that the new PZQ-DMA form obtained is a solvate. The DSC curve (red line) indicates an endothermic peak desolvation at 58 °C (87.16 kJ/mol). After desolvation, other endothermic events were recorded at the DSC at 132.57 °C and 138.36 °C, and identified as melting events. The first melting peak does not correspond to any previously reported anhydrous form, being a new form (Form G), which will be further discussed in Section 4.3.2. The second melting event corresponds to the most stable form (Form A). The commercial PZQ (Form A) was previously analyzed under the same conditions and presented a melting point of 138.90 °C. The desolvation of DMA is confirmed by the weight loss in the TGA, which was approximately 20%. It agrees with the theoretical value of 21.2% for a PZQ-DMA monosolvate. The weight loss started at around 56 °C, confirming the desolvation event observed by the endothermic peak in DSC.

Figure 4.3 shows the SEM images obtained for the forms A and fresh PZQ-DMA. The SEM images were acquired on the same day of the crystallization experiment. The PZQ-DMA exhibits different habitus morphology, showing lath-shaped crystals, differing from the crystals of Form A (smaller acicular crystals). For the experiments using acetic acid as solvent, the acetic acid solvate (PZQ-AA) was obtained in all experimental conditions, confirmed by comparison with the simulated powder pattern DAJCEA[71] (Figure A.2). PZQ-AA was first obtained by Zanolla et al. via liquid-assisted grinding using a vibrational mill[71]. The DSC curve of PZQ-AA (blue curve) is shown in Figure 4. 2, characterized by a single endothermic event at 72.19 °C. Zanolla et al. reported this event (peak at 72.26 °C) as the melting point of PZQ-AA, also confirmed by hot-stage microscopy[21]. Before starting thermal decomposition, a mass loss of 15.60% up to 200 °C is observed in TGA. This value agrees with the theory for acetic acid monosolvate (16.12%).

Forms A and C were obtained using toluene as the solvent for the fast cooling and high initial concentration case. In this preliminary screening, for the performed triplicate, pure Form A was obtained in two experiments and pure Form C in one experiment. They were characterized by PXRD (Figure A.3) and the melting event at 109.92 °C in DSC (Figure A.4). This value corresponds to the melting onset of Form C[69]. Form A was obtained for the other conditions for crystallization in toluene. Figure A.3 also shows the PXRD pattern for high initial concentration and slow cooling rate (orange line). In DSC, the melting peak of Form C is followed by partial recrystallization of Form A and its melting peak at around 138.63 °C. The events are in good agreement with the melting points of both Forms A and C[69]. In Section 4.3.1 (B), crystallization in toluene is further investigated under other experimental conditions.

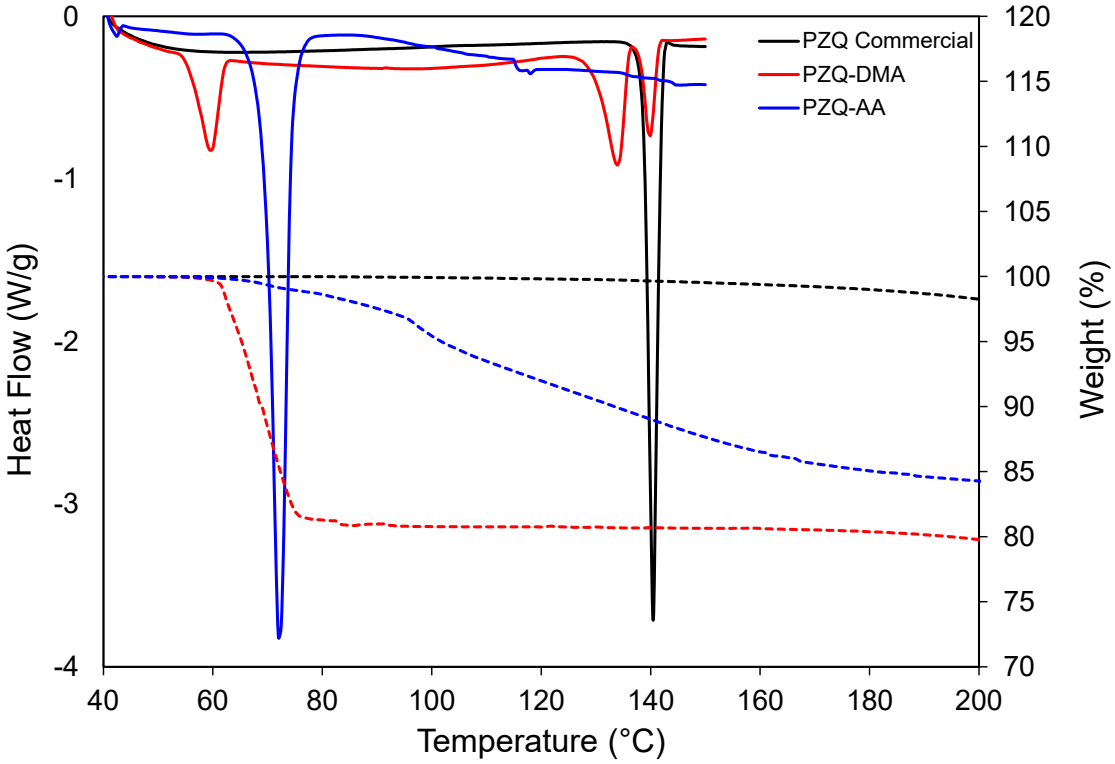

Figure 4.2 - DSC (solid lines) and TGA (dashed lines) thermograms of PZQ-DMA and PZQ-AA and comparison with PZQ Commercial (Form A).

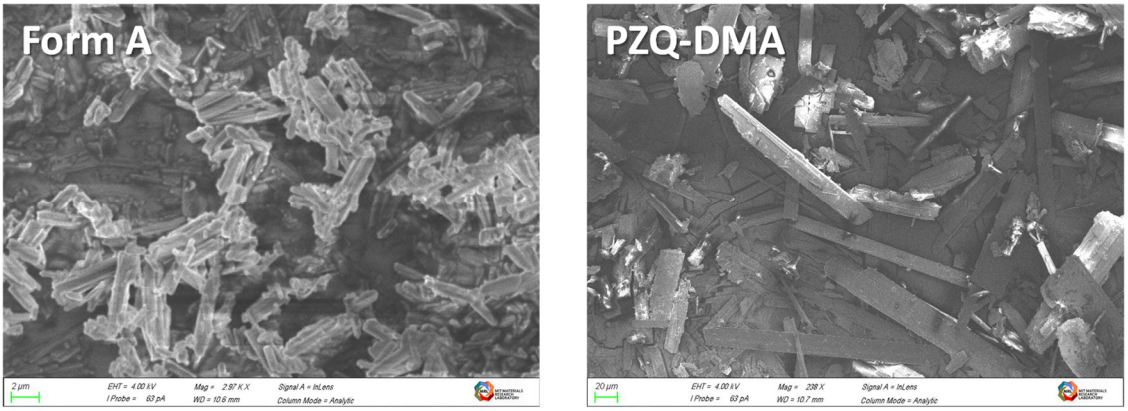

Figure 4.3 - SEM images of Form A (2970X, left) and PZQ-DMA (238X, right).

In the case of triethylamine, pure Form C was obtained for all analyzed conditions in an induction time much shorter than that observed for crystallization in toluene, also confirmed by comparing the PXRD patterns (Figure A.3) and melting point (red curve in Figure A.4). Section 4.3.1 (C) presents other results, such as Form B, obtained for crystallization from TEA under different conditions. Notably, Form C (indexed as GOYZOM) was only obtained so far by neat grinding in a vibrational mill[69].

A) DMA solvate transformation at ambient condition

The fresh DMA solvate was allowed to age at ambient conditions, and XRD analyses were performed periodically. After 12 days, the transformation of the DMA solvate was observed (Figure 4.4). Analyzing the PRXD pattern after 12 days, this phenomenon is more clearly observed by the decrease in the characteristic peaks of PZQ-DMA (e.g., 2ϑ value of 18.17°) and the appearance of other peaks. After 20 days, the transformation was complete. The TGA and DSC results show predominant desolvation and transformation into a new anhydrous form (named Form G), which will be better characterized in Section 4.2.

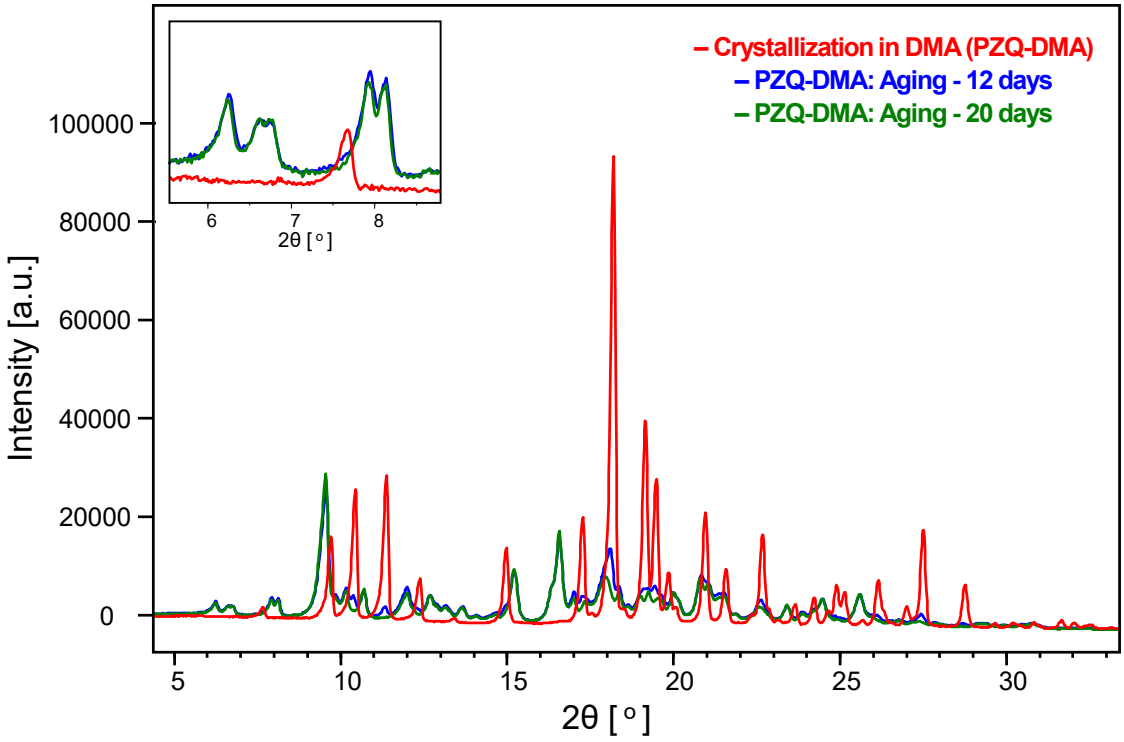

Figure 4.4 - Comparison of PXRD patterns of fresh PZQ-DMA (red line) and PZQ-DMA on aging at ambient conditions after 12 days (blue) and 20 days (green). Total conversion to a new Form (G) and Form A is obtained after 20 days. Form A is identified by its characteristic peaks in the enlarged 2ϑ° range in the frame.

Thus, the DMA desolvation under these conditions resulted in the majority transformation in Form G, but with concomitant transformation in a small percentage of Form A. It is evidenced by the enlarged pattern in the frame of Figure 4.4, in which characteristic peaks of Form A at 2ϑ values of 6.3, 6.7, 8.0, and 8.3º are observed. Form G has no such characteristic peaks (see Section 3.2). Even after total conversion into a mixture of forms G and A, the samples were analyzed for up to 50 days, obtaining the same PXRD pattern as that obtained after 20 days of aging. Therefore, Form G remained stable within this monitoring time.

SEM analysis revealed differences in habit and size due to PZQ-DMA transformation (Figure 4.5). The laths of PZQ-DMA differ from the product obtained after 20 days of aging. Form G exhibits smaller and agglomerated crystals. The presence of needle-like crystals under the surface of the agglomerates also notices the concomitant conversion to Form A.

B) The role of agitation in fast cooling crystallization using toluene

The results presented for crystallization in toluene showed the formation of Form C for only one of the three experiments performed at high initial concentration and fast cooling rate. In order to better explore crystallization in toluene, the effect of stirring the suspension was studied. Ten samples were taken adopting the same procedure described in Section 2.3. However, in five samples, no agitation was used. For the five samples with agitation, pure Form A crystals were obtained, characterized via PXRD and DSC. Without agitation, four samples corresponded to pure Form C and one to Form A. This result shows that agitation is a significant variable for the kinetics of crystallization. With agitation, the introduced secondary nucleation favors the formation of the more stable Form A. When agitation is not used, primary nucleation of the metastable Form C is predominant compared to primary nucleation of the metastable Form A. However, due to the stochasticity of the primary nucleation, Form C was not obtained in one experiment under these conditions. A set of hundreds of experiments should be conducted to better estimate the probability of the forms nucleation. Thus, it is already evident that the crystallization of PZQ in toluene at an initial concentration corresponding to saturation at 60 ^{o}C, the cooling rate of 5 ^{o}C/min, and no agitation is an effective method for obtaining the metastable Form C.

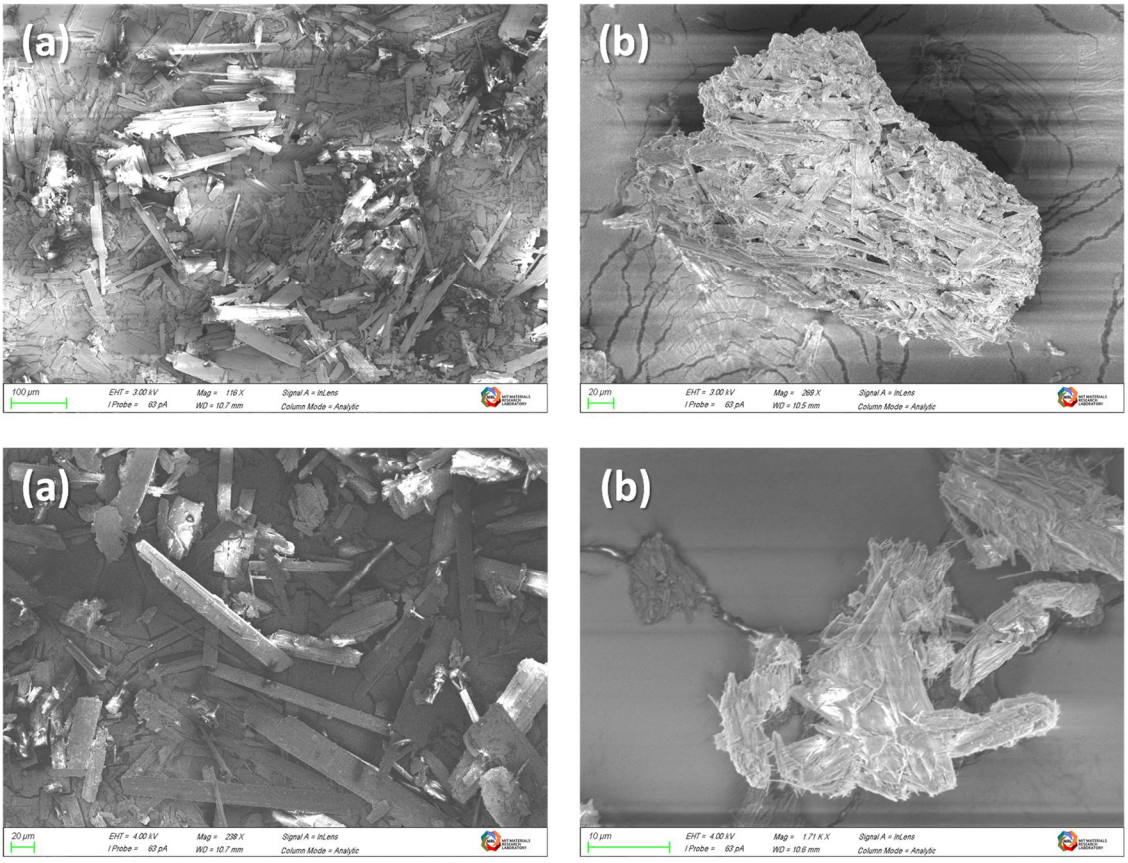

Figure 4. 5 - SEM images of: a) Fresh PZQ-DMA (118X, top; 238X, bottom); b) Mixture of forms G and A obtained by PZQ-DMA aging after 20 days (269X, top; 1710X, bottom).

C) The role of agitation and pre-filtration in crystallization using TEA

As TEA allowed the crystallization of Form C for all analyzed conditions, crystallization using this solvent was also studied for different experimental conditions to investigate the possibility of forming other polymorphs. Two factors were studied here: filtration of the prepared solution before cooling and agitation. Nine sets of experiments were carried out evaluating three conditions regarding the performance of agitation and filtration of the mother solution (Table 4.2). All the experiments were performed in the high initial concentration level (saturated at 60 ^{o}C) and fast cooling rate (5 ^{o}C/min). Condition 1 was the same one performed in the previous experiments using TEA (as described in Section 2.3)

for forming Form C. Again, Form C was obtained for the nine experiments under condition 1, confirmed by the PXRD pattern obtained (Figure 4.6).

Table 4.2 - Conditions evaluated for rapid cooling crystallization of PZQ in TEA

Condition	Agitation	Pre-filtration
1	Yes	Yes
2	No	No
3	No	Yes

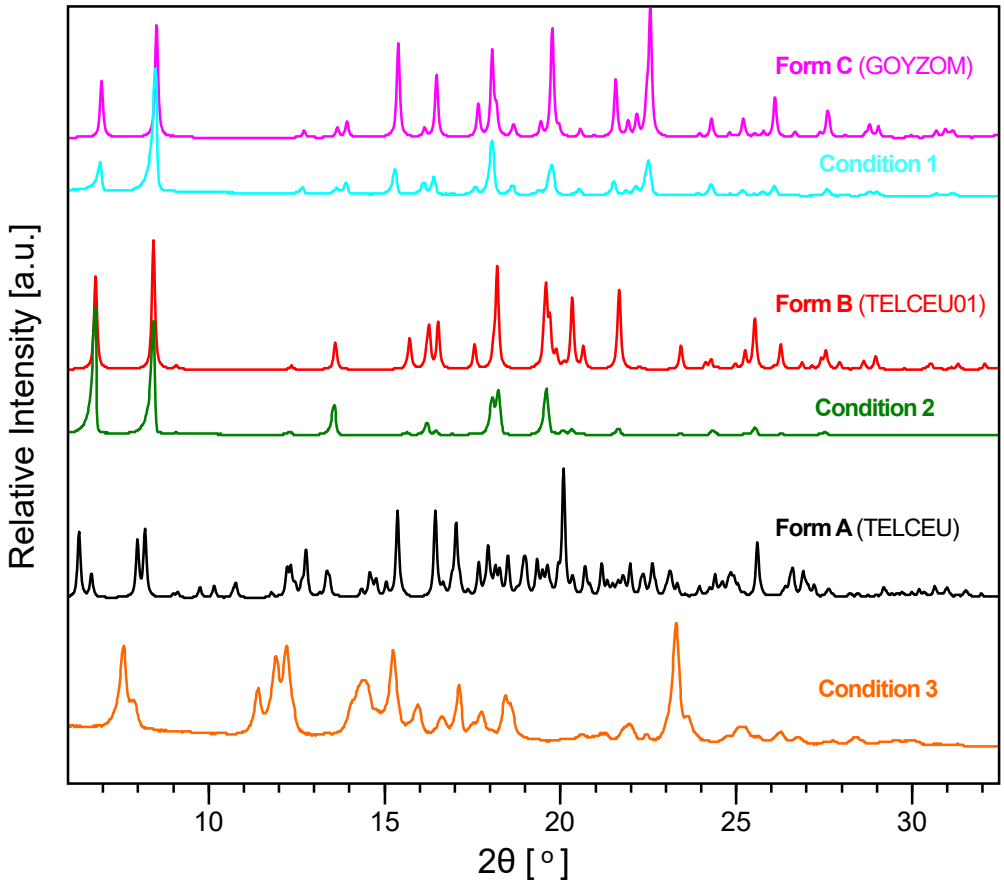

Figure 4. 6 - PXRD obtained at conditions 1 (blue), 2 (green) and 3 (orange) for crystallization of PZQ in TEA, and their comparison with forms A (black), B (red) ,and C (pink).

For condition 2, agitation was not used, and the solution was not filtered before cooling in Crystal16™. Pure Form B was obtained in the nine experiments under this condition (see the comparison of PXRD patterns in Figure 4.6). The absence of filtration can, therefore, favor the cross-nucleation of Form B. This result is important since Form B could only be obtained under these experimental conditions using TEA among all the solvents analyzed. The DSC curve for Condition 2 is shown in Figure A.4 (blue curve). The melting peak matches Form B's previously reported melting point without any event after it. Obtaining Form B has only been reported to be obtained by neat grinding of commercial PZQ[68].

Condition 3, in which agitation was not carried out, but filtration of the mother solution was carried out, introduces the obtainment of a new form of PZQ, Form H. TEA is shown to be a solvent that favors the formation of metastable forms, being an interesting case of study for the crystallization of PZQ. Figure 4. 6 (orange line) presents the PXRD pattern of Form H.

Thermal analysis of Form H (Figure 4.7) shows that it is an anhydrous form since there was no mass loss during TGA (dashed line) during the events observed in the DSC curve (full line). The DSC profile can be interpreted as follows: first, an endothermic event starting at 79.59 ^{o}C can indicate melting onset of Form H; after the melting event, expressive recrystallization of Form B followed by its melting at 112.27 ^{o}C is observed. This value corresponds to the melting onset of Form B[66]; directly from the melt, Form G partially crystallizes and melts at 132.31 ^{o}C. Also, a small amount of Form A crystallizes and melts at 137.72 ^{o}C. The shift in Form A melting point can be explained by the small crystallite size[70].

Form H proves to be the most unstable anhydrous form when compared to other well-characterized anhydrous forms (H $<<<$ B $<$ G $<$ A).

The SEM images in Figure 4.8 presents the morphology of the different forms obtained using TEA as the solvent compared to commercial Form A. For Condition 2, Form B appears clustered long and very thin whiskers, as observed by Zanolla et al[68]. Forms C and H exhibited differences in the habitus morphology

compared to Forms A and B. Form C appear as agglomerated tabular crystals and Form H as small platy crystals.

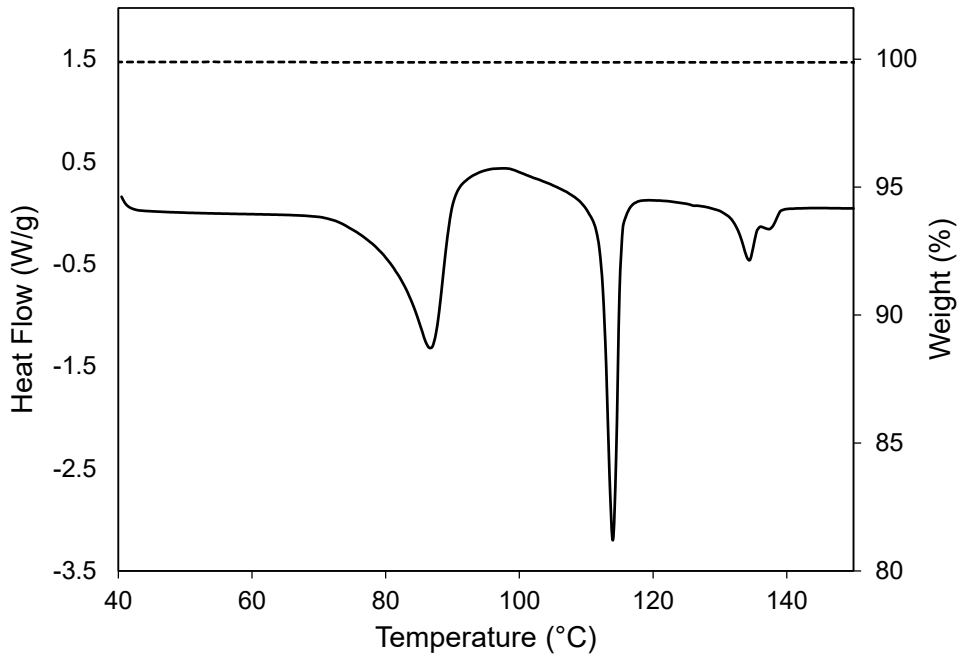

Figure 4.7 - DSC (solid line) and TGA (dashed line) thermograms of Form H obtained at condition 3 for crystallization of PZQ in TEA

4.3.2 Water vapor-induced desolvation/transformation

In Section 3.1.1, the transformation of the PZQ-DMA solvate in ambient conditions evidences the spontaneous desolvation and transformation of the crystalline structure, allowing obtaining a mixture of forms G and A. When submitted to water vapor-induced atmosphere overnight, total conversion to Form G was observed. The PXRD pattern for this condition does not show characteristic peaks for Form A (Figure 4.9). No pattern changes were observed during the 50 days that Form G was monitored via PXRD. In Figure 4.9, it is also possible to compare the result to the blank analysis, in which fresh PZQ-DMA was submitted to the same procedure using the same apparatus (Figure

A.1) but in the absence of water. Thus, water plays an essential role in expelling DMA and collapsing the crystalline structure.

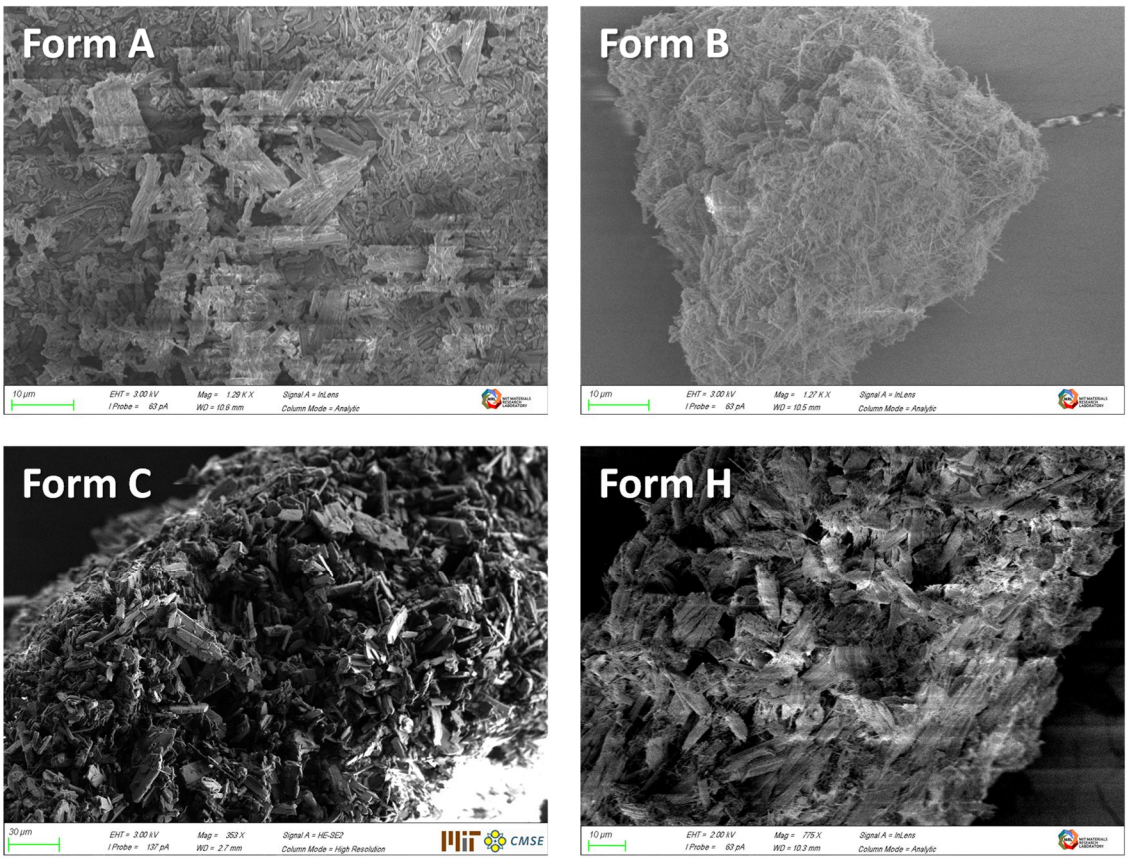

Figure 4.8 - SEM images of Form A (1290X, top left), Form B (1270X, top right), Form C (353X, bottom left), and Form H (775X, bottom right).

The difference in activities between DMA and water explains the facilitated desolvation for this experiment. Interestingly, through the thermal analysis (Figure 4.10), it is possible to observe that Form G does not represent a hydrate; water's role is only essential for the expulsion of DMA and transformation into a new anhydrous crystalline structure. The TGA curves (dashed lines) do not indicate any mass loss for the events observed by the DSC analysis. The DSC profile of Form G obtained by water vapor diffusion in PZQ-DMA only exhibits one single endothermic peak corresponding to its melting onset of 132.10 ^{o}C (25.46

kJ/mol). Compared to the mixture of forms G and A obtained by PZQ-DMA aging, a similar profile is obtained, differing by the melting peak of the small fraction of Form A that crystallized concomitantly. The exposure of PZQ-DMA to a water-vapor atmosphere is an effective method in which the nucleation kinetics of Form G is favored without partial conversion to Form A.

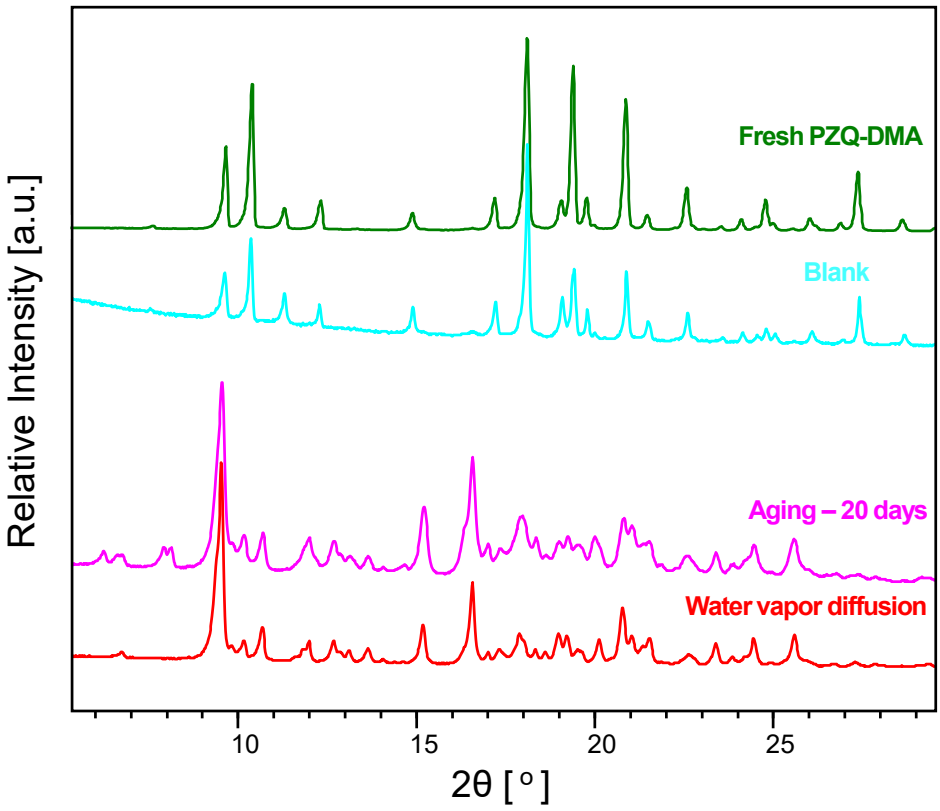

Figure 4.9 - PXRD patterns of fresh PZQ-DMA (green), blank for the presence of water (blue), mixture of Forms G and A after 20 days on aging at ambient condition (pink), and pure Form G obtained by water vapor diffusion experiment (red).

The relative stability of Form G can be assessed by analyzing its melting event (at 132.10 °C, ΔH_f = 25.46 kJ/mol) and those of previously reported forms (gray curves in Figure 4.10): Form A (at 138.90 °C, ΔH_f = 30.19 kJ/mol), Form B (at 113.19 °C, ΔH_f = 25.04 kJ/mol), and Form C (at 109.92 °C, ΔH_f = 27.74

kJ/mol. According to the heat-of-fusion rule of Burger and Ramberger, the polymorphic pairs B-C and G-C are suggested to be enantiotropically related[146,147]. According to the same rule, Form A is monotropically to the other forms because it has the highest melting point and heat of fusion[146,147].

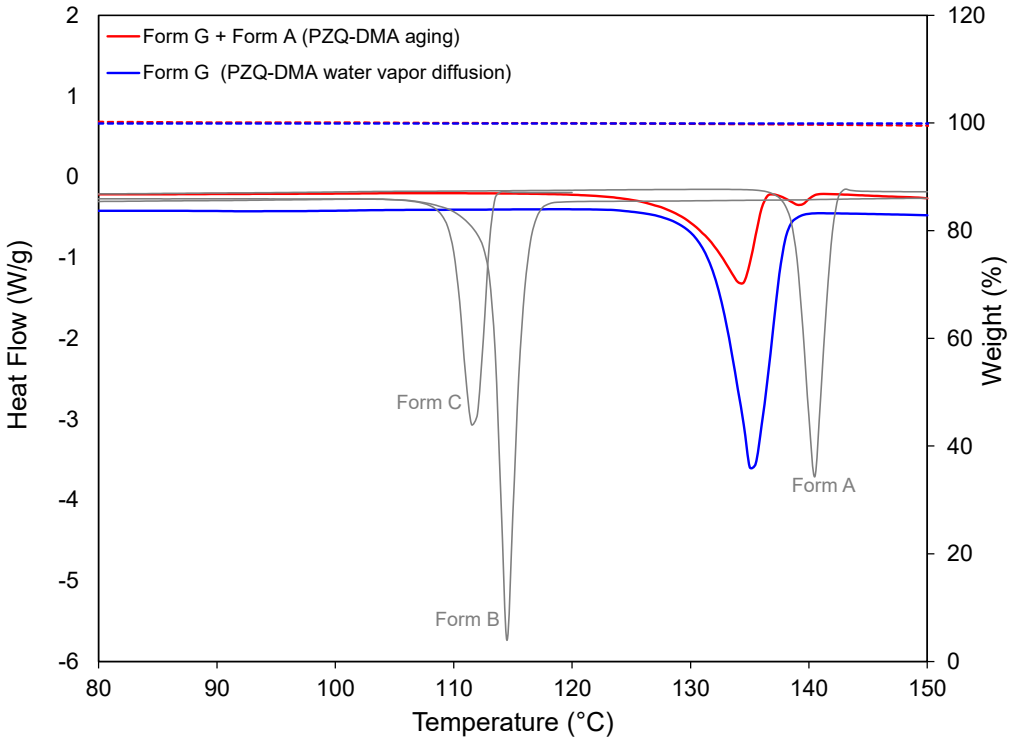

Figure 4.10 - DSC (solid lines) and TGA (dashed lines) thermograms of PZQ-DMA after transformation by aging (mixture of forms G and A, red) and by water-vapor diffusion (Form G, blue).

For the pair B-C, Zanolla et al. also observed a higher enthalpy of fusion value for Form C (lower melting point)[69]. However, the authors still attributed a monotropic relationship between Forms B and C due to the slight difference of about 6 kJ/mol obtained for the enthalpy of fusion, which was justified by inherent crystal defects, as they were obtained by mechanical treatment. In the present study, the difference in enthalpy of fusion between forms B and C was more pronounced (about 27 kJ/mol). Given the high crystallinity obtained for

Forms B and C via cooling crystallization, it is more likely that they are, therefore, enantiotropic polymorphs.

The pairs B-G and A-G are monotropic systems, with Form G always more stable than Form B and always less stable than Form A below the melting point (B < G < A).

For pairs B-C and G-C, the transition temperature (T_t) was estimated based on the method proposed by Yu[148] using the available melting data. The methodology used for the estimation of T_t can be found in SI. The estimated T_t for B-C and G-C are 83.45 °C and 17.03 °C, respectively. In both pairs, T_t lies below the melting point of the lower melting form, suggesting enantiotropic systems. It is worth mentioning that Yu's method indicates a good approximation if the transition temperature is not too removed from the lowest melting temperature of the two considered polymorphs. For the pair G-C, the uncertainty associated with using this method is more expressive due to the temperature difference between T_t and the melting point of Form C ($\Delta T \approx 92.9$ °C). For the pair B-C this temperature difference is relatively small ($\Delta T \approx 26.5$ °C).

At temperatures above T_t, the higher melting form is more stable, while at temperatures below T_t, the lower melting form is more stable. Therefore, it is possible to infer that Form C is more stable than Form B up to $T_t = 83.45$ °C, and more stable than form G up to $T_t = 17.03$ °C, inverting the stability after the respective T_t[148].

The estimated transition temperature for the G-C pair is low, thus suggesting that the Form G is the most stable of the pair in a wide temperature range. For example, for temperatures between 17 °C and 83 °C (thus including room temperature), the suggested order of stability is: B < C < G < A.

The transformation of fresh PZQ-DMA solvate into Form G is well illustrated when analyzing the SEM images. Figure 4.11 shows that regular crystals of the same average size were obtained for Form G, exhibiting smaller

crystals and a rod-like shape (Figure 4.11b) that differ from the laths of PZQ-DMA (Figure 4.11a).

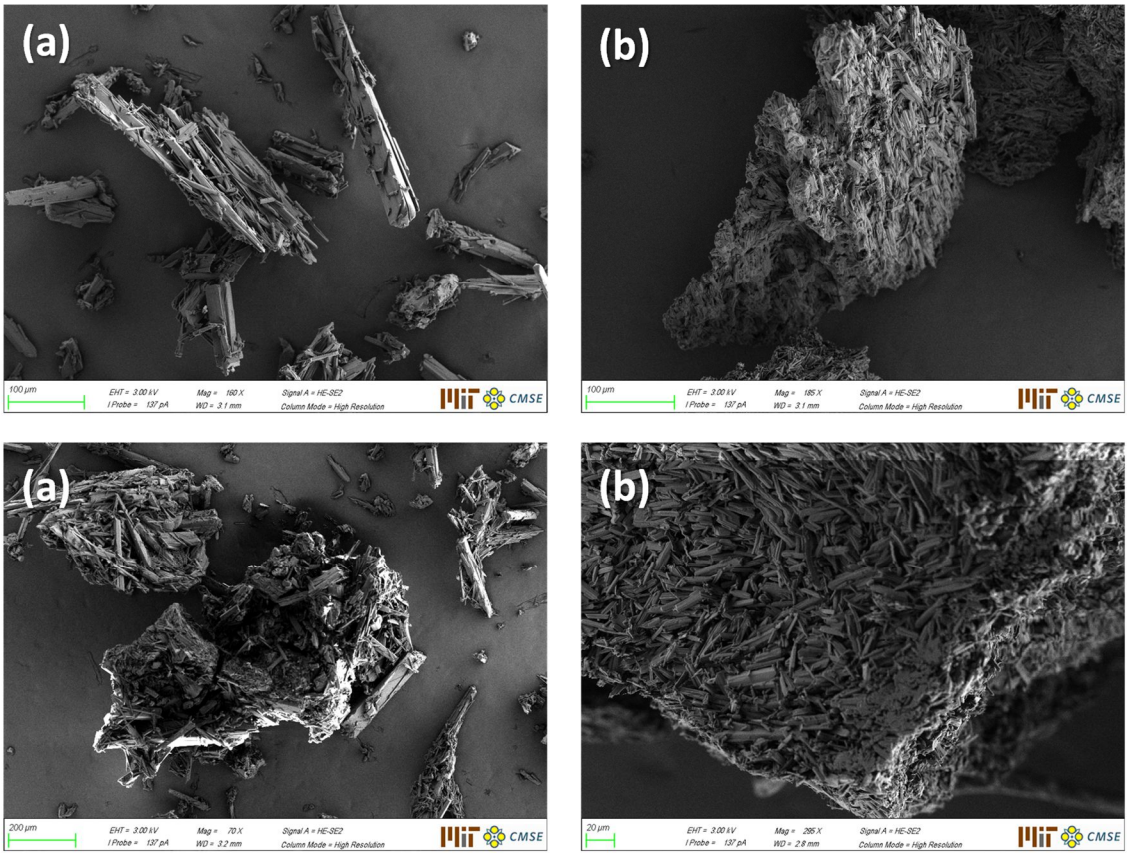

Figure 4.11 - SEM images of: a) Fresh PZQ-DMA (160X, top; 70X, bottom); b) Form G obtained after water-vapor diffusion through PZQ-DMA (185X, top; 295X, bottom).

PZQ-AA was also subjected to a water-vapor atmosphere, and complete conversion to PZQ-HH is confirmed by comparing the PXRD pattern with the simulated WUHQAU[70] (Figure A.5). In this case, the desolvation of AA and the solvation of water occurred. The DSC and TGA curves also confirmed the total conversion to PZQ-HH. The weight loss in TGA was 2.69%, in good agreement with the theoretical value of 2.72% for a PZQ hemihydrate. The events in the DSC profile (red curves in Figure A.6) are as follows: firstly, the endothermic event of desolvation, followed by partial recrystallization and melting of Form G,

and later partial recrystallization and melting of Form A. PZQ-HH was first obtained by water-assisted grinding[70].

4.3.3 Polymorphic outcome from alcohol/water mixtures

The PXRD patterns in Figure 4.12 present the results summarized in Table 4.3 for the different water fractions in methanol/water and ethanol/water mixtures as solvent. For methanol mixtures, percentages of 30 and 40% v/v of water enable the formation of the second hemihydrate (named PZQ-HH2). As for ethanol/water mixtures, percentages of 40 and 50% allow the formation of PZQ-HH2.

Table 4.3 - Results obtained from PZQ cooling crystallization experiments in alcohol/water mixtures

Solvent	Water fraction (% v/v)				
	10	20	30	40	50
Methanol	A	A + HH2	HH2	HH2	Amorphous
Ethanol	A	A	A	HH2	HH2

This hydrated form was first reported by MacEachern et al., but the stoichiometry was not completely elucidated[86]. By thermal analysis (Figure A.6), the weight loss in TGA of 2.64%, which corresponds to the water loss, is very close to the theoretical value for hemihydrate (2.72%). It is also indicated by the first desolvation endotherm with onset at 81.89 °C (peak at 91.89 °C) in the DSC profile. The following events succeed in the desolvation of PZQ-HH2: recrystallization followed by melting of Form C, B, and A, consecutively. The DSC thermogram is in a good agreement with the one presented by MacEachern et al.[86].

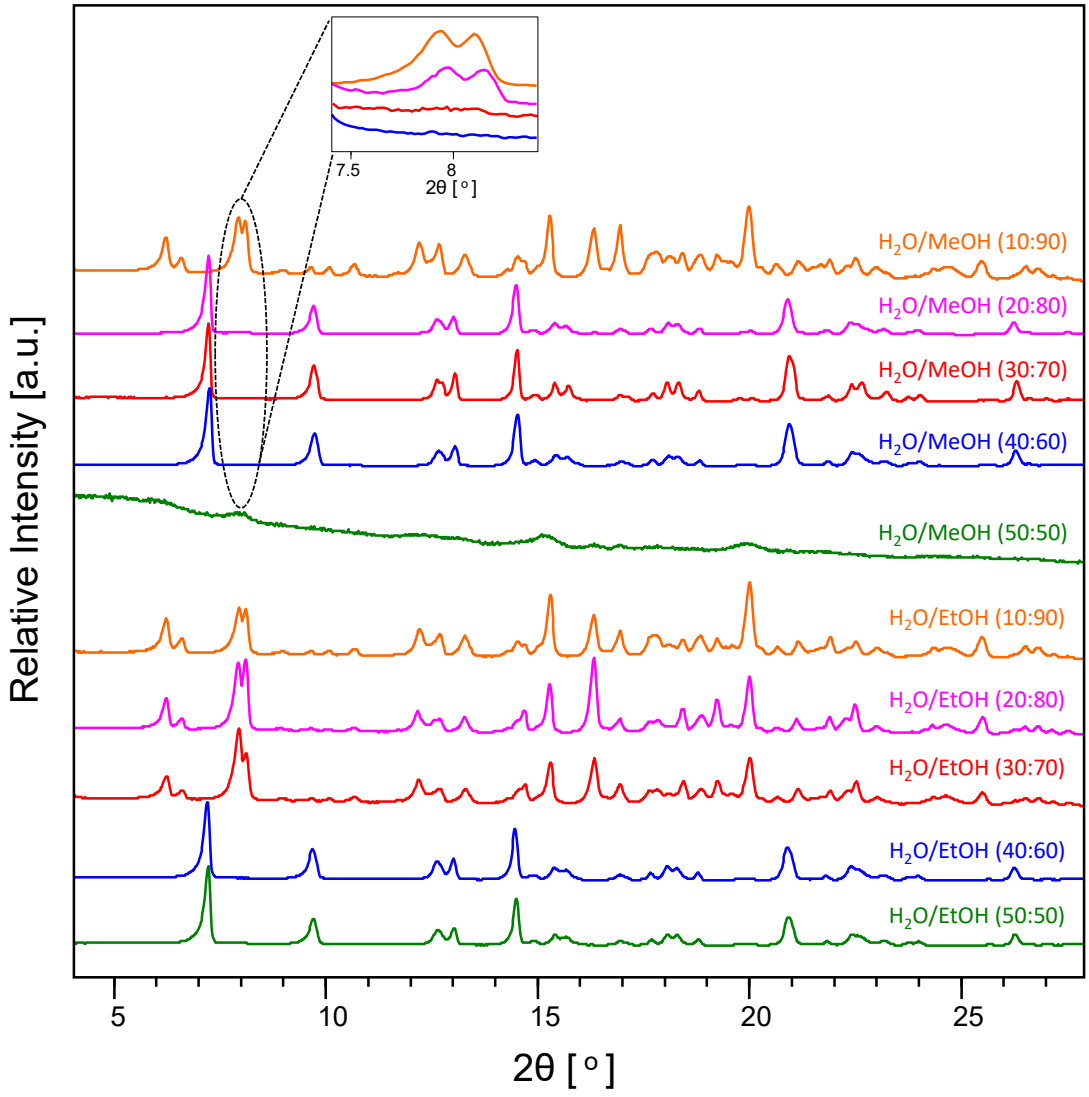

Figure 4.12 - PXRD patterns of PZQ obtained in water/methanol (H_2O/MeOH) mixtures (top patterns) and water/ethanol (H_2O/EtOH) mixtures. The presence of Form A in H_2O/MeOH (20:80) is identified by its characteristic peaks in the enlarged 2ϑ° range in the frame.

Furthermore, the KF titration result showed water content of 2.67 ± 0.04%, confirming PZQ-HH2 as a hemihydrate. Three PZQ-HH2 samples were used for the KF titrations, with triplicate injections for each sample. The KF Hydranal Standard water content was 10007.5 ppm, valid within the reference range (1007±3 ppm). SEM images of the produced PZQ-HH2 indicate the formation of clusters of tiny tabular crystals (Figure 4.13).

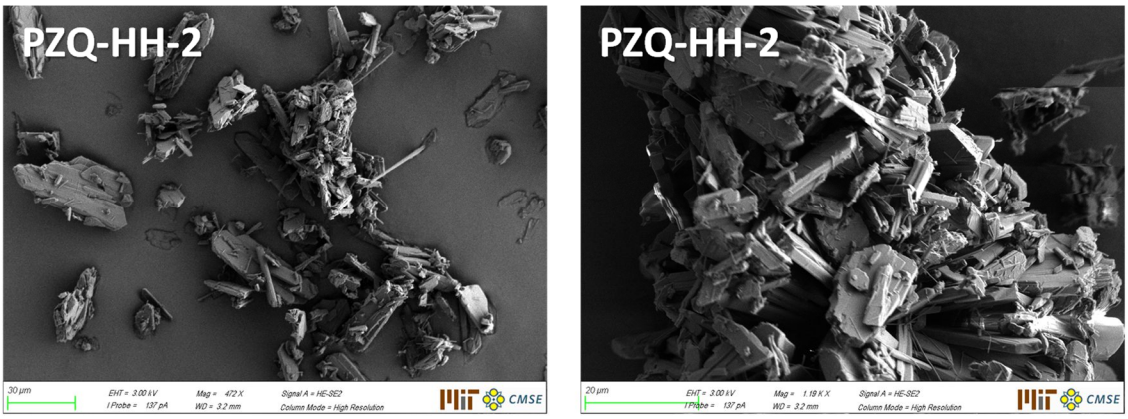

Figure 4.13. SEM images of PZQ-HH-2 (472X, left; 1190X, right).

4.4 Conclusions

The polymorphism of PZQ was investigated using cooling crystallization experiments in different solvents for different cooling rates and concentration levels. A new DMA solvate (PZQ-DMA) was identified and characterized. The DMA desolvation phenomena were studied; exposure to a water-vapor atmosphere being an excellent method to prepare a novel anhydrous polymorph by desolvation of PZQ-DMA, named Form G. Water plays an important role in expelling the DMA molecules from the original PZQ-DMA. Obtaining isolated Form G without any residual form of Form A was confirmed.

Among the studied solvents, triethylamine is shown to be a suitable solvent for the investigation of polymorphic nucleation of PZQ, showing dependence on the use of pre-filtration and agitation of the medium for the cooling crystallization experiments. A second anhydrous form was prepared by crystallization using TEA with no agitation, named Form H. The new Forms G and H were characterized by PXRD and DSC/TGA. Form G has a higher melting point than forms B, C, and H. Within the 50 days during which PXRD and DSC analyses of Form G

were periodically performed, no changes or transformations were observed. On the other hand, Form H appears to be the less stable form.

By changing the type of solvent and the experimental conditions for crystallization, the reported Forms B and C, the two hydrated forms, and the acetic acid solvate were prepared. The recently reported hydrated form was identified as another hemihydrate (PZQ-HH2) by thermal analysis and KF determination, being produced more efficiently by cooling crystallization in methanol and ethanol aqueous mixtures. Mixtures with a low percentage of water do not allow obtaining PZQ-HH2, whereas solutions with 30-40% of water in methanol and 40-50% of water in ethanol are suitable for the preparation of this hemihydrate.

This work also demonstrated that classic cooling crystallization is a more effective method to screen polymorphs and identify new solid forms than those obtained from more complexes and less reproducible techniques, such as mechanochemical grinding.

Chapter 5

Solubility Determination and Crystallization of Praziquantel

This chapter presents the experimental work carried out for praziquantel (PZQ). First, using a medium-throughput screening device (Crystal16™), PZQ solubility in different organic solvents was determined. This preliminary study is essential for choosing the solvent used in the crystallization process. Next, an experimental investigation is presented based on the results obtained for different batches, using in situ image analysis (Blaze900 BlazeMetricsTM) to evaluate the process over time.

5.1 Solubility estimation of praziquantel

The Crystal16™ device was used to obtain praziquantel solubility measurements. Solvents were methanol, ethanol, 1-propanol, 1-butanol, acetone, DMA, toluene, acetonitrile, dioxane, and THF.

Different microvials of 1.5 mL (11.5 mm diameter, flat-bottomed) containing different amounts of PZQ and solvent were used. Vials containing excess solids were initially used in all determinations in order to start at a cloud point (0% of laser transmission).

The mass of praziquantel and solvent added to each vial was determined by weighing in Mettler Toledo's AX205DR DeltaRange analytical balance with a readability of 0.01 mg. The suspensions were at least 5°C below the desired starting temperature. The vials were also properly sealed using parafilm around the caps to avoid any possible solvent loss by evaporation.

The vials were placed in the Crystal16 and maintained at the same temperature for 15 minutes, ensuring the experiment started from the cloud point. After this time, the temperature was increased by 5 degrees, defining the starting temperature of each experiment, and the slurry was stirred for another 30 minutes. After this equilibration time, the temperature programming method was started.

The principle of determining solubility takes place by heating at a slow temperature ramp until a clear point is reached, defined as the first point at which all crystals disappear, obtaining an increase in light transmission through each vial up to 100% of laser transmission.

During the heating stages, the suspension was slowly heated at a rate of 0.1 °C/min to ensure it was approximately in equilibrium. Figure 5.1 presents a typical method. Triplicate measurements were used in each run, which was possible by performing heating-cooling cycles. In the cooling stages, a faster ramp was used (-3 °C/min) to facilitate the nucleation and consequent recrystallization, reaching a new cloud point to be subjected again to a heating stage for a new measurement of the solubility temperature.

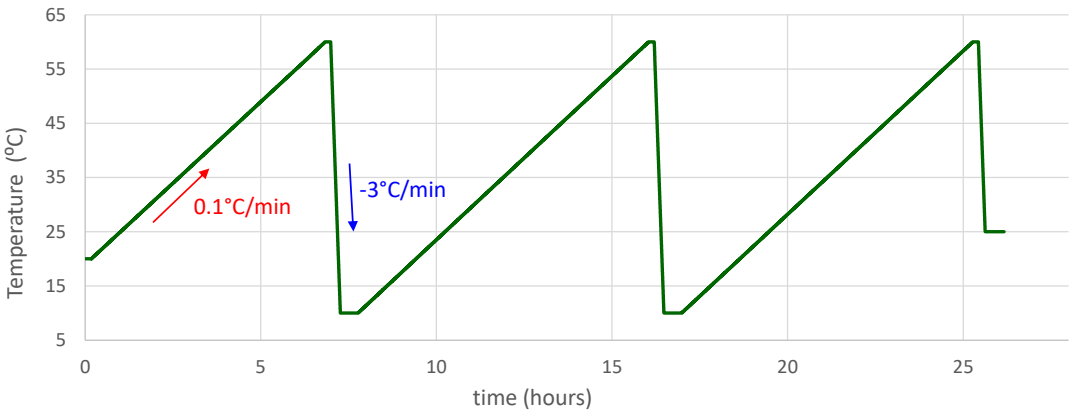

Figure 5.1 - Temperature programming method in Crystal16. The red arrow indicates a heating step and the respective heating rate ($0.1\,°C/min$) and the blue arrow indicates a cooling step and the respective cooling rate ($-3\,°C/min$).

Figure 5.2 presents an example of the experimental result for the solubility of PZQ in methanol. Compared to the first reading, excellent agreement is obtained for the following determinations after the cooling stages.

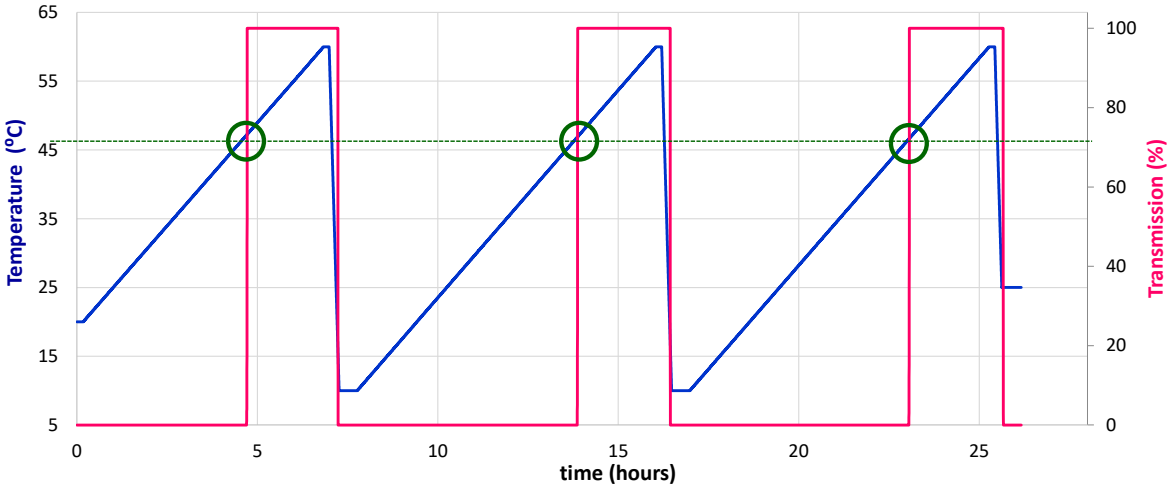

Figure 5.2 - Solubility measurement result for PZQ in methanol using Crystal16. The pink lines represents the experimental transmission and the blue lines the performed temperatures. The red circles indicates the change in transmission to 100% (clear point).

The triplicate determination can only be effectively applied to stable polymorphs that do not crystallize in another form after the following nucleation events. The polymorphism screening studied in Chapter 4 ensures that the commercial PZQ (Form A) was obtained in the determinations using all solvents studied except for DMA. For DMA, the following recrystallization events led to another form (PZQ-DMA), confirmed by PXRD. Therefore, only one determination per sample is possible using DMA.

In order to obtain a thermodynamic model for each studied system, the following methodology, inspired by the procedure described in Nicoud et al., was used[149]:

1. Measure the solubility at some points from Crystal16 runs.
2. Measure the solid-state properties from DSC analysis.
3. Calculate the experimental activity coefficients using the modified Van't Hoff equation (Eq. 5.1) and the determinations in 1 and 2.

$$\gamma_p = \frac{1}{x_p}\exp\left(\frac{\Delta H_f}{R}\left(\frac{1}{T_f}-\frac{1}{T}\right)\right) \tag{5.1}$$

where x_p and γ_p denote the PZQ molar fraction and activity coefficient, respectively; ΔH_f is the molar enthalpy of fusion.

4. Fit the interaction coefficients of the thermodynamic model. In this work, the Wilson method was employed to describe the variations of the activity coefficient with temperature and molar composition:

$$\ln(\gamma_p) = -\ln(1 - A_{sp}\,x_s) - x_s\left[\left(\frac{x_p A_{sp}}{1 - A_{sp}\,x_s}\right) - \left(\frac{x_s A_{ps}}{1 - A_{ps}\,x_p}\right)\right] \tag{5.2}$$

where the index p denotes the PZQ (solute) and s the solvent. The solvent mole fraction is given by $x_s = 1 - x_p$, and A_{sp} and A_{ps} are the binary interactions parameters expressed by

$$A_{sp} = 1 - \frac{V_s}{V_p} exp\left(-\frac{\Delta g_{sp}}{RT}\right) \tag{5.3}$$

$$A_{ps} = 1 - \frac{V_p}{V_s} exp\left(-\frac{\Delta g_{ps}}{RT}\right) \tag{5.4}$$

where Δg_{sp} and Δg_{ps} $[J/mol]$ are the binary interaction coefficients to be estimated. The parameter estimation was performed using a Generalized Reduced Gradient algorithm, minimizing the objective function:

$$\Omega(\Delta g_{sp}, \Delta g_{ps}) = \sum_{i=1}^{N_{exp}} \left(\gamma_{p,i}^{exp} - \gamma_{p,i}^{calc}\right)^2 \tag{5.5}$$

where $\gamma_{p,i}^{exp}$ is the activity coefficient determined in step 2 (Eq. 5.1, and $\gamma_{p,i}^{calc}$ by Eq. 5.2).

5. Calculate the solubility x_p by Eq. 5.1. The equation is implicit in x_p.

The estimated parameters are shown in Table 5.1. Figure 5.3 present the experimental activity coefficients and the fit adopted. Figures 5.4 and 5.5 show the experimental solubility compared to the calculated values by the model. The solubility is expressed in molar fraction (x_p) and in [g of PZQ / g of solvent].

Table 5.1 – Estimated binary interaction coefficients

PZQ /	$\Delta g_{sp}\ (J/mol)$	$\Delta g_{ps}\ (J/mol)$
methanol	1797.87	2191.43
ethanol	1008.89	2103.84
1-propanol	2374.67	846.52
1-butanol	2591.69	416.67
acetone	-3775.34	10301.30
DMA	-5028.93	5194.01
toluene	-3686.89	47777.61
acetonitrile	-397.49	3181.35
dioxane	-5845.65	11525.37
THF	-6057.13	11394.73

From the described methodology, using the Van't Hoff equation with Wilson's model for the activity coefficient, a good fit to the experimental data is obtained. Appendix B reports the comparison of the values obtained with other literature data[150-152]. Solubility in THF and dioxane had not been studied previously. Good agreement exists with the data obtained in previous studies for the compared cases, except for crystallization in toluene. Toluene can lead to the crystallization of Form C. In this study, however, Form A was ensured to be obtained after recrystallization for the remaining determinations in toluene. Therefore, this highlights the importance of checking the polymorph when determining solubility.

Furthermore, the methodology proposed here using a medium-throughput system provides faster results. It uses less material to determine solubility than traditional methods, such as the isothermal saturation method used by Li et al.[151] and Liu et al.[152].

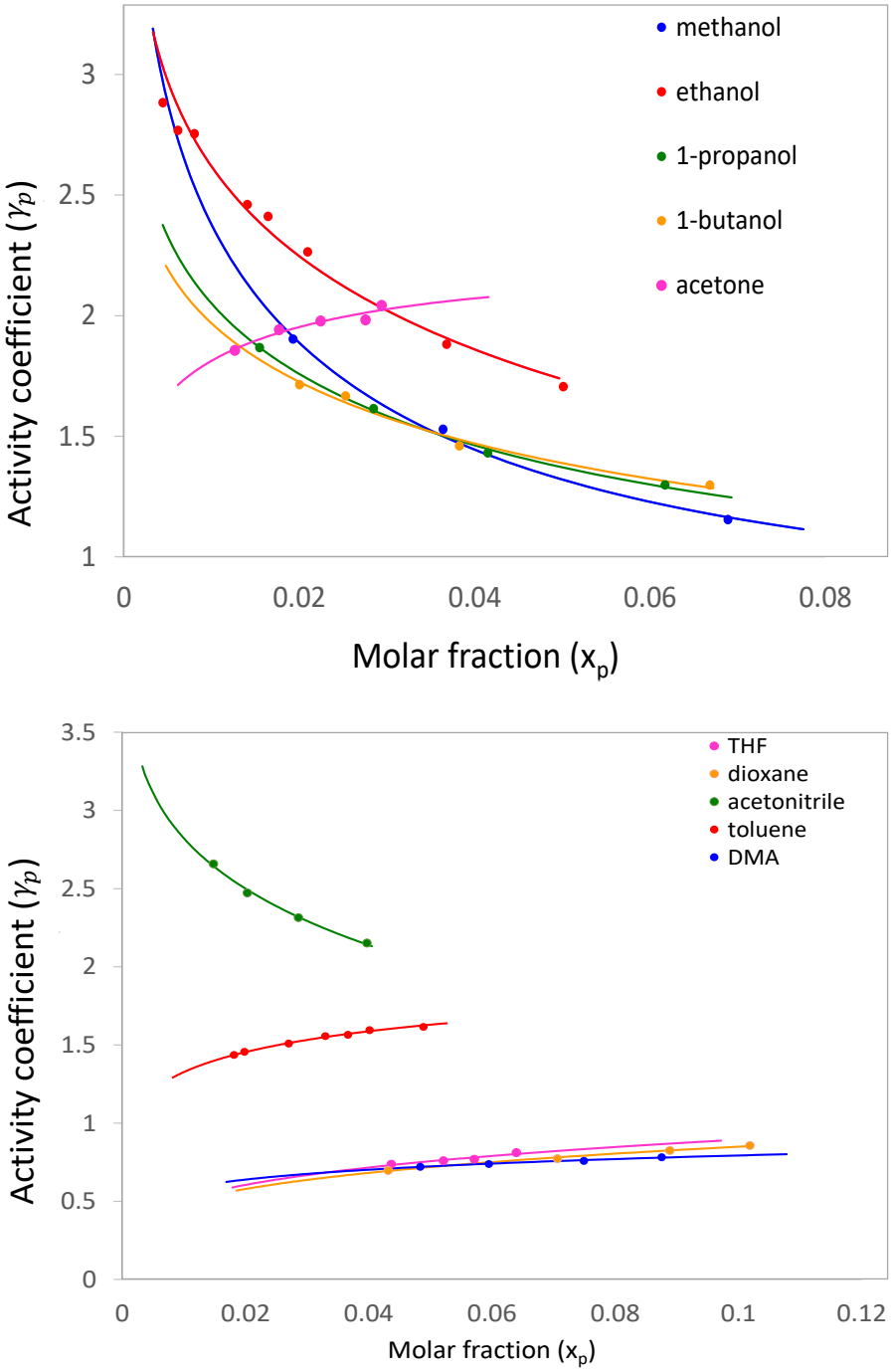

Figure 5.3 – Experimental (dots) vs. calculated activity coefficients (solid lines) of PZQ in different solvents.

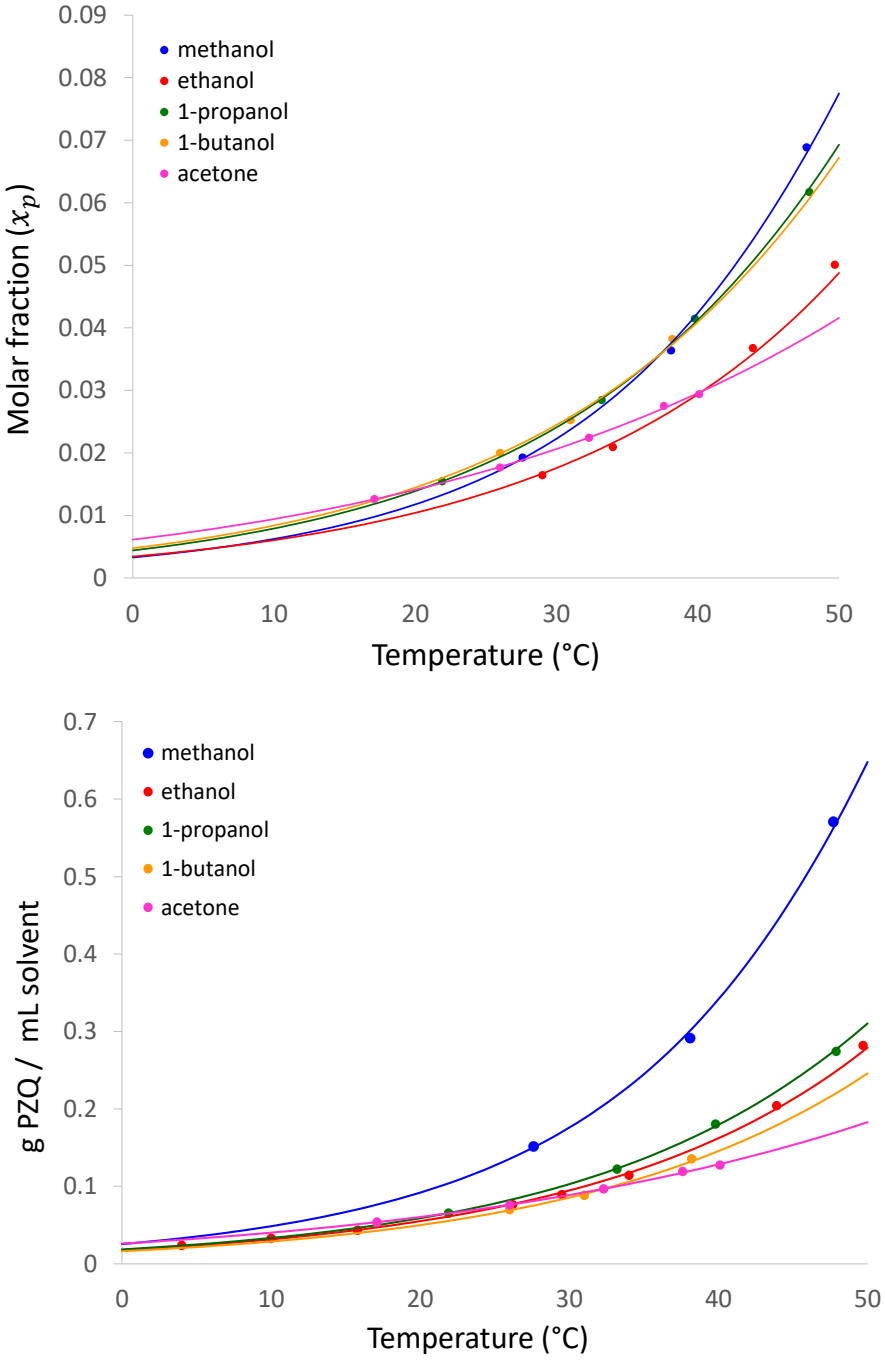

Figure 5. 4 – Solubility data (dots) vs. calculated curves (solid lines) of PZQ in methanol (blue), ethanol (red), 1-propanol (green), 1-propanol (yellow), and acetone (pink).

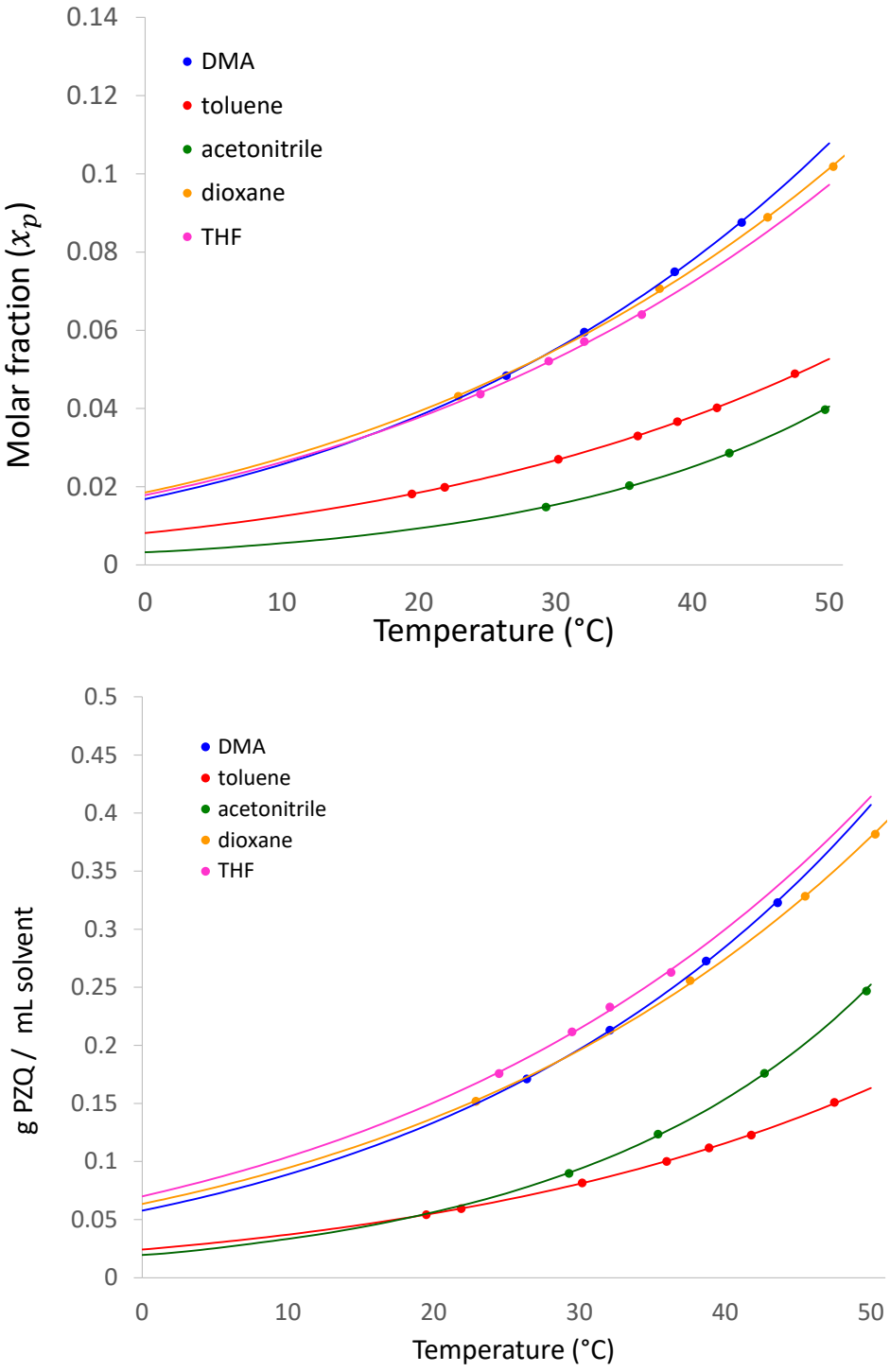

Figure 5. 5 - Solubility data (dots) vs. calculated curves (solid lines) of PZQ in DMA (blue), toluene (red), acetonitrile (green), dioxane (yellow), and THF (pink).

From the determined solubility curves, ethanol and methanol are the best candidates for cooling crystallization. We reached this conclusion by evaluating the conditions for a theoretical yield of 90%. Both solvents provided the lowest energy consumption (lower required ΔT, 36 °C for methanol and 38 °C for ethanol). Although the results suggest that methanol should perform best, the difference is minimal. Also, due to the high toxicity of this solvent, ethanol was the solvent chosen for carrying out the crystallization experiments presented in Section 5.2.

5.2 Experimental investigation of unseeded batch cooling crystallization of praziquantel

PZQ crystallization was performed in Mettler Toledo's EasyMax 102 reactor using a 100 mL two-piece glass reactor equipped with a PTFE cover and an overhead pitch-blade impeller. The agitation rate was 400 rpm in all experiments. The liquid phase was monitored using online attenuated total reflection Fourier transform infrared (ATR-FTIR) spectroscopy using Mettler Toledo's ReactIR 15 equipped with a 6.3 mm AgX DiComp probe.

The crystalline phase was monitored by online microscopy using a Blaze900 probe (BlazeMetrics™). The probe detects crystals above approximately 2 μm. Images were taken throughout the experiment. The saving of images can be independently chosen from its measurement duration, and we used a rate of 2 images per minute.

Blaze900 determined chord length distribution (CLD) data from the images obtained. The number of chords measured proportional to their probability of measurement, as well as scanning technologies like FBRM®. Compared to FBRM®, Blaze900's image-based measurements are inherently weighted by the chord length. It can be evidenced when analyzing a spherical particle. Chords close to the diameter will be more likely to be measured because there is more

available area and, thus, a greater probability of the chord measurement. In contrast, smallest chords, corresponding to the edges of the sphere are less likely to be measured because less corresponding area in the images is available for measurement (less probability of measurement). Therefore, the chord length naturally weights the acquired data.

Thus, to use measurements compatible with those acquired by FBRM®, in this work, the cube-weighted mean length and cube-weighted chord counts will be used as measurements in this work. Such measurements would be compatible with the square-weighted mean chord length (SWMCL) and square-weighted chord counts (SWCC) of FBRM®, respectively. The SWCC was chosen in this work to represent the number of crystals[137]. In seeking to adopt the same nomenclature, in this work, SWMCL and SWCC are used, but considering Blaze900 technique, the selection was made "cube weighted," as previously explained.

The chord lengths were determined by the length of a line that cross the particle between any two edge points. All the chord length measurements were within a size range of 2 – 700 μm, sorted into 80 size ranges (number of bins). The SWCC was calculated by

$$SWCC = \frac{\sum_{i=1}^{K} n_i \, {\lambda_i}^2}{1/K \, \sum_{i=1}^{K} {\lambda_i}^2} \tag{5.6}$$

where n_i is the number of chords in an individual bin (chord counts), λ_i is the midpoint of an individual bin $[\mu m]$, and K is the number of bins.

The SWMCL was determined by

$$SWMCL = \frac{\sum_{i=1}^{K} n_i \, {\lambda_i}^3}{\sum_{i=1}^{K} n_i \, {\lambda_i}^2} \tag{5.7}$$

In order to obtain further elucidation about the cooling crystallization of praziquantel in ethanol, we first evaluated the system by performing experiments in which complete information could be obtained. Allied with this is the concern with not using experimental steps that would consume much raw material, given its low availability. Thus, Figure 5.6 presents the design adopted for the performing experiments.

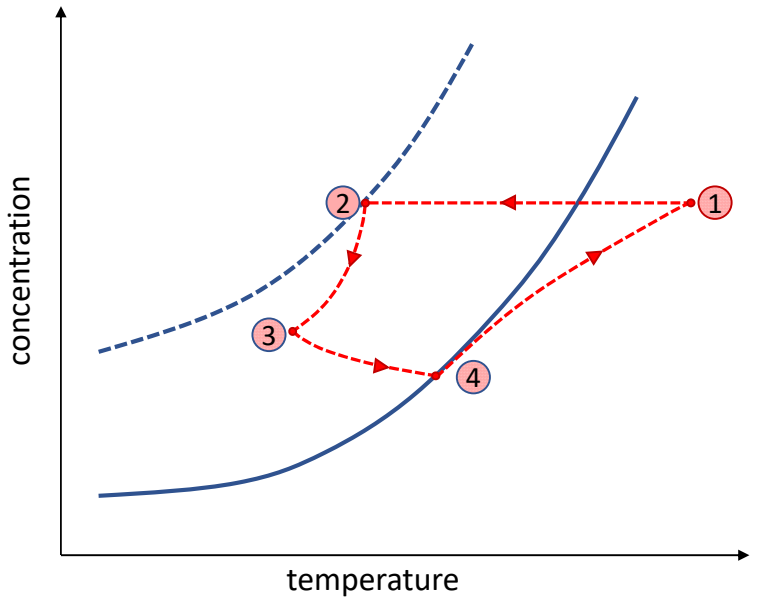

Figure 5.6 – Experimental strategy for the praziquantel cooling crystallization: 1 → 2: nucleation by reaching the metastable limit; 2 → 3: cooling crystallization; 3 → 4: decrease in supersaturation by heating; 4→ 1: dissolution (undersaturated condition). Dotted curve: metastable zone limit. Solid curve: solubility.

For all experiments, the initial cooling step from clear solution took place with the same slow cooling ramp to allow determination of the metastable zone width (MSZW). Therefore, the experiments were unseeded, in which cooling crystallization (path 2→ 3) occurred after reaching the limit (2) of the metastable zone (dotted curve in Figure 5.6). Subsequently, we carried out a heating stag to decrease the supersaturation, but stay in the metastable zone (path 3 → 4). Then, the heating led to the solubility curve (solid curve in Figure 5.6) crossing using a

moderate heating ramp performed, reaching an undersaturation condition (path $4 \rightarrow 1$) until complete dissolution.

Table 5.2 presents the experimental conditions for the analyzed experiments. The mass of solvent used in all experiments was 60 g of ethanol.

Table 5.2 – Experimental conditions for the praziquantel crystallization

Experiment	T_i (°C)	C_i (g PZQ / g ethanol)	$CR1$ (°C/min)	$CR2$ (°C/min)	HR (°C/min)
Exp1	20	0.050	0.2	0	0.5
Exp2	27	0.075	0.2	0.1	0.2
Exp3	33	0.100	0.2	0.2	0.4
Exp4	37	0.150	0.2	0.2	0.5

In addition, the same initial solution was subjected to a calibration step for concentration measurements in all experiments. This step is important since the absorbance data also depends on the temperature. For better accuracy of the calibration model, isotherms were determined for the original solution. Figure 5.7 presents a calibration scheme performed before the crystallization run in Exp1. After this step, the clear solution was set at the initial temperature (point 1 in Figure 5.6) to start the crystallization batch.

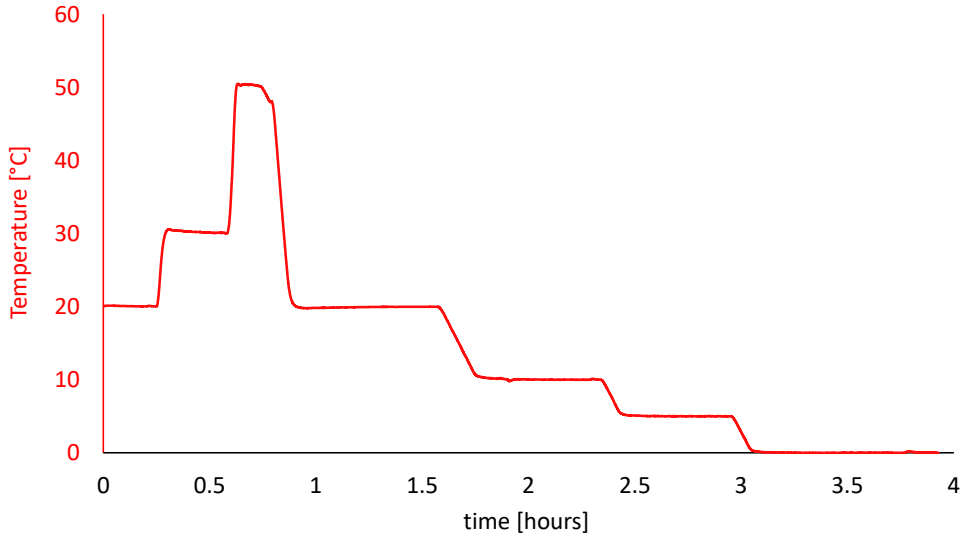

Figure 5. 7 – Temperature profile for the calibration of concentration for Exp1

Figure 5.8 summarizes the results obtained for Exp1. In point A, the beginning of crystallization is indicated by observing the first crystals to appear in the images. Although it is impossible to determine the nuclei size because only particles larger than 2 µm can be detected, this point will be adopted as an approximation to the metastable limit in this study. The evaluation of this point would be better established using the non-weighted chord counts (NWCC) to not diminish the contribution of the tiny crystals in the chord counts. However, similar trends were observed for NWCC and SWCC. The evolution of crystallization is perceived by the increase in chord length and counts, as illustrated in the images of points B and C. The solute concentration is lower in Exp1 than in the other experiments, implying a lower driving force (i.e., supersaturation). It justifies the formation of particles of smaller average size, which is also reflected by the lower SWMCL values. It justifies the formation of particles of smaller average size, which is also reflected by the lower SWMCL values. Although we know that the mean chord length did not perfectly represent the crystal size, for the experiments carried out here, its trend can be considered a good approximation to the crystal size's trend.

Figure 5.8 shows the existence of agglomeration of the smaller crystals. In D, the appearance of spherically agglomerated crystals is perceived, being the presence of spheres mostly seen in point E. When analyzing the experimental data, this is well explained by the increase in mean chord length and decrease in chord counts, which characterize agglomeration in larger particles, i.e., spherical agglomerates. At point F, when the heating step was already active, there were an increase in SWCC and a decrease in SWMCL due to the deagglomeration of the agglomerates into individual crystals. As heating progresses, dissolution is observed by crystals' shrinkage (point G) until total disappearance (point H), thus returning to the same solution present at the initial batch time.

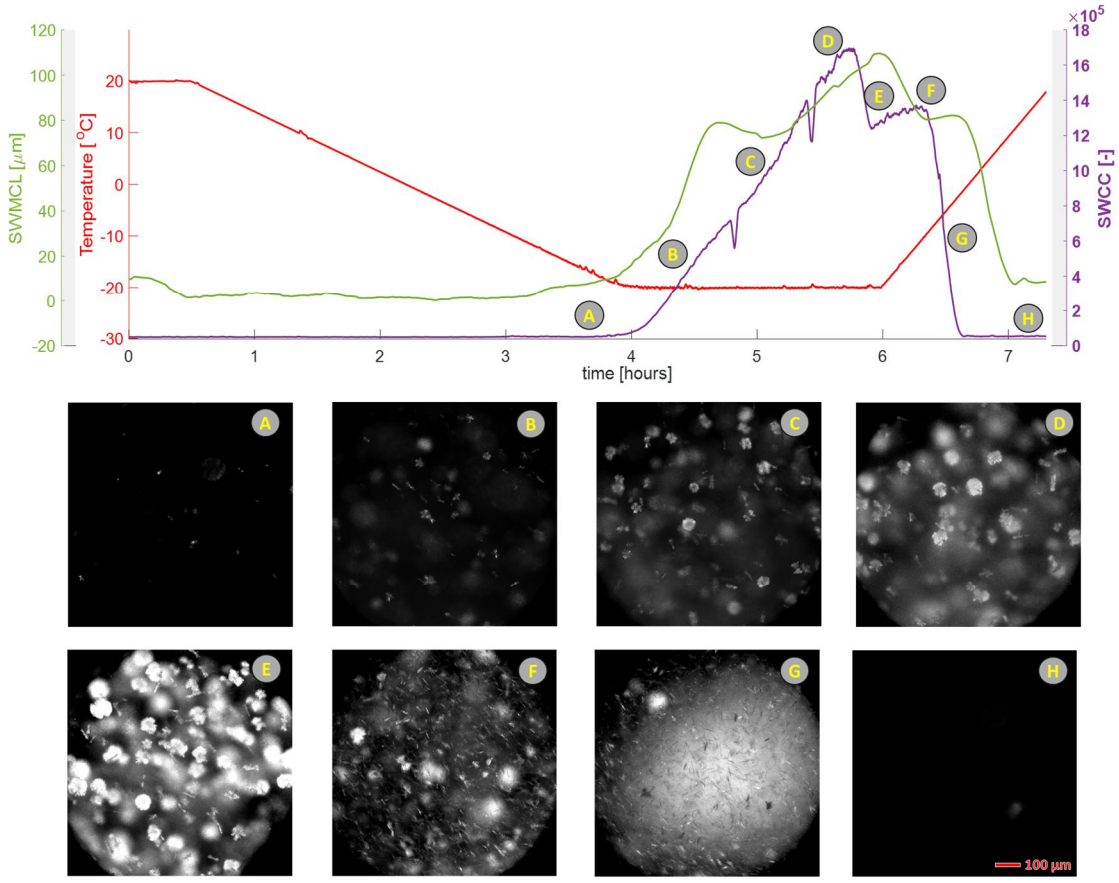

Figure 5.8 - Experimental trends of Exp1 for PZQ crystallization: SWMCL (green), SWCC (purple), temperature (red). Images obtained by online microscopy (A to H) are indicated.

Figure 5.9 presents the results obtained for Exp2. Again, the beginning of particle formation is detected at point A, indicated by the increase in SWMCL and SWCC. The formation of spherical agglomerates was also observed. At point E, the decrease in chord counts and the increase in mean chord length to a high value are evidenced by the large clusters, making the proper interpretation of such data difficult. Given these phenomena, we decided to include a short period using a fast heating rate (5 $℃/min$) to reduce the particles' size. Again, the deagglomeration exhibited a rapid response upon heating, in which large agglomerates were almost completely eliminated with the fast heating rate (point F). Afterward, the experiment followed the initial heating rate (0.2 $℃/min$), in which the dissolution occurred by the decrease of the crystal's size (points G and H).

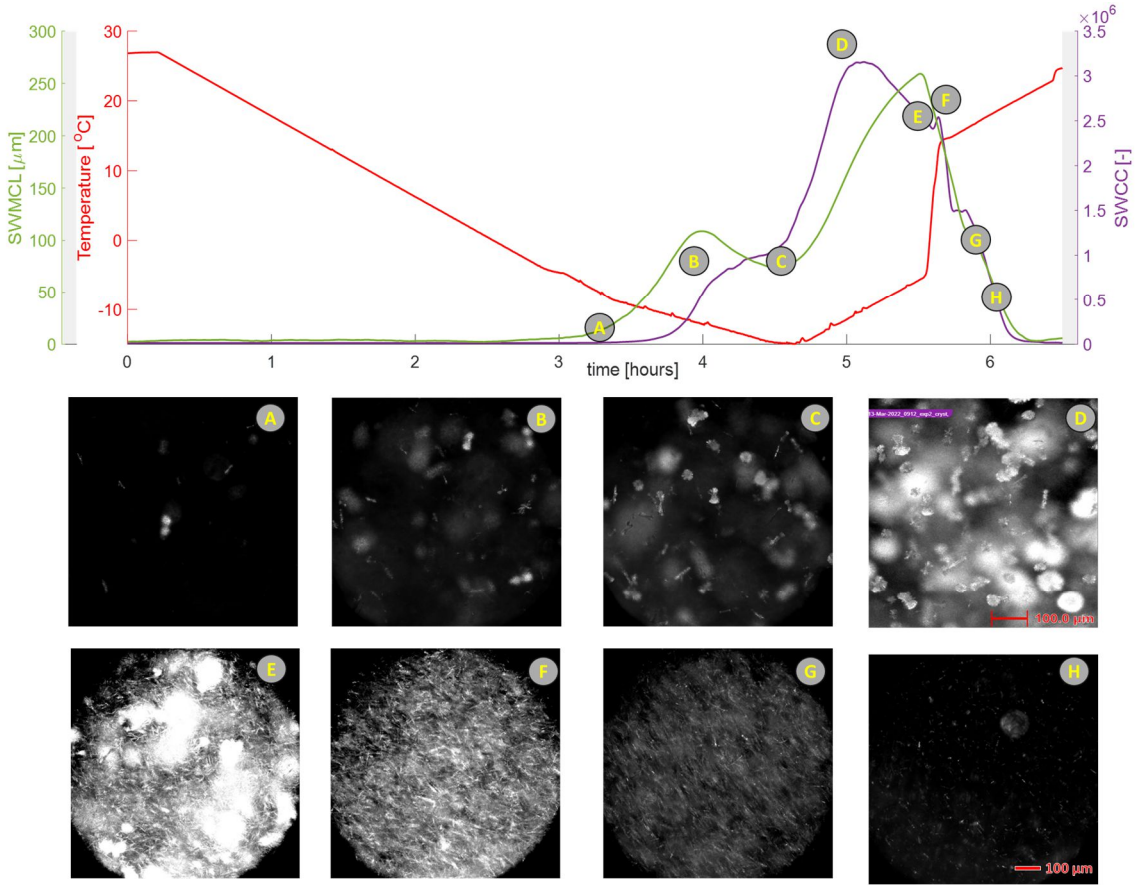

Figure 5.9 - Experimental trends of Exp2 for PZQ crystallization: SWMCL (green), SWCC (purple), temperature (red). Images obtained by online microscopy (A to H) are indicated.

The results of Exp3 are shown in Figure 5.10. For this experiment, the calibration step is shown just for illustrative purposes. During the calibration step, crystallization occurred, which is indicated by the increase in chord counts and mean chord length. Since the concentration used in this experiment was already high, one would expect that, at very low temperatures, nucleation could occur. In this case, the time at zero degrees was enough to reach the induction time. The temperature was increased to circumvent this problem and the calibration step continued until a clear solution was guaranteed again.

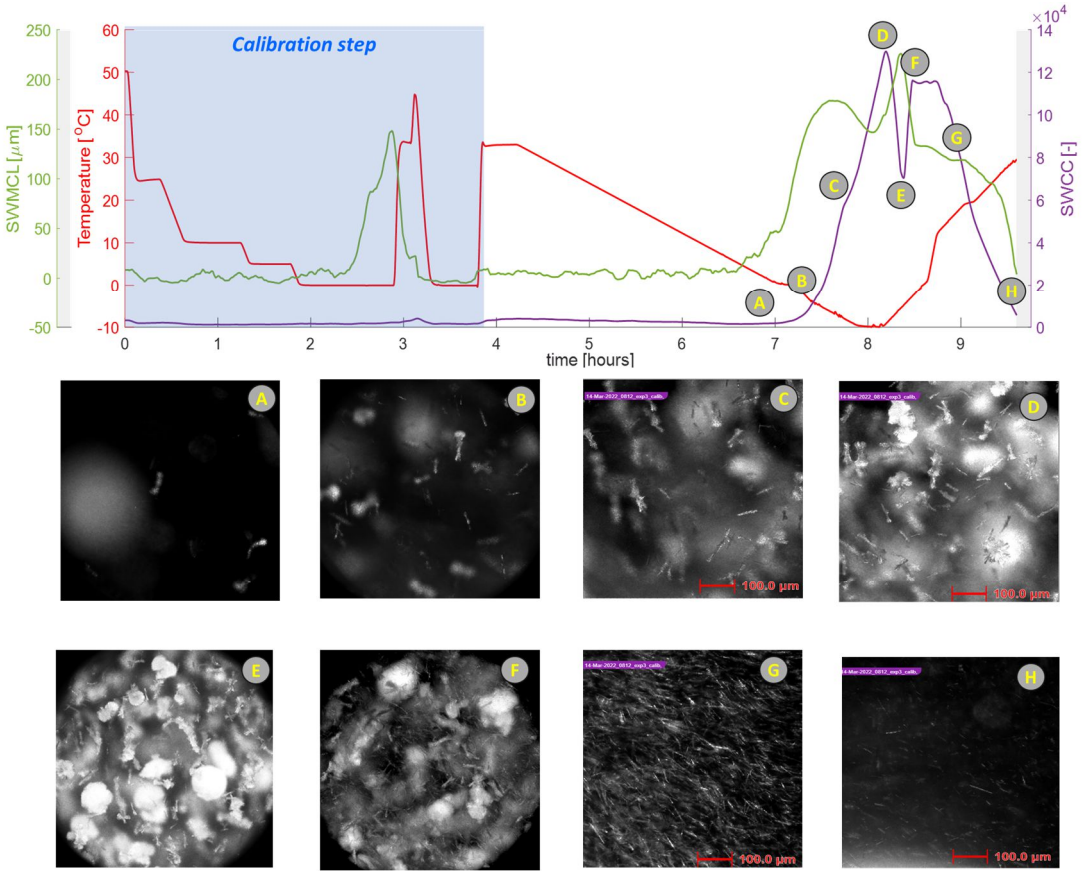

Figure 5.10 - Experimental trends of Exp3 for PZQ crystallization: SWMCL (green), SWCC (purple), temperature (red). Images obtained by online microscopy (A to H) are indicated.

Under this conditions of supersaturation, the phenomenon of nucleation seems to compete with agglomeration, which is evident at point D in Figure 5.10, corresponding to a maximum for SWCC, but was reached with a decrease in the average particle size. This trend reversed at point E, in which the images shows that the spherical agglomerates appeared expressively, decreasing the number of particles and increasing their average size.

Exp4 was the one that presented the least similar behavior when compared to the other experiments (Figure 5.11).

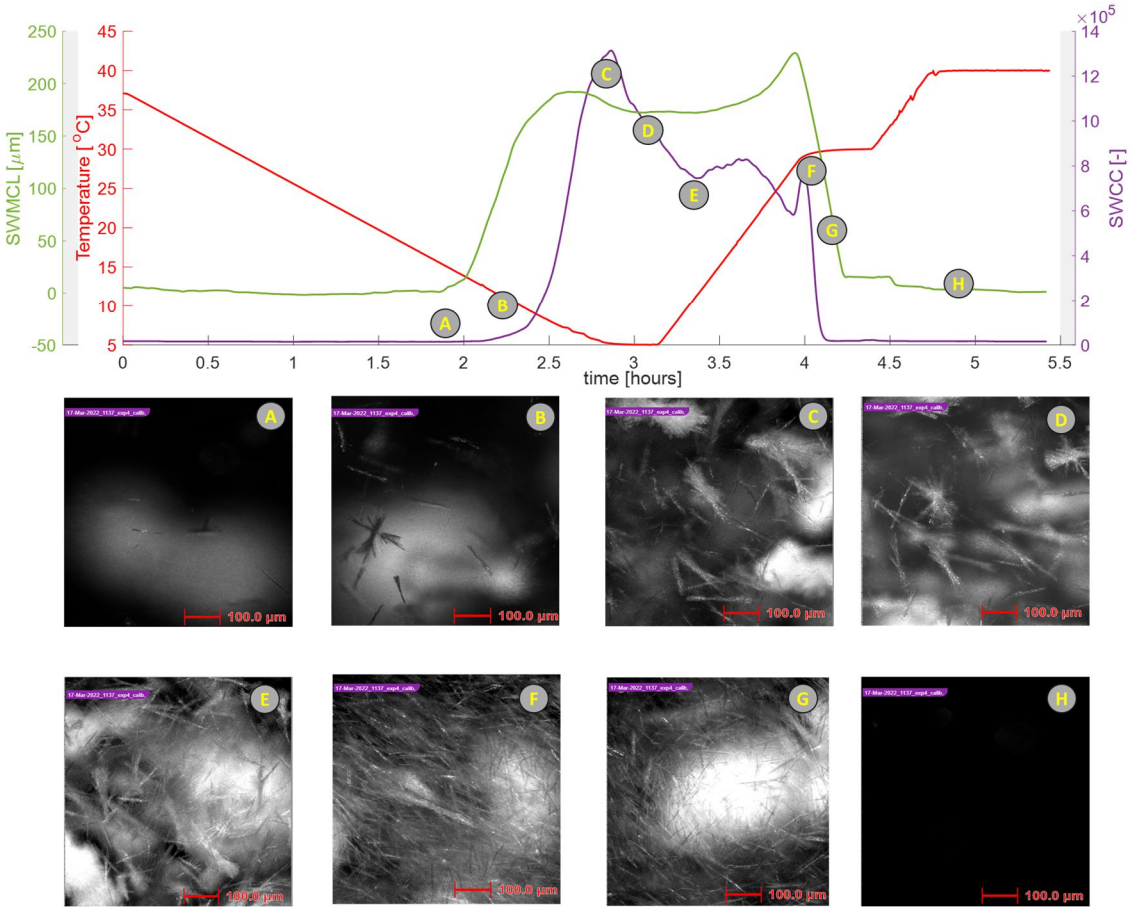

Figure 5.11 - Experimental trends of Exp4 for PZQ crystallization: SWMCL (green), SWCC (purple), temperature (red). Images obtained by online microscopy (A to H) are indicated.

Initially, the formation of spherical agglomerates was not perceived in Exp4, which shows that the temperature and supersaturation of the medium influence their occurrence. These are the only conditions different from the other experiments, as they were all performed in similar uniform fluid dynamic conditions. Agglomerates (points D and E) still existed, but no longer in spherical form but as star-shaped ones. A lesser degree of agglomeration is evidenced, and the isolated crystals were larger than those in the previous experiments. Around t = 3.9 h (shortly before point F), agglomeration had its most pronounced effect due to the decrease in SWCC and a significant increase in SWMCL. At point F, deagglomeration was observed due to heating, where individual crystals were mainly obtained, without any star-shaped agglomerates.

In conclusion, in all experiments, the sensitivity of deagglomeration to the heating effect is perceptible for the studied system. It can be measured with good agreement by the decrease in SWCC and increase in SWMCL for all cases.

Once again, online microscopy proved valuable and adequate for monitoring these processes. Explaining the phenomena during the experiments was possible based on the experimental evidence acquired with this technique.

Thus, the experiments could provide important information about the crystallization of praziquantel in ethanol, such as determining MSZW and obtaining modeling that considers the agglomeration phenomena.

It is worth mentioning the obtaining of spherically agglomerated crystals in Exp1, Exp2, and Exp3. Although it is difficult to handle from a modeling point of view, especially for agglomeration terms in a population balance approach, spherical crystallization can be operationally desired due to the formation of regular-shaped particles, which facilitates downstream steps such as filtration. For the case of APIs like PZQ, where individual needle-like crystals are observed, spherical crystallization can be attractive. It can be related to a property of agglomerate aging: if the growth rate is greater than the agglomeration rate, the agglomerates can be aged to this spherical form.

Chapter 6

Conclusions and Future Directions

The present work combines advances in cooling crystallization processes both from a modeling and control point of view and from an experimental point of view. Although in different focuses, this study highlights the vast application of this technique, whether for controlling the size and shape of crystals in industrial processes or discovering new polymorphic forms.

The crystallization processes by cooling the inorganic salts K_2SO_4 and KDP allowed the development of mathematical modeling via population balance using ex-situ image analysis data. A sampling loop was used continuously during the processes. The good prediction obtained by the developed models regarding the moments of the size distribution shows that this technique proved suitable for monitoring these processes. Also, a methodology for estimating crystallization kinetics parameters was developed based on image analysis measurements. For crystallization processes, it is a common practice to use information about the crystalline phase in the objective function only for some points in the batches, usually using CSD data at the end of the experiment. Although it provides complete information on the CSD, using the data in just a few points can impair the understanding and proper estimation of parameters in cases where dynamics are more challenging to capture. In this work, even using the moments of the distributions (and not the complete CSD), the fact of introducing in the objective function the measures of all the variables present in the model throughout the

entire process (data in each sampling interval) presents an effective approach for validating and obtaining a digital twin for the operations studied.

Even though it does not represent the entire CSD, the rapid acquisition of measured values for these variables at every sampling time, using the interface implemented in the image analyzer, decreases the numerical solution's complexity when solving the equations of moments. Thus, it facilitates the proposition for schemes of online feedback control.

Size and shape control schemes were investigated through deterministic simulations to produce crystals of desired criteria for different control targets. In the control study for the crystallization process of K_2SO_4, the use of predictive control based on empirical modeling via recurrent neural networks framework was explored, showing the potential application of machine learning in which it is possible to capture the dynamics of processes and achieve the desired control targets for the crystals.

For KDP crystallization, a bivariate PBM incorporating nucleation and growth (in supersaturation conditions) and dissolution and disappearance (in undersaturation conditions) was obtained. The presented optimal control strategy application is experimentally suitable for closed-loop control, calculating the temperature setpoints based on the optimal supersaturation policies. This approach is expected to be applied to different compounds and measuring techniques to investigate the mass, size, and the crystal shape.

The investigation of praziquantel polymorphism using systematic crystallization techniques was performed for the first time. The study for praziquantel specifically led to the discovery of two new anhydrous forms and one solvate. However, the study generally presents a systematic methodology that aids the cooling crystallization technique to maintain its crown concerning the polymorphic investigation. Although many techniques via mechanochemistry are currently being explored to obtain cocrystals and new forms, the study shows that using crystallization by cooling with a due experimental screening of essential

factors can lead to better results from the point of view of crystallinity, yield, and cost in the adopted procedures. Namely, selecting the solvent and propitiating nucleation in different scenarios (agitation, pre-filtration of the mother solution, and rate of supersaturation generation) proved crucial for obtaining different polymorphs. The present study also points explicitly out that vapor diffusion experiments have great potential to be combined with the crystallization technique, especially from the point of view of the desolvation phenomenon.

From the point of view of the pharmaceutical engineering, the discovery of new anhydrous forms G and H and the evaluation of the PZQ-HH2 hydrate are important, making it possible to obtain new formulations after due investigation of these new solid forms. Biopharmaceutical properties should be investigated for this, highlighting the determination of water saturation solubility, intrinsic dissolution rate, physical stability, and in vitro and in vivo bioactivity against Schistosoma (e.g., S. mansoni). Especially Form G has great potential since it has good physical stability, being more stable than the other forms but less than the A form. It would allow for a more favourable water solubility and dissolution rate, producing good activity levels using a less therapeutic dose.

PZQ solubility data in different organic solvents were made possible using a medium throughput screening, in which small amounts of solute are spent using microvials. The subsequent investigation of praziquantel crystallization mapped favorable conditions for spherical crystallization, using the SWCC and SWMCL variables (for analyzing cube-weighted images) representative of the process, especially for evaluating the agglomeration phenomenon. Even under this phenomenon, the agglomeration response to the increase in temperature has a fast dynamic, allowing the complete elimination of agglomerates and preserving the average size of the crystals.

In this way, the advances in cooling crystallization obtained in this thesis can be used in crystallization processes in their different conception phases, focusing on the optimal operation or developing new formulations. As future

suggestions for the studies carried out, the following venues can be explored as a continuation of this thesis.

1. **Exploring the crystallization of praziquantel**: First, elucidating the agglomeration phenomenon is essential, especially concerning the evaluation of spherical crystallization for this process. Obtaining representative phenomenological modeling that considers nucleation, growth, agglomeration/deagglomeration, and dissolution is important for this purpose, especially from the point of view of agglomeration control. Moreover, using convolutional neural networks (CNN) is attractive for extracting image features for detection and control.

2. **Exploring the polymorphism experiments on different scales**: In addition to crystallization in microvial crystallizers, investigating polymorphism on a larger scale can allow comparison and investigation of the volume effect. The systematic study can therefore be applied to praziquantel, given the systematics adopted in this study.

3. **Determination of biopharmaceutical properties and bioactivity of the new PZQ polymorphs:** Determining water solubility, in vitro and in vivo bioactivities, and physical stability of Forms G, H, and PZQ-HH2 is essential to decide whether these forms can significantly impact the PZQ formulation to reduce the therapeutic dose and guarantee good bioavailability.

4. **Validating the developed size and shape control schemes experimentally**: The experimental validation of the control schemes in the experimental apparatus of the present research group is important to make it possible to investigate different scenarios and obtain accurate results for the control of size and shape. This study may be carried out

initially using the studied inorganic salts. However, with the proper modeling chosen, the control frameworks can be extended to other processes.

5. **Integrating the simulated moving bed with the crystallization unit for praziquantel crystallization**: The praziquantel (PZQ) studied in this work is the commercial form, which is a racemate. However, only the R enantiomer (R-PZQ) is bioactive. In the present research group, works were dedicated to studying the separation of enantiomers via a simulated moving bed. Therefore, integrating the processes to obtain the crystallization of the R-PZQ after the separation becomes interesting. A concentration step (solvent removal) of the (R)-PZQ stream coming from the SMB must be established before the crystallization step. The crystallization of (R)-PZQ in batch cooling using image analysis can thus be used to develop modeling and control the size and shape of the crystals in the process, using the methodology developed and validated in the present study.

6. **Extending the polymorphism study of praziquantel to the pure bioactive enantiomer (R-PZQ)**: There are no studies in the literature investigating the polymorphism of R-PZQ. So far, only two crystalline forms as hydrates have been reported for this compound. Therefore, searching for the crystallization of anhydrous forms and investigating the existence of other polymorphs is crucial to enhance this API formulation.

References

[1] Ahn, B.; Bosetti, L.; Mazzotti, M. Secondary Nucleation by Interparticle Energies. II. Kinetics. Crystal Growth & Design 2022, 22 (1), 74–86. https://doi.org/10.1021/acs.cgd.1c00928.

[2] Zhang, Z.; Babayomi, O.; Dragicevic, T.; Heydari, R.; Garcia, C.; Rodriguez, J.; Kennel, R. Advances and Opportunities in the Model Predictive Control of Microgrids: Part I–Primary Layer. International Journal of Electrical Power & Energy Systems 2022, 134, 107411, https://doi.org/10.1016/j.ijepes.2021.107411.

[3] Tang W, Quan Y, Gong J, Wang J, Yin Q, Li T. Form selection of concomitant polymorphs: A case study informed by crystallization kinetics modeling. AIChE J. 2021, 67, 1-16. https://doi.org/10.1002/aic.17129

[4] Su, P.-C.; Ward, J. D. Modeling of Membrane-Assisted Seeded Batch Crystallization. Ind. Eng. Chem. Res. 2019, 58 (36), 16787–16797. https://doi.org/10.1021/acs.iecr.9b02935.

[5] Braatz, R. D.; Hasebe, S. Particle size and shape control in crystallization processes, In: Rawlings, J. B.; Ogunnaike, B. A.; Eaton, J. W. (Ed.), AIChE Symposium Series 2002, 98, 326, AIChE Press, 307-327, 2002.

[6] Randolph, A.; Larson, M. Theory of Particulate Processes, Analysis and Techniques of Continuous Crystallization; Academic Press: Salt Lake City, UT, 1988.

[7] Kempkes, M.; Eggers, J.; Mazzotti, M. Measurement of Particle Size and Shape by FBRM and in Situ Microscopy. Chemical Engineering Science 2008, 63 (19), 4656–4675. https://doi.org/10.1016/j.ces.2007.10.030.

[8] Lewis, A.; Seckler, M.; Kramer, H.; Van Rosmalen, G. Industrial Crystallization: Fundamentals and Application, 1. ed. Cambridge University Press, 2015.

[9] Christofides, P. D.; El-Farra, N.; Li, M.; Mhaskar, P. Model-Based Control of Particulate Processes. Chem. Eng. Sci. 2008, 63 (5), 1156−1172. https://doi.org/10.1016/j.ces.2007.07.017

[10] Mesbah, A.; Kramer, H. J. M.; Huesman, A. E. M.; Van den Hof, P. M. J. A Control Oriented Study on the Numerical Solution of the Population

Balance Equation for Crystallization Processes. Chem. Eng. Sci. 2009, 64 (20), 4262–4277. https://doi.org/10.1016/j.ces.2009.06.06.

[11] Rawlings, J. B.; Miller, S. M.; Witkowski, W. R. Model Identification and Control of Solution Crystallization Processes – a Review. Ind. Eng. Chem. Res. 1993, 32, 1275–1296.

[12] Worlitschek, J.; Mazzotti, M. Model-based optimization of particle size distribution in batch-cooling crystallization of paracetamol. Cryst. Growth Des. 2004, 4, 891 – 903. https://doi.org/10.1021/cg034179b

[13] Gherras, N.; Fevotte, G. On the use of process analytical technologies and population balance equations for the estimation of crystallization kinetics. A case study. AIChE J. 2012, 58, 2650–2664. https://doi.org/10.1002/aic.12776

[14] Ó'Ciardhá, C. T.; Hutton, K. W.; Mitchell, N. A.; Frawley, P. J. Simultaneous parameter estimation and optimization of a seeded antisolvent crystallization. Cryst. Growth Des. 2012, 12, 5247–5261. https://doi.org/10.1021/cg3006822

[15] Borsos, A.; Majumder, A.; Nagy, Z. K. Multi-Impurity Adsorption Model for Modeling Crystal Purity and Shape Evolution during Crystallization Processes in Impure Media. Cryst. Growth Des. 2016, 16, 555–568. https://doi.org/10.1021/acs.cgd.5b00320.

[16] Gomez, L. G. E.; Bommarius, A. S.; Rousseau, R. W. Crystallization Kinetics of Ampicillin Using Online Monitoring Tools and Robust Parameter Estimation. Ind. Eng. Chem. Res. 2016, 55, 2153–2162. https://doi.org/10.1021/acs.iecr.5b03880

[17] Li, H.; Kawajiri, Y.; Grover, M. A.; Rousseau, R. W. Modeling of nucleation and 34 growth kinetics for unseeded batch cooling crystallization. Ind. Eng. Chem. Res. 2017, 56, 4060–4073. https://doi.org/10.1021/acs.iecr.6b04914

[18] Trampuž, M.; Teslić, D.; Likozar, B. Crystallization of fesoterodine fumarate active pharmaceutical ingredient: Modelling of thermodynamic equilibrium, nucleation, growth, agglomeration and dissolution kinetics and temperature cycling. Chem. Eng. Sci. 2019, 201, 97–111. https://doi.org/10.1016/j.ces.2019.02.019

[19] Liu, Y. C.; Acevedo, D.; Yang, X.; Naimi, S.; Wu, W.; Pavurala, N.; Nagy, Z. K.; O'Connor, T. F. Population Balance Model Development Verification and Validation of Cooling Crystallization of Carbamazepine. Cryst. Growth Des. 2020, 20, 5235–5250. https://doi.org/10.1021/acs.cgd.0c00434

[20] Szilagyi, B.; Eren, A.; Quon, J. L.; Papageorgiou, C. D.; Nagy, Z. K. Application of Model-Free and Model-Based Quality-by-Control (QbC) for the Efficient Design of Pharmaceutical Crystallization Processes. Cryst. Growth Des. 2020, 20, 3979−3996. https://doi.org/10.1021/acs.cgd.0c00295

[21] Kim, Y.; Kawajiri Y.; Rousseau R. W.; Grover, M. A. Modeling of Nucleation, Growth, Dissolution, and Disappearance of Paracetamol in Ethanol Solution for Unseeded Batch Cooling Crystallization with Temperature-Cycling Strategy. ChemRxiv.Cambridge: Cambridge Open Engage 2020. https://doi.org/10.26434/chemrxiv.13011491.v1.

[22] Bosetti, L.; Mazzotti, M. Population Balance Modeling of Growth and Secondary Nucleation by Attrition and Ripening. Cryst. Growth Des. 2020, 20, 307−319. https://doi.org/10.1021/acs.cgd.9b01240.

[23] Moraes, M. G. F.; Grover, M. A.; Souza Jr., M. B.; Lage, P. C.; Secchi, A. R. Optimal Control of Crystal Size and Shape in Batch Crystallization Using a Bivariate Population Balance Modeling. IFAC PapersOnLine 2021, 54 (3), 653-660, https://doi.org/10.1016/j.ifacol.2021.08.316.

[24] Szilagyi, B.; Eren, A.; Quon, J. L.; Papageorgiou, C. D.; Nagy, Z. K. Digital Design of the Crystallization of an Active Pharmaceutical Ingredient Using a Population Balance Model with a Novel Size Dependent Growth Rate Expression. FromDevelopment of a Digital Twin to In Silico Optimization and Experimental Validation. Cryst. Growth Des. 2022, 22, 497−512. https://doi.org/10.1021/acs.cgd.1c01108.

[25] Pérez-Calvo, J. F.; Kadam, S. S.; Kramer, H. J. M. Determination of kinetics in batch cooling crystallization processes - A sequential parameter estimation approach. AIChE J. 2016, 62 (11), 3992-4012. https://doi.org/10.1002/aic.15295.

[26] Morris, G.; Power, G.; Ferguson, S.; Barrett, M.; Hou, G.; Glennon, B. Estimation of Nucleation and Growth Kinetics of Benzoic Acid by Population Balance Modeling of a Continuous Cooling Mixed Suspension, Mixed Product Removal Crystallizer. Org. Process Res. Dev. 2015, 19 (12), 1891−1902. https://doi.org/10.1021/acs.oprd.5b00139.

[27] Quintana-Hernández, P.; Bolaños-Reynoso, E.; Miranda-Castro, B.; Salcedo-Estrada, L. Mathematical Modeling and Kinetic Parameter Estimation in Batch Crystallization. AIChE J. 2004, 50 (7), 1407−1417. https://doi.org/10.1002/aic.10133.

[28] Simon, L. L.; Pataki, H.; Marosi, G.; Meemken, F.; Hungerbühler, K.; Baiker, A.; Tummala, S.; Glennon, B.; Kuentz, M.; Steele, G.; Kramer, H. J. M.; Rydzak, J. W.; Chen, Z.; Morris, J.; Kjell, F.; Singh, R.; Gani, R.; Gernaey, K. V.; Louhi-Kultanen, M.; O'Reilly, J.; Sandler, N.; Antikainen,

O.; Yliruusi, J.; Frohberg, P.; Ulrich, J.; Braatz, R. D.; Leyssens, T.; von Stosch, M.; Oliveira, R.; Tan, R. B. H.; Wu, H.; Khan, M.; O'Grady, D.; Pandey, A.; Westra, R.; Delle-Case, E.; Pape, D.; Angelosante, D.; Maret, Y.; Steiger, O.; Lenner, M.; Abbou-Oucherif, K.; Nagy, Z. K.; Litster, J. D.; Kamaraju, V. K.; Chiu, M.-S. Assessment of Recent Process Analytical Technology (PAT) Trends: A Multiauthor Review. Org. Process Res. Dev. 2015, 19 (1), 3–62. https://doi.org/10.1021/op500261y

[29] Bordui, P. F.; Loiacono, G. M. In-Line Bulk Supersaturation Measurement By Electrical Conductometry in KDP Crystal Growth From Aqueous Solution. Journal of Crystal Growth 1984, 67, 168-172. https://doi.org/10.1016/0022-0248(84)90175-1

[30] Hu, Q.; Rohani, S.; Wang, D. X.; Jutan, A. Nonlinear Kinetic Parameter Estimation for Batch Cooling Seeded Crystallization. AIChE J. 2004, 50 (8), 1786–1794. https://doi.org/10.1002/aic.10163.

[31] Aamir, E.; Nagy, Z. K.; Rielly, C. D.; Kleinert, T.; Judat, B. Combined Quadrature Method of Moments and Method of Characteristics Approach for Efficient Solution of Population Balance Models for Dynamic Modeling and Crystal Size Distribution Control of Crystallization Processes. Ind. Eng. Chem. Res. 2009, 48, 8575−8584. https://doi.org/10.1021/ie900430t

[32] Oliva J. A.; Wu, W.L.; Greene, M.R.; Pal, K.; Nagy, Z.K., Continuous spherical crystallization of lysozyme in an oscillatory baffled crystallizer using emulsion solvent diffusion in droplets, Cryst. Growth Des. 2020, 20 (2), 934–947, https://doi.org/10.1021/acs.cgd.9b01313.

[33] Larsen, P. A.; Rawlings, J. B.; Ferrier, N. J. An algorithm for analyzing noisy, in situ images of high-aspect-ratio crystals to monitor particle size distribution. Chem. Eng. Sci. 2006, 61, 5236−5248. https://doi.org/10.1016/j.ces.2006.03.035

[34] Kong, Y.; Zhuang, Y.; Yu, J.; Han, Z.; Shi, B. Structural Study on PVA Assisted Self-Assembled 3D Hierarchical Iron (Hydr)Oxides. CrystEngComm 2018, 20 (15), 2093–2101. https://doi.org/10.1039/C8CE00075A.

[35] Czapla, F.; Kail, N.; Oncul, A.; Lorenz, H.; Briesen, H.; SeidelMorgenstern, A. Application of a recent FBRM-probe model to quantify preferential crystallization of DL-threonine. Chem. Eng. Res. Des. 2010, 88, 1494−1504. https://doi.org/10.1016/j.cherd.2010.03.004

[36] Worlitschek, J.; Hocker, T.; Mazzotti, M. Restoration of PSD from Chord Length Distribution Data Using the Method of Projections onto Convex Sets. Part. Part. Syst. Charact. 2005, 22 (2), 81–98. https://doi.org/10.1002/ppsc.200400872.

[37] Szilágyi, B.; Nagy, Z. K. Aspect Ratio Distribution and Chord Length Distribution Driven Modeling of Crystallization of Two-Dimensional Crystals for Real-Time Model-Based Applications. Crystal Growth & Design 2018, 18 (9), 5311–5321. https://doi.org/10.1021/acs.cgd.8b00758.

[38] Szilágyi, B.; Eren, A.; Quon, J. L.; Papageorgiou, C. D.; Nagy, Z. K. Application of Model-Free and Model-Based Quality-by-Control (QbC) for the Efficient Design of Pharmaceutical Crystallization Processes. Crystal Growth & Design 2020, 20 (6), 3979–3996. https://doi.org/10.1021/acs.cgd.0c00295.

[39] Eren, A.; Szilagyi, B.; Quon, J. L.; Papageorgiou, C. D.; Nagy, Z. K. Experimental Investigation of an Integrated Crystallization and Wet-Milling System with Temperature Cycling to Control the Size and Aspect Ratio of Needle-Shaped Pharmaceutical Crystals. Crystal Growth & Design 2021, 21 (7), 3981–3993. https://doi.org/10.1021/acs.cgd.1c00308.

[40] Eggers, J.; Kempkes, M.; Mazzotti, M. Measurement of Size and Shape Distributions of Particles through Image Analysis. Chemical Engineering Science 2008, 63 (22), 5513–5521. https://doi.org/10.1016/j.ces.2008.08.007.

[41] Schorsch, S.; Vetter, T.; Mazzotti, M. Measuring Multidimensional Particle Size Distributions during Crystallization. Chemical Engineering Science 2012, 77, 130–142. https://doi.org/10.1016/j.ces.2011.11.029.

[42] Heisel, S.; Ernst, J.; Emshoff, A.; Schembecker, G.; Wohlgemuth, K. Shape-Independent Particle Classification for Discrimination of Single Crystals and Agglomerates. Powder Technology 2019, 345, 425–437. https://doi.org/10.1016/j.powtec.2019.01.018.

[43] Temmel, E.; Gänsch, J.; Lorenz, H.; Seidel-Morgenstern, A. Measurement and Evaluation of the Crystallization Kinetics of L -Asparagine Monohydrate in the Ternary L -/ D -Asparagine/Water System. Crystal Growth & Design 2018, 18 (12), 7504–7517. https://doi.org/10.1021/acs.cgd.8b01322.

[44] Borchert, C.; Temmel, E.; Eisenschmidt, H.; Lorenz, H.; Seidel-Morgenstern, A.; Sundmacher, K. Image-Based in Situ Identification of Face Specific Crystal Growth Rates from Crystal Populations. Cryst. Growth Des. 2014, 14, 952−971. https://doi.org/10.1021/cg401098x

[45] Omar, W. Experimental Investigations of Adipic Acid Agglomeration Behavior under Different Operating Conditions Using Image Analysis Technique QICPIC Software. Particulate Science and Technology 2020, 38 (6), 740–746. https://doi.org/10.1080/02726351.2019.1620386.

[46] Eisenschmidt, H.; Bajcinca, N.; Sundmacher, K. Optimal Control of Crystal Shapes in Batch Crystallization Experiments by Growth-

Dissolution Cycles. Crystal Growth & Design 2016, 16 (6), 3297–3306. https://doi.org/10.1021/acs.cgd.6b00288.

[47] Schiele, S. A.; Antoni, F.; Meinhardt, R.; Briesen, H. Analysis of Nonideal Shape Evolution during Potash Alum Crystallization Using Microcomputed Tomography and Three-Dimensional Image Analysis. Crystal Growth & Design 2021, 21 (3), 1751–1761. https://doi.org/10.1021/acs.cgd.0c01644.

[48] Ma, C. Y., Wang, X. Z. Closed-loop control of crystal shape in cooling crystallization of l-glutamic acid. Journal of Process Control 2012, 22, 72-81.

[49] Bötschi, S., Rajagopalan, A. K., Morari, M., Mazzotti, M. Feedback Control for the Size and Shape Evolution of Needle-like Crystals in Suspension. I. Concepts and Simulation Studies. *Crystal Growth & Design* 2018, v.18, pp. 4470-4483.

[50] Nicoud, L.; Nicordari, F.; Myerson, A. S. Polymorph control in MSMPR crystallizers. A case study with paracetamol. Organic Process Research & Development 2019, 23 (5), 794-806.

[51] Lee, A. Y.; Erdemir, D.; Myerson, A. S. Crystal Polymorphism in Chemical Process Development. *Annu. Rev. Chem. Biomol. Eng.* **2011**, *2* (1), 259–280. https://doi.org/10.1146/annurev-chembioeng-061010-114224.

[52] Lee, E. H. A Practical Guide to Pharmaceutical Polymorph Screening & Selection. *Asian Journal of Pharmaceutical Sciences* **2014**, *9* (4), 163–175. https://doi.org/10.1016/j.ajps.2014.05.002.

[53] Bernstein, J. *Polymorphism in Molecular Crystals*; International Union of Crystallography Monographs on Crystallography; Oxford University Press: Oxford, NY, 2002.

[54] Gao, Z.; Rohani, S.; Gong, J.; Wang, J. Recent Developments in the Crystallization Process: Toward the Pharmaceutical Industry. *Engineering* 2017, *3* (3), 343–353. https://doi.org/10.1016/J.ENG.2017.03.022.

[55] El-Arini, S. K.; Leuenberger, H. Dissolution Properties of Praziquantel–PVP Systems. *Pharmaceutica Acta Helvetiae* 1998, *73* (2), 89–94. https://doi.org/10.1016/S0031-6865(97)00051-4.

[56] WHO. WHO Model List of Essential Medicines, 19th edition (April 2015). Available at: https://www.who.int/publications/i/item/WHO-MHP-HPS-EML-2021.02. Accessed May 20, 2022.

[57] Werneck, G. L.; Hasselmann, M. H.; Gouvêa, T. G. Panorama dos estudos sobre nutrição e doenças negligenciadas no Brasil. *Ciênc. saúde coletiva* 2011, *16* (1), 39–62. https://doi.org/10.1590/S1413-81232011000100009.

[58] McManus, D. P.; Dunne, D. W.; Sacko, M.; Utzinger, J.; Vennervald, B. J.; Zhou, X.-N. Schistosomiasis. Nat Rev Dis Primers 2018, 4 (1), 13. https://doi.org/10.1038/s41572-018-0013-8.

[59] Colley, D. G.; Bustinduy, A. L.; Secor, W. E.; King, C. H. Human Schistosomiasis. *The Lancet* **2014**, *383* (9936), 2253–2264. https://doi.org/10.1016/S0140-6736(13)61949-2.

[60] World Health Organization. *Establishing and Strengthening Immunization in the Second Year of Life: Practices for Vaccination beyond Infancy*; World Health Organization: Geneva, 2018.

[61] Cugovčan, M.; Jablan, J.; Lovrić, J.; Cinčić, D.; Galić, N.; Jug, M. Biopharmaceutical Characterization of Praziquantel Cocrystals and Cyclodextrin Complexes Prepared by Grinding. *Journal of Pharmaceutical and Biomedical Analysis* **2017**, *137*, 42–53. https://doi.org/10.1016/j.jpba.2017.01.025.

[62] Devogelaer, J.-J.; Charpentier, M. D.; Tijink, A.; Dupray, V.; Coquerel, G.; Johnston, K.; Meekes, H.; Tinnemans, P.; Vlieg, E.; ter Horst, J. H.; de Gelder, R. Cocrystals of Praziquantel: Discovery by Network-Based Link Prediction. *Crystal Growth & Design* **2021**, *21* (6), 3428–3437. https://doi.org/10.1021/acs.cgd.1c00211.

[63] Espinosa-Lara, J. C.; Guzman-Villanueva, D.; Arenas-García, J. I.; Herrera-Ruiz, D.; Rivera-Islas, J.; Román-Bravo, P.; Morales-Rojas, H.; Höpfl, H. Cocrystals of Active Pharmaceutical Ingredients—Praziquantel in Combination with Oxalic, Malonic, Succinic, Maleic, Fumaric, Glutaric, Adipic, And Pimelic Acids. *Crystal Growth & Design* **2013**, *13* (1), 169–185. https://doi.org/10.1021/cg301314w.

[64] Rodríguez-Ruiz, C.; Salas-Zúñiga, R.; Sánchez-Guadarrama, M. O.; Delgado-Díaz, A.; Herrera-Ruiz, D.; Morales-Rojas, H.; Höpfl, H. Structural, Physicochemical, and Biopharmaceutical Properties of Cocrystals with *RS*- and *R*-Praziquantel─Generation and Prolongation of the Supersaturation State in the Presence of Cellulosic Polymers. *Crystal Growth & Design* **2022**, *22* (10), 6023–6038. https://doi.org/10.1021/acs.cgd.2c00661.

[65] Sánchez-Guadarrama, O.; Mendoza-Navarro, F.; Cedillo-Cruz, A.; Jung-Cook, H.; Arenas-García, J. I.; Delgado-Díaz, A.; Herrera-Ruiz, D.; Morales-Rojas, H.; Höpfl, H. Chiral Resolution of *RS*-Praziquantel via Diastereomeric Co-Crystal Pair Formation with L-Malic Acid. *Crystal Growth & Design* **2016**, *16* (1), 307–314. https://doi.org/10.1021/acs.cgd.5b01254.

[66] Saikia, B.; Seidel-Morgenstern, A.; Lorenz, H. Role of Mechanochemistry in Solid Form Selection and Identification of the Drug Praziquantel.

Crystal Growth & Design **2021**, *21* (10), 5854–5861. https://doi.org/10.1021/acs.cgd.1c00736.

[67] Salazar-Rojas, D.; Maggio, R. M.; Kaufman, T. S. Preparation and Characterization of a New Solid Form of Praziquantel, an Essential Anthelmintic Drug. Praziquantel Racemic Monohydrate. *European Journal of Pharmaceutical Sciences* **2020**, *146*, 105267. https://doi.org/10.1016/j.ejps.2020.105267.

[68] Zanolla, D.; Perissutti, B.; Passerini, N.; Chierotti, M. R.; Hasa, D.; Voinovich, D.; Gigli, L.; Demitri, N.; Geremia, S.; Keiser, J.; Cerreia Vioglio, P.; Albertini, B. A New Soluble and Bioactive Polymorph of Praziquantel. *European Journal of Pharmaceutics and Biopharmaceutics* **2018**, *127*, 19–28. https://doi.org/10.1016/j.ejpb.2018.01.018.

[69] Zanolla, D.; Perissutti, B.; Vioglio, P. C.; Chierotti, M. R.; Gigli, L.; Demitri, N.; Passerini, N.; Albertini, B.; Franceschinis, E.; Keiser, J.; Voinovich, D. Exploring Mechanochemical Parameters Using a DoE Approach: Crystal Structure Solution from Synchrotron XRPD and Characterization of a New Praziquantel Polymorph. *European Journal of Pharmaceutical Sciences* **2019**, *140*, 105084. https://doi.org/10.1016/j.ejps.2019.105084.

[70] Zanolla, D.; Hasa, D.; Arhangelskis, M.; Schneider-Rauber, G.; Chierotti, M. R.; Keiser, J.; Voinovich, D.; Jones, W.; Perissutti, B. Mechanochemical Formation of Racemic Praziquantel Hemihydrate with Improved Biopharmaceutical Properties. *Pharmaceutics* **2020**, *12* (3), 289. https://doi.org/10.3390/pharmaceutics12030289.

[71] Zanolla, D.; Gigli, L.; Hasa, D.; Chierotti, M. R.; Arhangelskis, M.; Demitri, N.; Jones, W.; Voinovich, D.; Perissutti, B. Mechanochemical Synthesis and Physicochemical Characterization of Previously Unreported Praziquantel Solvates with 2-Pyrrolidone and Acetic Acid. *Pharmaceutics* **2021**, *13* (10), 1606. https://doi.org/10.3390/pharmaceutics13101606.

[72] Liu, Y.; Wang, X.; Wang, J.-K.; Ching, C. B. Investigation of the Phase Diagrams of Chiral Praziquantel. *Chirality* **2006**, *18* (4), 259–264. https://doi.org/10.1002/chir.20251.

[73] Meyer, T.; Sekljic, H.; Fuchs, S.; Bothe, H.; Schollmeyer, D.; Miculka, C. Taste, A New Incentive to Switch to (R)-Praziquantel in Schistosomiasis Treatment. *PLoS Negl Trop Dis* **2009**, *3* (1), e357. https://doi.org/10.1371/journal.pntd.0000357.

[74] Cedillo-Cruz, A.; Aguilar, M. I.; Flores-Alamo, M.; Palomares-Alonso, F.; Jung-Cook, H. A Straightforward and Efficient Synthesis of Praziquantel Enantiomers and Their 4′-Hydroxy Derivatives. *Tetrahedron: Asymmetry* **2014**, *25* (2), 133–140. https://doi.org/10.1016/j.tetasy.2013.11.004.

[75] Alvarez, A. J.; Singh, A.; Myerson, A. S. Polymorph Screening: Comparing a Semi-Automated Approach with a High Throughput Method. *Crystal Growth & Design* **2009**, *9* (9), 4181–4188. https://doi.org/10.1021/cg900421v.

[76] Florence, A. J.; Johnston, A.; Price, S. L.; Nowell, H.; Kennedy, A. R.; Shankland, N. An Automated Parallel Crystallisation Search for Predicted Crystal Structures and Packing Motifs of Carbamazepine. *Journal of Pharmaceutical Sciences* **2006**, *95* (9), 1918–1930. https://doi.org/10.1002/jps.20647.

[77] Karashima, M.; Kimoto, K.; Kojima, T.; Ikeda, Y. Rational Polymorph Screening Based on Slow Cooling Crystallization of Poorly Soluble Mebendazole. *Journal of Crystal Growth* **2014**, *390*, 30–37. https://doi.org/10.1016/j.jcrysgro.2013.12.014.

[78] Ouyang, J.; Chen, J.; Rosbottom, I.; Chen, W.; Guo, M.; Heng, J. Y. Y. Supersaturation and Solvent Dependent Nucleation of Carbamazepine Polymorphs during Rapid Cooling Crystallization. *CrystEngComm* **2021**, *23* (4), 813–823. https://doi.org/10.1039/D0CE01357A.

[79] Parambil, J. V.; Poornachary, S. K.; Tan, R. B. H.; Heng, J. Y. Y. Influence of Solvent Polarity and Supersaturation on Template-Induced Nucleation of Carbamazepine Crystal Polymorphs. *Journal of Crystal Growth* **2017**, *469*, 84–90. https://doi.org/10.1016/j.jcrysgro.2016.09.058.

[80] Parmar, M. M.; Khan, O.; Seton, L.; Ford, J. L. Polymorph Selection with Morphology Control Using Solvents. *Crystal Growth & Design* **2007**, *7* (9), 1635–1642. https://doi.org/10.1021/cg070074n.

[81] Shan, G. Control of Solvent-Mediated Transformation of Crystal Polymorphs Using a Newly Developed Batch Crystallizer (WWDJ-Crystallizer). *Chemical Engineering Journal* **2002**, *85* (2–3), 169–176. https://doi.org/10.1016/S1385-8947(01)00154-1.

[82] Sudha, C.; Srinivasan, K. Nucleation Control and Separation of Paracetamol Polymorphs through Swift Cooling Crystallization Process. *Journal of Crystal Growth* **2014**, *401*, 248–251. https://doi.org/10.1016/j.jcrysgro.2013.10.025.

[83] Sacchi, P.; Reutzel-Edens, S. M.; Cruz-Cabeza, A. J. The Unexpected Discovery of the Ninth Polymorph of Tolfenamic Acid. *CrystEngComm* **2021**, *23* (20), 3636–3647. https://doi.org/10.1039/D1CE00343G.

[84] McCabe, J. F. Application of Design of Experiment (DOE) to Polymorph Screening and Subsequent Data Analysis. *CrystEngComm* **2010**, *12* (4), 1110–1119. https://doi.org/10.1039/B914818C.

[85] Sistla, A.; Wu, Y.; Khamphavong, P.; Liu, J. Medium-Throughput Hydrate Screening Using the Crystal 16 ™. *Pharmaceutical Development and Technology* **2011**, *16* (2), 102–109. https://doi.org/10.3109/10837450903499366.

[86] MacEachern, L.; Kermanshahi-pour, A.; Mirmehrabi, M. Transformation under Pressure: Discovery of a Novel Crystalline Form of Anthelmintic Drug Praziquantel Using High-Pressure Supercritical Carbon Dioxide. *International Journal of Pharmaceutics* **2022**, *619*, 121723. https://doi.org/10.1016/j.ijpharm.2022.121723.

[87] Mullin, J. W.; Gaska, C. The Growth and Dissolution of Potassium Sulphate Crystals in a Fluidized Bed Crystallizer. Can. J. Chem. Eng. 1969, 47 (5), 483–489. https://doi.org/10.1002/cjce.5450470514.

[88] Randolph, A. D.; Rajagopal, K. Direct Measurement of Crystal Nucleation and Growth Rate Kinetics in Backmixed Crystal Slurry. Study of the K2SO4 System. Ind. Eng. Chem. Fund. 1970, 9 (1), 165–171. https://doi.org/10.1021/i160033a027.

[89] Randolph, A. D.; Cise, M. D. Nucleation Kinetics of the Potassium Sulfate-Water System. AIChE J. 1972, 18 (4), 798–807. https://doi.org/10.1002/aic.690180423,

[90] Jones, A. G., Budz, J., Mullin, J. W., Crystallization Kinetics of Potassium Sulfate in an MSMPR Agitated Vessel. AIChE Journal 1986, 32 (12), 2002-2009.

[91] Budz, J.; Jones, A. G.; Mullin, J. W. On the Shape-Size Dependence of Potassium Sulfate Crystals. Ind. Eng. Chem. Res. 1987, 26 (4), 820–824. https://doi.org/10.1021/ie00064a034.

[92] Jones, A. G.; Budz, J.; Mullin, J. W. Batch Crystallization And Solid-Liquid Separation Of Potassium Sulphate. Chemical Engineering Science 1987, 42 (4), 619-629 https://doi.org/10.1016/0009-2509(87)80023-4

[93] Chianese, A.; Di Berardino, F.; Jones, A. G. On the Effect of Secondary Nucleation on the Crystal Size Distribution from a Seeded Batch Crystallizer. Chemical Engineering Science 1993, 48 (3), 551–560. https://doi.org/10.1016/0009-2509(93)80309-E.

[94] Omar, W.; Ulrich, J. Influence of Crystallization Conditions on the Mechanism and Rate of Crystal Growth of Potassium Sulphate. Cryst. Res. Technol. 2003, 38 (1), 34–41. https://doi.org/10.1002/crat.200310004.

[95] Rawlings, J.B., Slink, C.W., Miller, S.M. Control of crystallization processes. In: Myerson, A.S. (Ed.), Handbook of Industrial Crystallization, 2nd ed ,2001, 201–230.

[96] Paengjuntuek, W.; Kittisupakorn, P.; Arpornwichanop, A. Optimization and Nonlinear Control of a Batch Crystallization Process. Journal of the Chinese Institute of Chemical Engineers 2008, 39 (3), 249–256. https://doi.org/10.1016/j.jcice.2007.12.017.

[97] Paengjuntuek, W.; Thanasinthana, L.; Arpornwichanop, A. Neural Network-Based Optimal Control of a Batch Crystallizer. Neurocomputing 2012, 83, 158–164. https://doi.org/10.1016/j.neucom.2011.12.008.

[98] Shi, D.; El-Farra, N. H.; Li, M.; Mhaskar, P.; Christofides, P. D. Predictive Control of Particle Size Distribution in Particulate Processes. Chemical Engineering Science 2006, 61 (1), 268–281. https://doi.org/10.1016/j.ces.2004.12.059.

[99] Zhang, W.; Chen, X.; Wang, Y.; Wu, L.; Hu, Y. Experimental and Modeling of Conductivity for Electrolyte Solution Systems. *ACS Omega* **2020**, *5* (35), 22465–22474. https://doi.org/10.1021/acsomega.0c03013.

[100] Ramkrishna, D. Population Balances: Theory and Applications to Particulate Systems in Engineering; Academic Press: San Diego, CA, 2000.

[101] Perry's Chemical Engineers' Handbook, 8th ed.; Perry, R. H., Green, D. W., Eds.; McGraw-Hill: New York, 2008.

[102] Secchi, A.R.; Pereira, F.A. Modeling and Simulation of a High Pressure Polyethylene Tubular Reactor with Axial Mixing. Latin American Applied Research, **1998**, 28 (4) 271-276.

[103] Secchi, A. R., DASSLC User's Manual Version 3.2. Universidade Federal do Rio Grande do Sul, DEQUI, Porto Alegre, RS, Brazil, 2007.

[104] Kennedy, J.; Eberhart, R. Particle Swarm Optimization. In Proceedings of ICNN'95 - International Conference on Neural Networks; IEEE: Perth, WA, Australia, 1995, 4, 1942–1948. https://doi.org/10.1109/ICNN.1995.488968.

[105] Nelder, J. A.; Mead, R. A Simplex Method for Function Minimization. The Computer Journal 1965, 7 (4), 308–313. https://doi.org/10.1093/comjnl/7.4.308.

[106] Secchi, A. R.; Cardozo, N. S. M.; Neto, E. A.; Finkler, T. F. An Algorithm For Automatic Selection And Estimation Of Model Parameters. IFAC Proceedings Volumes 2006, 39 (2), 789–794. https://doi.org/10.3182/20060402-4-BR-2902.00789.

[107] Osmari, T. A.; Gallon, R.; Schwaab, M.; Barbosa-Coutinho, E.; Severo, J. B.; Pinto, J. C. Statistical Analysis of Linear and Non-Linear Regression for the Estimation of Adsorption Isotherm Parameters. Adsorption Science & Technology 2013, 31 (5), 433–458. https://doi.org/10.1260/0263-6174.31.5.433.

[108] Tolazzi, N.; Steffani, E.; Barbosa-Coutinho, E.; Severo Júnior, J. B.; Pinto, J. C.; Schwaab, M. Adsorption Equilibrium Models: Computation of Confidence Regions of Parameter Estimates. Chemical Engineering Research and Design 2018, 138, 144–157. https://doi.org/10.1016/j.cherd.2018.08.027.

[109] Schwaab, M.; Biscaia, Jr., E. C.; Monteiro, J. L.; Pinto, J. C. Nonlinear Parameter Estimation through Particle Swarm Optimization. Chemical Engineering Science 2008, 63 (6), 1542–1552. https://doi.org/10.1016/j.ces.2007.11.024.

[110] Tatar A.; Naseri S.; Bahadori M.; Hezave A. Z.; Kashiwao T.; Bahadori A.; Darvish H. Prediction of carbon dioxide solubility in ionic liquids using MLP and radial basis function (RBF) neural networks. Journal of the Taiwan Institute of Chemical Engineers 2016, 60, 151-164. https://doi.org/10.1016/j.jtice.2015.11.002

[111] Haykin, S. S.; Haykin, S. S. Neural Networks and Learning Machines, 3rd ed.; Prentice Hall: New York, 2009.

[112] Ren J.; Ni D. A batch-wise LSTM-encoder decoder network for batch process monitoring. Chemical Engineering Research and Design 2020, 164, 102-112. https://doi.org/10.1016/j.cherd.2020.09.019

[113] Shahnazari; H. Fault diagnosis of nonlinear systems using recurrent neural networks. Chemical Engineering Research and Design 2020, 153, 233-245. https://doi.org/10.1016/j.cherd.2019.09.026

[114] Petsagkourakis P.; Sandoval I. O.; Bradford E.; Zhang D.; Del Rio-Chanona E. A. Reinforcement learning for batch bioprocess optimization. Computers and Chemical Engineering 2020,133, 106649. https://doi.org/10.1016/j.compchemeng.2019.106649

[115] Sun W.; Paiva A. R. C.; Xu P.; Sundaram A.; Braatz R. D. Fault detection and identification using Bayesian recurrent neural networks. Computers and Chemical Engineering 2020, 141, 106991. https://doi.org/10.1016/j.compchemeng.2020.106991

[116] Lillicrap T. P.; Santoro A. Backpropagation through time and the brain. Current Opinion in Neurobiology 2019, 55, 82-89. https://doi.org/10.1016/j.conb.2019.01.011

[117] Dias A. C. S. R.; Soares F. R.; Jaschke J.; Souza Jr. M. B.; Pinto J. C. Extracting Valuable Information from Big Data for Machine Learning Control: An Application for a Gas Lift Process. Processes 2019, 7(5), 252. https://doi.org/10.3390/pr7050252

[118] Matino I.; Dettori S.; Colla V.; Weber V.; Salame S. Forecasting blast furnace gas production and demand through echo state neural network-

based models: Pave the way to off-gas optimized management. Applied Energy 2019, 253, 113578. https://doi.org/10.1016/j.apenergy.2019.113578

[119] Ying-Chun B.; Xin Z. Online adaptive dynamic programming based on echo state networks for dissolved oxygen control. Applied Soft Computing 2018, 62, 830-839. https://doi.org/10.1016/j.asoc.2017.09.015

[120] Patanè L.; Xibilia M. G. Echo-state networks for soft sensor design in an SRU process. Information Sciences 2021, 566, 195-214. https://doi.org/10.1016/j.ins.2021.03.013

[121] Korndörfer C. Echo State Networks in Python. GitHub, 2015. Available from: https://github.com/cknd/pyESN

[122] Yang F.; Li K.; Zhong Z.; Luo Z.; Sun X.; Cheng H.; Guo X.; Huang F.; Ji H.; Li S. Asymmetric Co-Teaching for Unsupervised Cross-Domain Person Re-Identification. Advancement of Artificial Intelligence 2020, arXiv:1912.01349. https://doi.org/10.48550/arXiv.1912.01349

[123] Wu Z.; Luo J.; Rincon D.; Christofides P. D. Machine learning-based predictive control using noisy data: evaluating performance and robustness via a large-scale process simulator. Chemical Engineering Research and Design 2021, 168, 275-287. https://doi.org/10.1016/j.cherd.2021.02.011

[124] Rawlings, J.; Mayne, D. Q.; Diehl, M. Model Predictive Control: Theory, Computation, and Design. Nob Hill Publishing, LLC, 2017, 2nd ed.

[125] Morato M. M.; Normey-Rico J. E.; Sename O. Model predictive control design for linear parameter varying systems: A survey. Annual Reviews in Control 2020, 49, 64-80. https://doi.org/10.1016/j.arcontrol.2020.04.016

[126] Virtanen P.; Gommers R.; Oliphant T. E.; Haberland M.; Reddy T.; Cournapeau D.; Burovski E.; Peterson P.; Weckesser W.; Bright J.; Walt S. J.; Brett M.; Wilson J.; Millman K. J.; Mayorov N.; Nelson A. R. J.; Jones E.; Kern R.; Larson E.; Carey C. J.; Polat I.; Feng Y.; Moore E. W.; VanderPlas J.; Laxalde D.; Perktold J.; Cirmrman R.; Henriksen I.; Quintero E. A.; Harris C. R.; Archibald A. M.; Ribeiro A. H.; Pedregosa F.; Mulbregt P.; SciPy 1.0 Contributors. SciPy 1.0: Fundamental Algorithms for Scientific Computing in Python. Nature Methods 2020,17 (3), 261-272. https://doi.org/10.1038/s41592-019-0686-2

[127] Andersson; J.A.E.; Gillis; J.; Horn; G. et al. CasADi: a software framework for nonlinear optimization and optimal control. Math. Prog. Comp 2019, 11, 1–36. http://dx.doi.org/10.1007/s12532-018-0139-4

[128] Jiang, M., Zhu, X., Molaro, M. C., Rasche, M. L., Zhang, H., Chadwick, K., Raimondo, D. M., Kim, K. K. K., Zhou, L., Zhu, Z., Wong, M. H., O'Grady, D., Hebrault, D., Tedesco, J., Braatz, R. D. Modification of

crystal shape through deep temperature cycling. Industrial Engineering & Chemistry Research. 2014, v. 53, p. 5325–5336.

[129] Eisenschmidt, H., Voigt, A., Sundmacher, K. (2015). Face-Specific Growth and Dissolution Kinetics of Potassium Dihydrogen Phosphate Crystals from Batch Crystallization Experiments. Crystal Growth & Design, v. 15, pp. 219-227.

[130] Ma, D. L.; Tafti, D. K.; Braatz, R. D. (2002). Optimal control and simulation of multidimensional crystallization processes. Computers & Chemical Engineering, v. 26, pp. 1103-1116.

[131] Yang, Y., Ma, C. Y, Wang, X. Z. (2012) Optimisation and Closed-loop Control of Crystal Shape Distribution in Seeded Cooling Crystallisation of L-Glutamic Acid. In: 8th IFAC Symposium on Advanced Control of Chemical Processes, Singapore, July 10-13, 2012, pp. 216-221.

[132] Rajagopalan, A. K., Bötschi, S., Morari, M., Mazzotti, M. (2018). Feedback Control for the Size and Shape Evolution of Needle-like Crystals in Suspension. II. Cooling Crystallization Experiments. Crystal Growth & Design, v.18, pp. 6185-6186.

[133] Kwon, JSI., M. Nayhouse, P. D. Christofides and G. Orkoulas, "Modeling and Control of Crystal Shape in Continuous Protein Crystalization, Chemical Engineering Science 2014, v.107, p.47-57.

[134] Kwon, JSI., M. Nayhouse, G. Orkoulas and P. D. Christofides, Crystal Shape and Size Control Using a Plug Flow Crystallization Configuration, Chemical Engineering Science 2014, v. 119, p. 30-39.

[135] Gunawan, R.; Fusman, I.; Braatz, R. D. High Resolution Algorithms for Multidimensional Population Balance Equations. AIChE Journal, 2004, 50 (11), 2738-2749.

[136] Yang, G; Kubota, N.; Sha, Z.; Louhi-Kultanen, M. Wang, J. Crystal Shape Control by Manipulating Supersaturation in Batch Cooling Crystallization. Crystal Growth & Design 2006, 6 (12), 2799-2803.

[137] Grover M. A.; Griffin D. J.; Tang X.; Kim Y.; Rousseau R. W. Optimal feedback control of batch self-assembly processes using dynamic programming. Journal of Process Control 2020, 88, 32-42. https://doi.org/10.1016/j.jprocont.2020.01.013

[138] Toro, R., Kaduk, J, Delgado, M, de D, G.D. Structural characterization of praziquantel: a broad spectrum anthelmintic, in powder diffraction. ICDD Annual Spring Meetings. *Powder Diffr.* , **2014**, 29 (2), 206–207.

[139] Allesø, M.; van den Berg, F.; Cornett, C.; Jørgensen, F. S.; Halling-Sørensen, B.; de Diego, H. L.; Hovgaard, L.; Aaltonen, J.; Rantanen, J.

Solvent Diversity in Polymorph Screening. Journal of Pharmaceutical Sciences **2008**, *97* (6), 2145–2159. https://doi.org/10.1002/jps.21153.

[140] Gu, C.-H.; Li, H.; Gandhi, R. B.; Raghavan, K. Grouping Solvents by Statistical Analysis of Solvent Property Parameters: Implication to Polymorph Screening. *International Journal of Pharmaceutics* **2004**, *283* (1–2), 117–125. https://doi.org/10.1016/j.ijpharm.2004.06.021.

[141] Braun, D. E.; Gelbrich, T.; Kahlenberg, V.; Tessadri, R.; Wieser, J.; Griesser, U. J. Stability of Solvates and Packing Systematics of Nine Crystal Forms of the Antipsychotic Drug Aripiprazole. *Crystal Growth & Design* **2009**, *9* (2), 1054–1065. https://doi.org/10.1021/cg8008909.

[142] Kons, A.; Bērziņš, A.; Actiņš, A.; Rekis, T.; van Smaalen, S.; Mishnev, A. Polymorphism of R-Encenicline Hydrochloride: Access to the Highest Number of Structurally Characterized Polymorphs Using Desolvation of Various Solvates. *Crystal Growth & Design* **2019**, *19* (8), 4765–4773. https://doi.org/10.1021/acs.cgd.9b00648.

[143] Liu, Y.; Zhang, X.; Zhou, L.; Du, S.; Wu, S.; Gong, J. Development and Structure Analysis of Crystal Forms of Apabetalone: Solvates and Polymorphs. *Crystal Growth & Design* **2021**, *21* (7), 3864–3873. https://doi.org/10.1021/acs.cgd.1c00187.

[144] Yang, P.; Qin, C.; Du, S.; Jia, L.; Qin, Y.; Gong, J.; Wu, S. Crystal Structure, Stability and Desolvation of the Solvates of Sorafenib Tosylate. *Crystals* **2019**, *9* (7), 367. https://doi.org/10.3390/cryst9070367.

[145] Vangala, V. R.; Chow, P. S.; Tan, R. B. H. The Solvates and Salt of Antibiotic Agent, Nitrofurantoin: Structural, Thermochemical and Desolvation Studies. *CrystEngComm* **2013**, *15* (5), 878–889. https://doi.org/10.1039/C2CE26575C.

[146] Burger, A.; Ramberger, R. On the Polymorphism of Pharmaceutical and Other Molecular Crystals. I. *Microchim. Acta* **1979**, 72, 259–271.https://doi.org/10.1007/BF01197379

[147] Burger, A.; Ramberger, R. On the polymorphism of pharmaceuticals and other molecular crystals. II. *Microchim. Acta* **1979**, 72, 273–316. https://doi.org/10.1007/BF01197380.

[148] Yu, L. Inferring Thermodynamic Stability Relationship of Polymorphs from Melting Data. *Journal of Pharmaceutical Sciences* **1995**, *84* (8), 966–974. https://doi.org/10.1002/jps.2600840812.

[149] Nicoud, L.; Licordari, F.; Myerson, A. S. Estimation of the Solubility of Metastable Polymorphs: A Critical Review. *Crystal Growth & Design* **2018**, *18* (11), 7228–7237. https://doi.org/10.1021/acs.cgd.8b01200.

[150] Sha, J.; Gong, Y.; Cao, Z.; Huang, Z.; Hu, X.; Wan, Y.; Sun, R.; He, H.; Jiang, G.; Li, Y.; Li, T.; Ren, B. Solid-Liquid Phase Equilibrium of Praziquantel in Eleven Pure Solvents: Determination, Model Correlation, Solvent Effect, Molecular Simulation and Thermodynamic Analysis. *The Journal of Chemical Thermodynamics* **2021**, *154*, 106327. https://doi.org/10.1016/j.jct.2020.106327

[151] Li, R.; Chen, X.; He, G.; Wu, C.; Gan, Z.; He, Z.; Zhao, J.; Han, D. The Dissolution Behaviour and Thermodynamic Properties Calculation of Praziquantel in Pure and Mixed Organic Solvents. *The Journal of Chemical Thermodynamics* **2020**, *144*, 106062. https://doi.org/10.1016/j.jct.2020.106062.

[152] Liu, Y.; Zhang, X.; Wang, M.; Ma, Y.; Tang, W. Uncovering the Effect of Solvents on Solid-Liquid Phase Equilibrium of Praziquantel. *Journal of Molecular Liquids* **2020**, *297*, 111917. https://doi.org/10.1016/j.molliq.2019.111917.

Appendix A

Polymorphism of Praziquantel: Analytical and experimental procedures and complementary results

This appendix contains the supporting information for Chapter 4, consisting of instruments and analytical procedures, experimental conditions for the cooling crystallization screening (experimental temperatures and estimated concentrations employed), description of water-vapor diffusion the procedure, PXRD diffractograms, and DSC/TGA thermograms, and equations used for the estimation of the transition temperature from melting data.

A.1 Instruments and analytical procedures

Powder X-ray diffraction (PXRD): Patterns were obtained using a PanAnalytical X'Pert Pro diffractometer using a monochromatic Cu Kα radiation source with nickel filter λ = 1.5418 Å generated at 45 kV and 40 mA, with an X'Celerator high-speed detector. The data were obtained for 2ϑ between 4° and 40° with a step size of 0.0167° at a step time of 60 seconds for a slow scan rate (0.03556°/s). Zero background silicon plate was used to carry out the measurements.

Thermal analyses: The DSC samples were heated at a rate of 10 ^{o}C/min from 40 to 200 ^{o}C under nitrogen atmosphere (flow rate of 50 mL/min). In each analysis, about 3 mg of the samples were accurately weighted, filled into Tzero aluminum DSC pans (TA Instruments, USA), and crimped using aluminum lids. TGA Samples (10 mg) were weighed in Platinum-HT pans and analyzed from 25 to 200 ^{o}C at a rate of 10.0 ^{o}C/min. The nitrogen flow rate was 40 mL/min for the balance gas and 60 mL/min for the sample gas.

Karl Fischer (KF) coulometric titration: Hydranal™ Water Standard 1.0 (1 mg/g) was used to check the procedure accuracy. In order to minimize the error in titration, about 10 mg of the solid samples (hydrate crystals) were previously dissolved in 1 mL of anhydrous methanol. About 0.5g of the solution was accurately weighted for each titration analysis. A blank analysis using pure anhydrous methanol (the same used right before sample preparation) was performed before any determination.

SEM: Double-coated conductive carbon tape was glued to conventional SEM stubs. The samples were coated with an ultra-thin layer (~10 nm) of Au-Pd (Gold and Platinum electrode) by sputter coating.

A.2 Cooling crystallization screening

Table A. 1 - Experimental temperatures for the cooling crystallization screening from single solvents

Solvent	Initial saturation temperature (°C)		Final set temperature (°C)
	Low	High	
Acetone	20	40	-10
Methanol	20	50	-10
Ethanol	20	60	-10
1-Propanol	20	60	-10
Isopropanol	20	60	-10
1-Butanol	20	60	-10
Ethyl acetate	20	60	-10
Dimethylformamide	20	60	-10
Dimethylacetamide	20	60	-10
Tetrahydrofuran	20	50	-10
Acetonitrile	20	60	-10
Toluene	20	60	-10
1,4-dioxane	30	60	14
Acetic Acid	30	60	17
Triethylamine	20	60	-10
Dichloromethane	5	25	-10
Anisole	20	60	-10
Dimethyl sulfoxide	40	60	20
2-butanone	20	60	-10

The estimated concentration of praziquantel (mass of praziquantel per 1 mL of solvent) obtained from approximate solubility tests are reported in Table A.2.

Table A. 2 - Estimated concentration of praziquantel employed in the screening experiments

Solvent	Estimated concentration (mg of PZQ / mL of solvent)	
	Low	High
Acetone	60	128
Methanol	86	647
Ethanol	54	415
1-Propanol	58	450
Isopropanol	41	220
1-Butanol	50	390
Ethyl acetate	49	116
Dimethylformamide	124	448
Dimethylacetamide	133	510
Tetrahydrofuran	150	414
Acetonitrile	56	496
Toluene	55	248
1,4-dioxane	137	445
Acetic Acid	84	638
Triethylamine	58	328
Dichloromethane	32	135
Anisole	147	420
Dimethyl sulfoxide	284	495
2-butanone	44	128

A.3 Water Vapor Diffusion Procedure

Fresh DMA and AA solvate crystals were placed on filter paper one at a time. The filter paper was put inside a desiccator containing ultrapure water in the bottom part (see Figure A.1) and in a 20 mL vial arranged beside it. The

system was closed and connected to the vacuum line to promote a saturated water vapor atmosphere. The experiments were done in triplicate for each solvate.

Figure A. 1 - Water vapor diffusion apparatus.

A.4 PXRD diffractograms and DSC/TGA thermograms

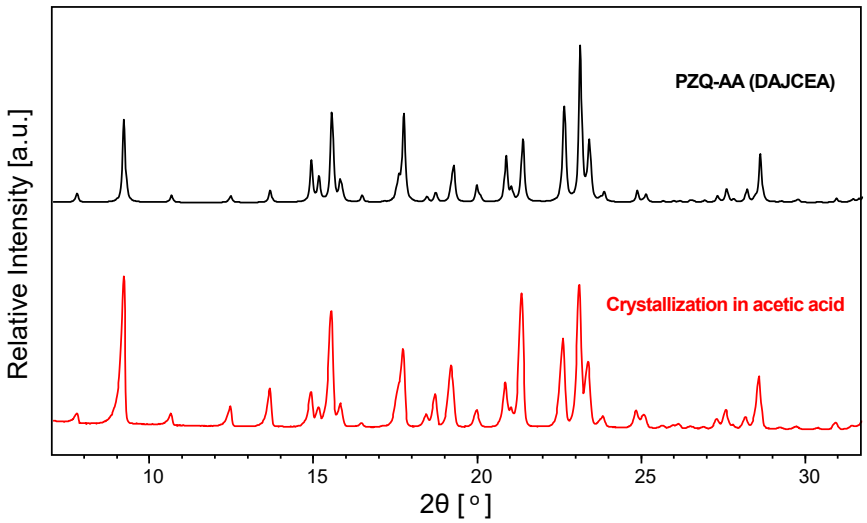

Figure A. 2 - PXRD pattern comparison of PZQ-AA obtained by crystallization in acetic acid and the simulated powder pattern of PZQ-AA (DAJCEA).

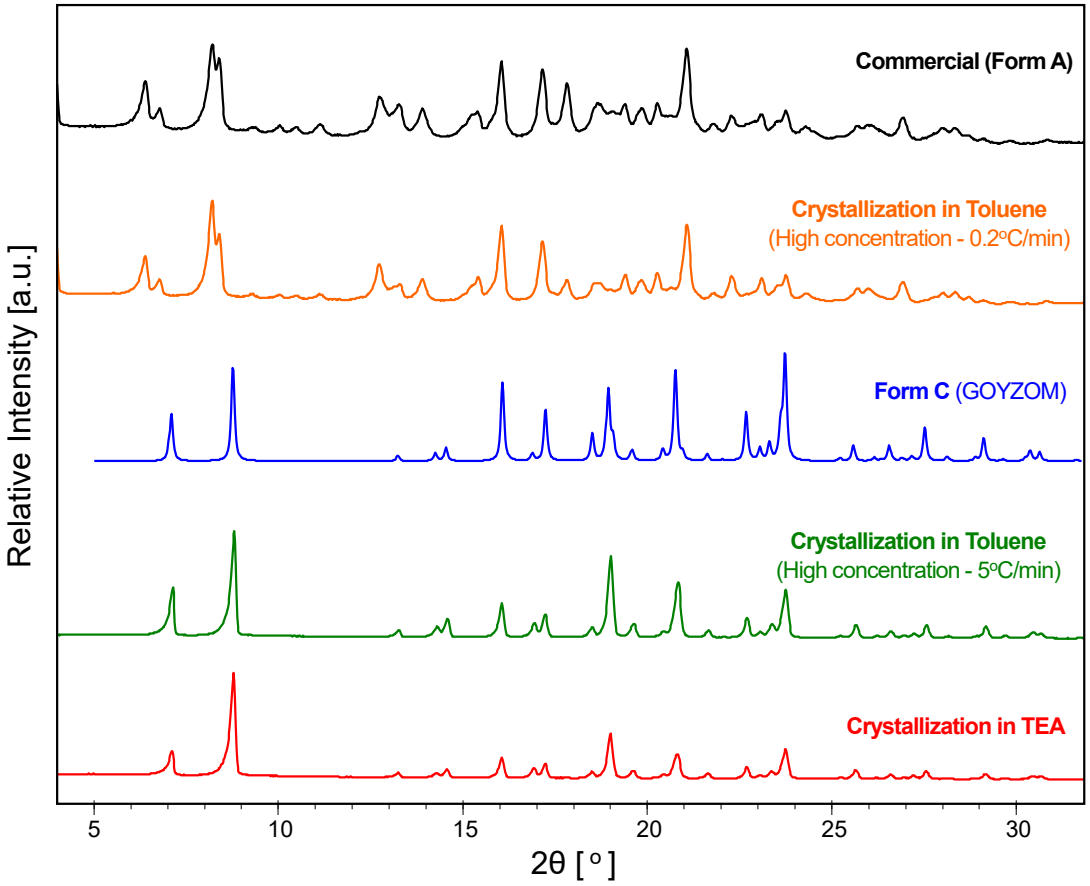

Figure A. 3 - PXRD pattern obtained by crystallization in toluene and TEA for the first screening and comparison with Forms A and C.

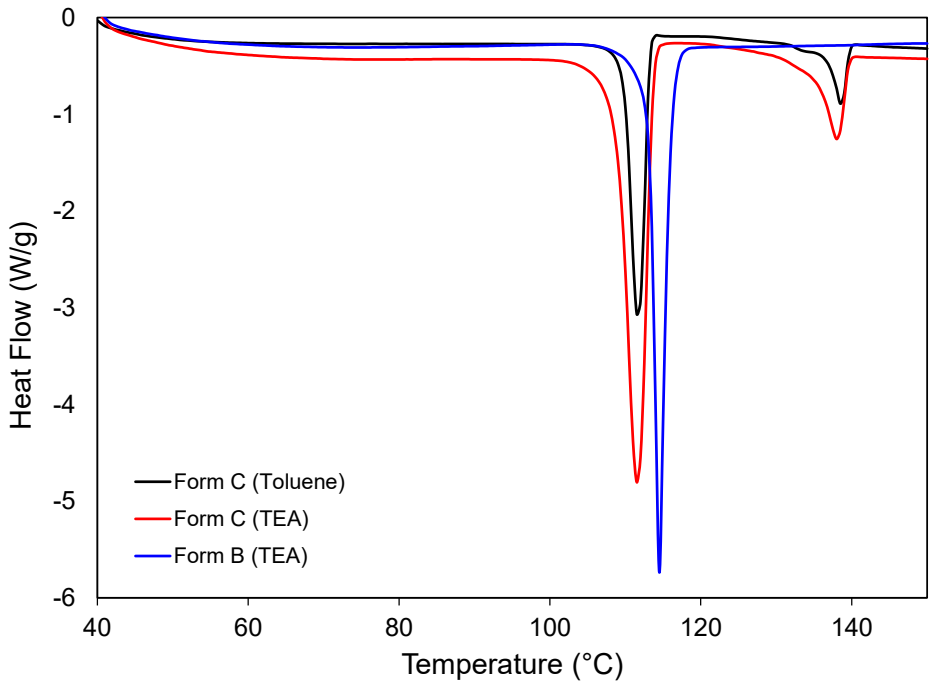

Figure A. 4 - DSC curves of Form C obtained from crystallization in toluene (high initial concentration and fast cooling rate, black curve) and TEA (red curve), and Form B obtained from crystallization in TEA (no agitation and no pre-filtration of solution, blue curve).

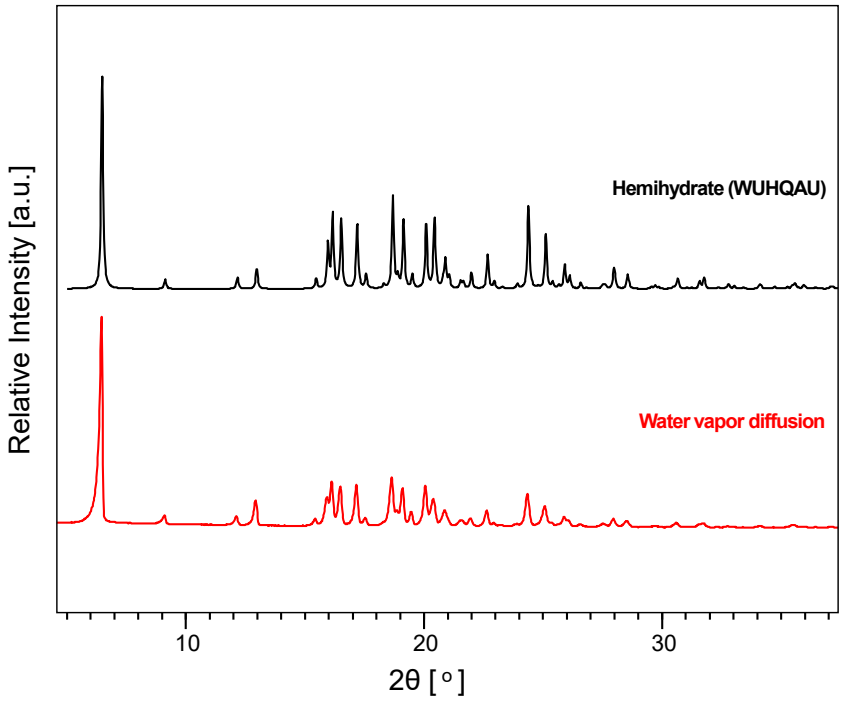

Figure A. 5 - PXRD pattern comparison of simulated PZQ-HH (WUHQAU, black) and the experimental pattern obtained after water-vapor diffusion in PZQ-AA (red).

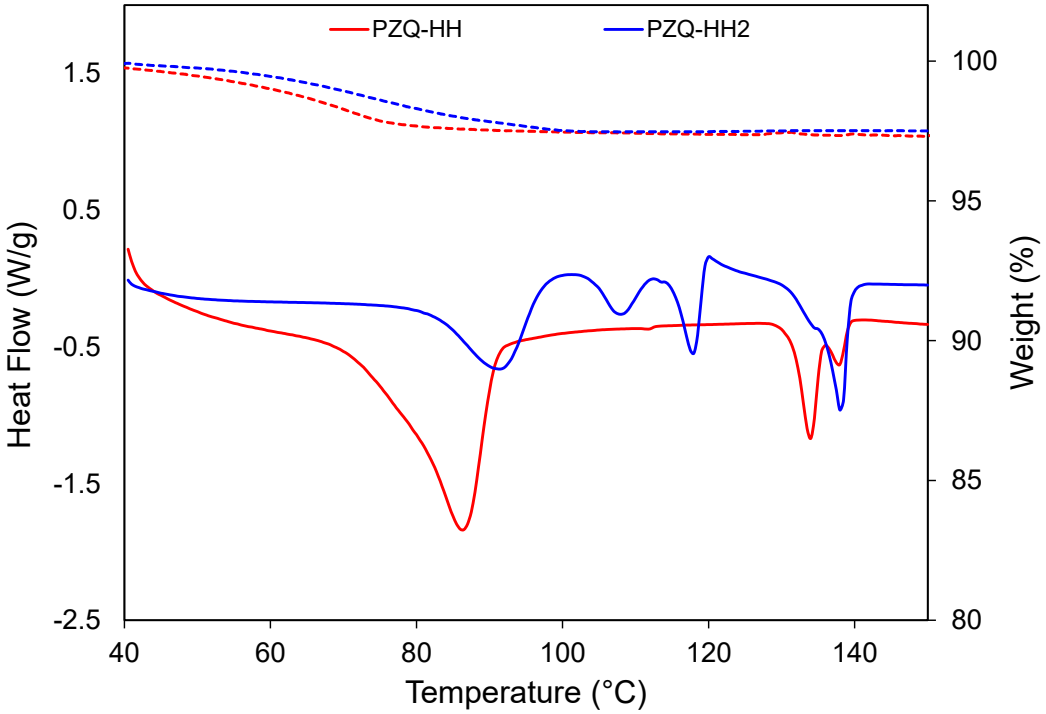

Figure A. 6 - DSC (solid lines) and TGA (dashed lines) thermograms of PZQ-HH obtained by water-vapor diffusion experiment in PZQ-AA (red), and PZQ-HH2 obtained by crystallization from water/methanol mixture 40:60 (blue).

A.5 Estimation of the transition temperature from melting data

The method proposed by Yu to determine the T_r of a pair of enantiotropic polymorphs was used in Section 3.2. Based on Yu's method, the following expression of T_r can be obtained[1,2]:

$$T_r = \frac{\Delta H_{f,1} - \Delta H_{f_2} + (C_{p,L} - C_{p,2})(T_{f,2} - T_{f,1})}{\frac{\Delta H_{f,1}}{T_{f,1}} - \frac{\Delta H_{f,2}}{T_{f,2}} + (C_{p,L} - C_{p,2})\, ln\left(\frac{T_{f,2}}{T_{f,1}}\right)} \quad (A.1)$$

where $\Delta H_{f,i}$ and $T_{f,i}$ are the molar enthalpy of fusion and the melting temperature of the form i, respectively $(i = 1, 2)$. The index $i = 1$ refers to the lower melting form, and $i = 2$ to the higher melting form. $C_{p,L}$ and $C_{p,2}$ are the molar heat capacities of the supercooled liquid and the higher melting form, respectively.

The four parameters $\Delta H_{f,1}$, $\Delta H_{f,2}$, $T_{f,1}$, and $T_{f,2}$ are readily known from the DSC data. Using DSC data, a molar heat capacity C_p can be estimated by:

$$C_p = \frac{Q}{(dT/dt)} M \qquad \text{(A. 2)}$$

where Q is the heat flow rate per unit of solid mass (W/g), dT/dt is the heating rate (K/s), and M is the molar mass (g/mol).

The estimation of $C_{p,L}$ and $C_{p,2}$ was obtained by Eq. A.2 right after and right before the melting event, respectively. The transition temperatures T_r for the pairs B-C and G-C were calculated using Eq. A.1 with the respective melting data of the polymorphs. Table A.3 shows the differences $(C_{p,L} - C_{p,s})$ for Forms B and G, used for the T_r calculations ($C_{p,s}$ refers to the heat capacity of the respective solid phase). For this determination, the heat flow rate signal from the empty pan under the same conditions was subtracted from the sample data.

Table A.3 - Estimates of $(C_{p,L} - C_{p,s})$ for Forms B and G.

Form	$(C_{p,L} - C_{p,s})$ $(J/mol \cdot K)$
B	46.86
G	86.23

References

(1) Yu, L. Inferring Thermodynamic Stability Relationship of Polymorphs from Melting Data. *Journal of Pharmaceutical Sciences* **1995**, *84* (8), 966–974. https://doi.org/10.1002/jps.2600840812.

(2) Qi, M.-H.; Hong, M.-H.; Liu, Y.; Wang, E.-F.; Ren, F.-Z.; Ren, G.-B. Estimating Thermodynamic Stability Relationship of Polymorphs of Sofosbuvir. *Crystal Growth & Design* **2015**, *15* (10), 5062–5067. https://doi.org/10.1021/acs.cgd.5b01038.

Appendix B

Comparison of solubility data of praziquantel in organic solvents

This appendix contains a comparação entre os dados experimentais e modelos obtidos nesse estudo com dados reportados na literatura.

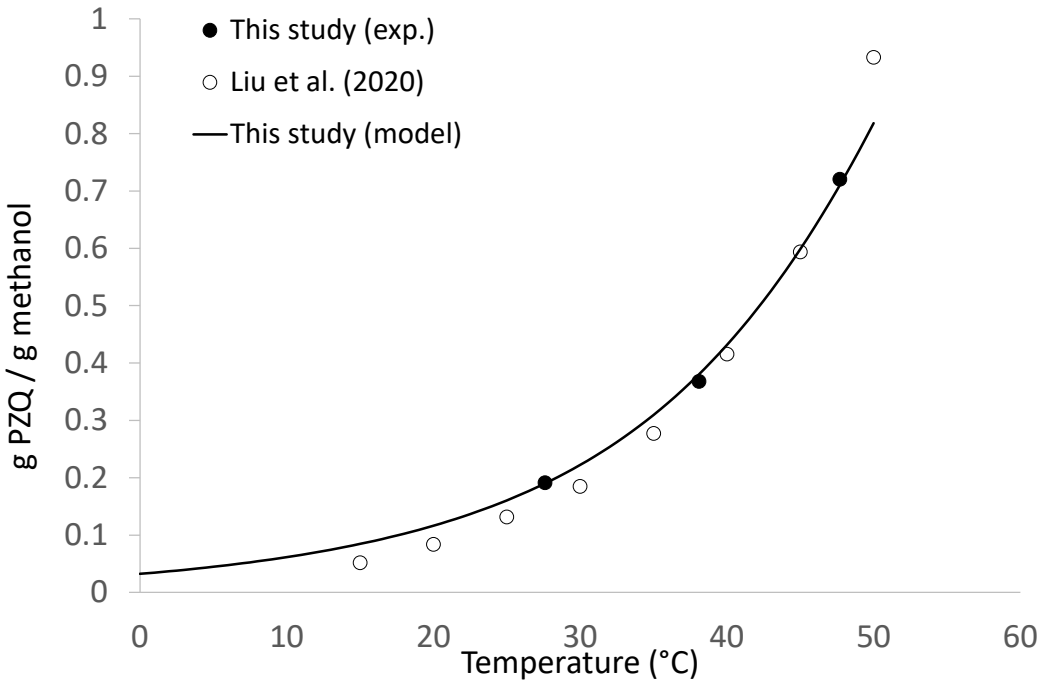

Figure B. 1 - Solubility data of PZQ in methanol (g/g of methanol).

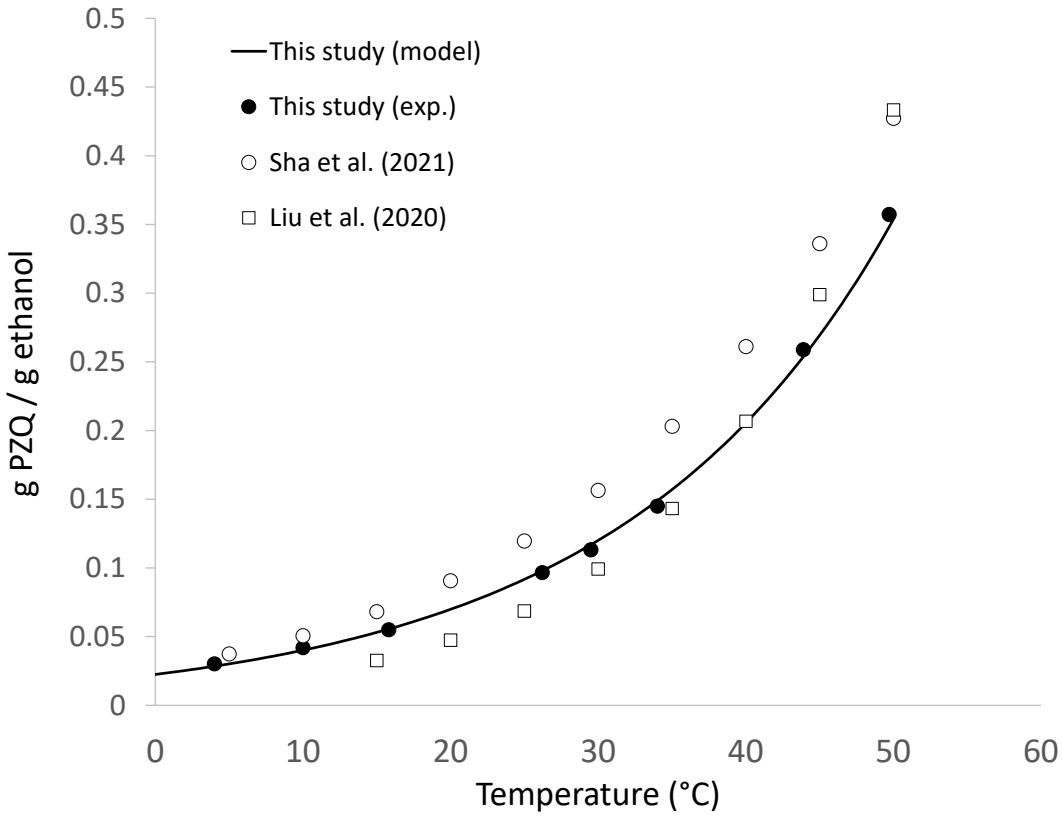

Figure B. 2 - Solubility data of PZQ in ethanol (g/g of ethanol).

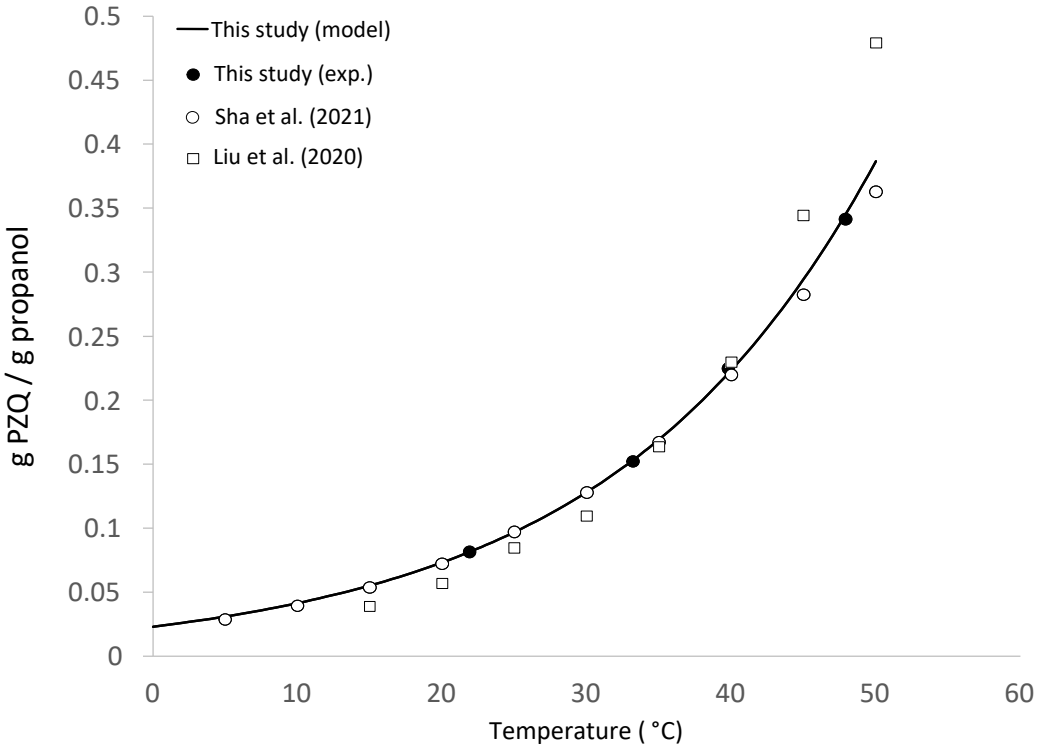

Figure B. 3 - Solubility data of PZQ in propanol (g/g of propanol).

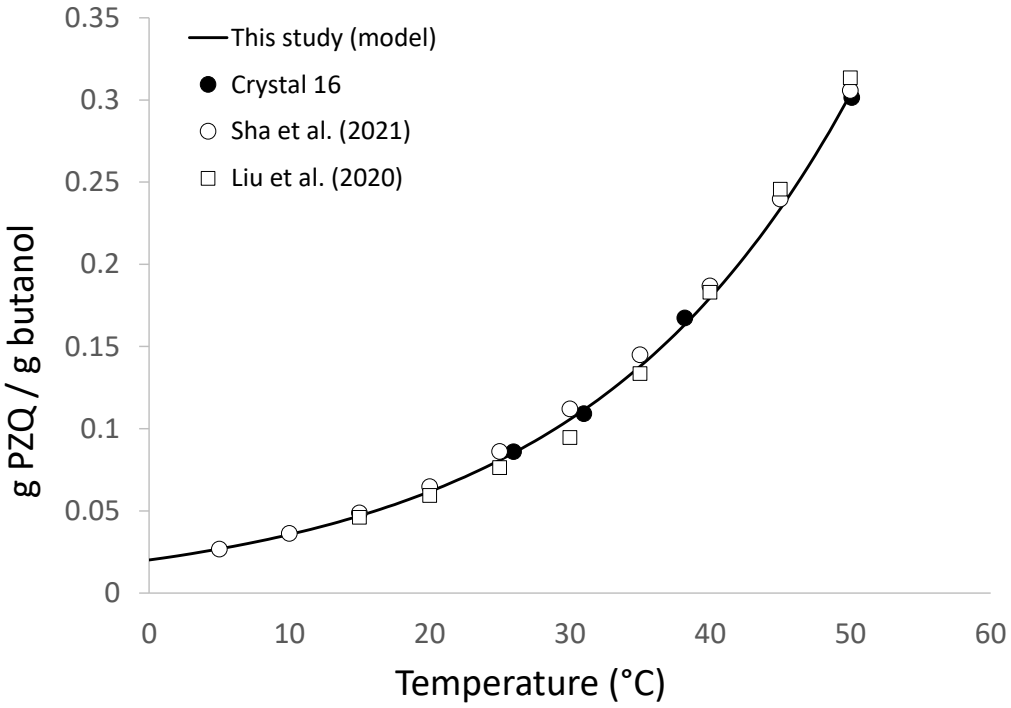

Figure B. 4 - Solubility data of PZQ in butanol (g/g of butanol).

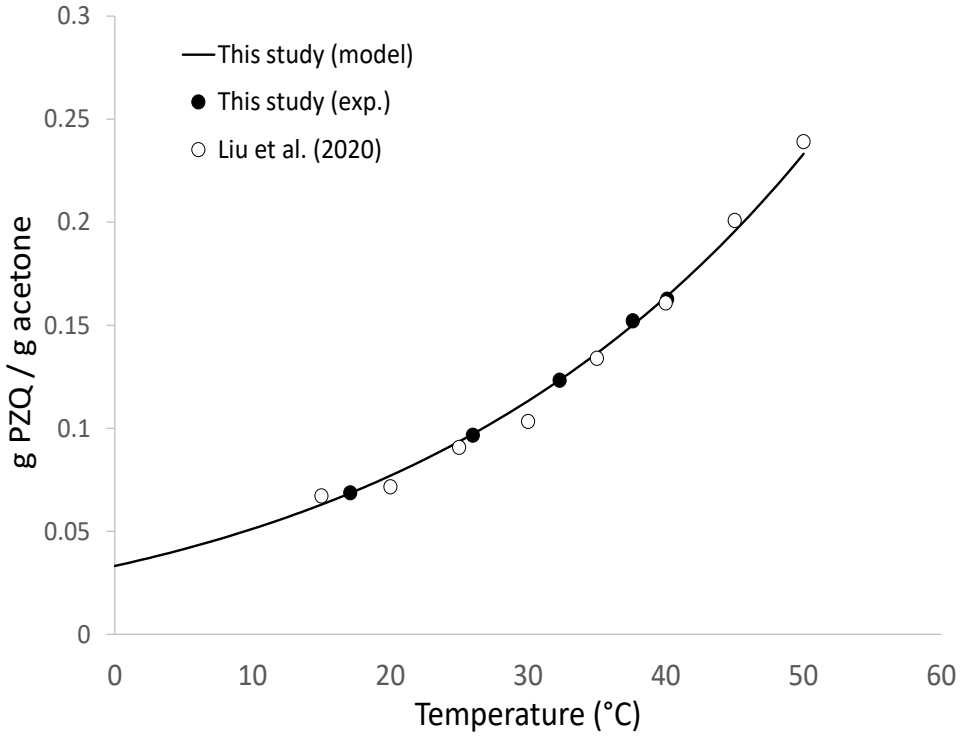

Figure B. 5 - Solubility data of PZQ in acetone (g/g of acetone).

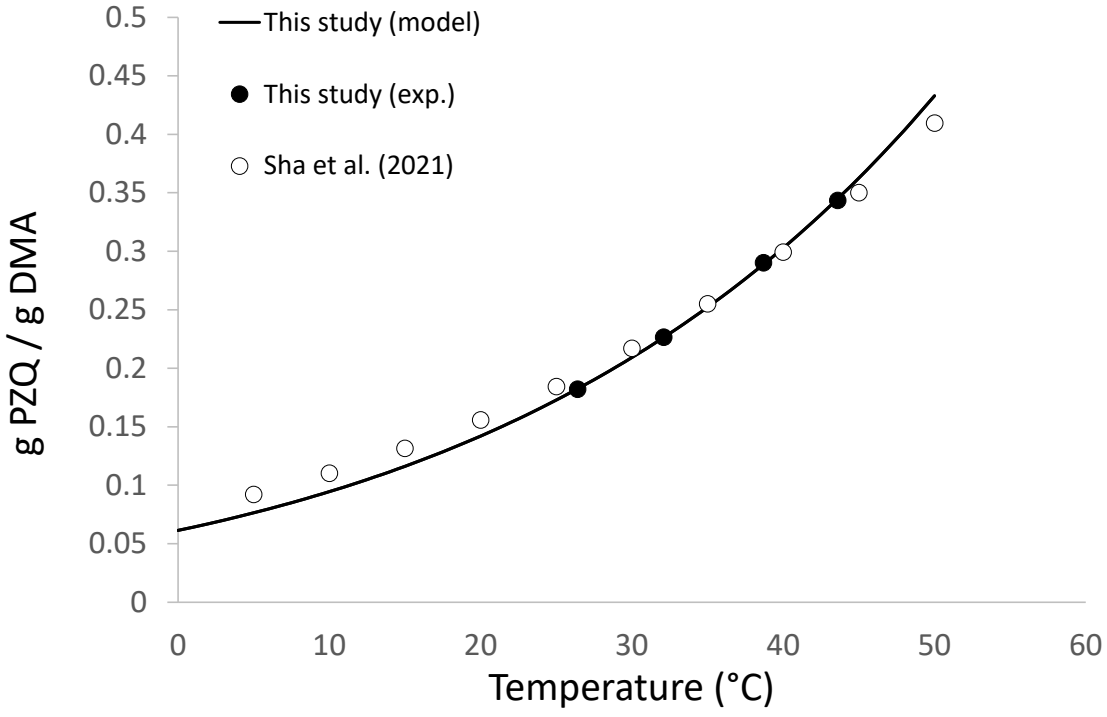

Figure B. 6 - Solubility data of PZQ in DMA (g/g of DMA).

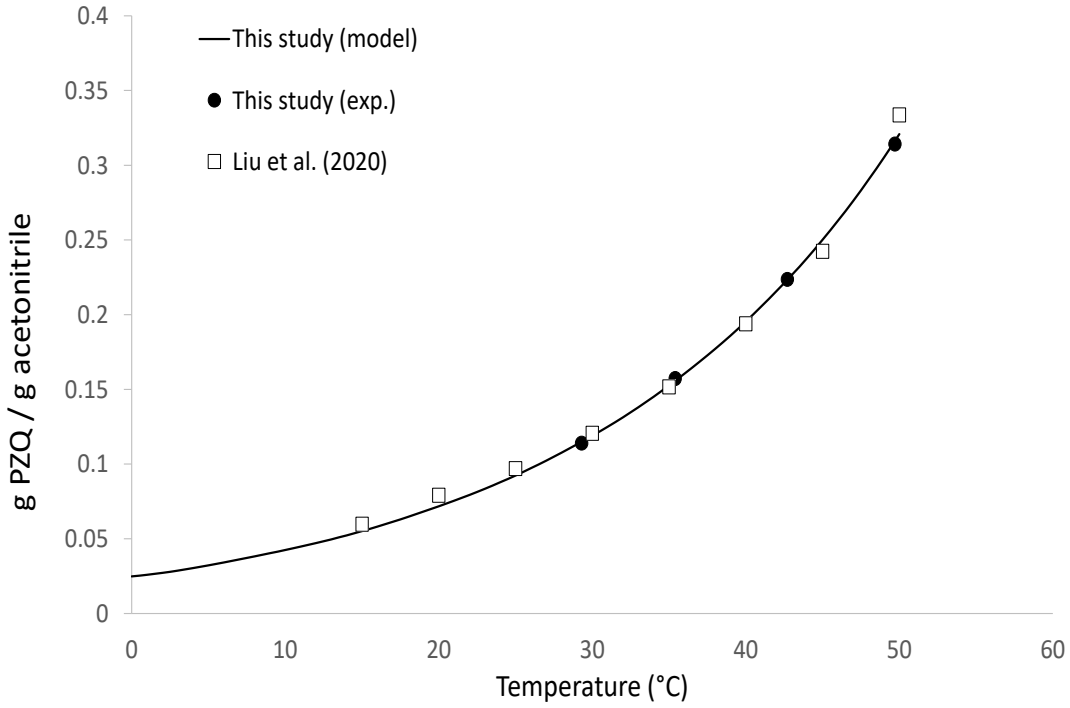

Figure B. 7 - Solubility data of PZQ in acetonitrile (g/g of acetonitrile).

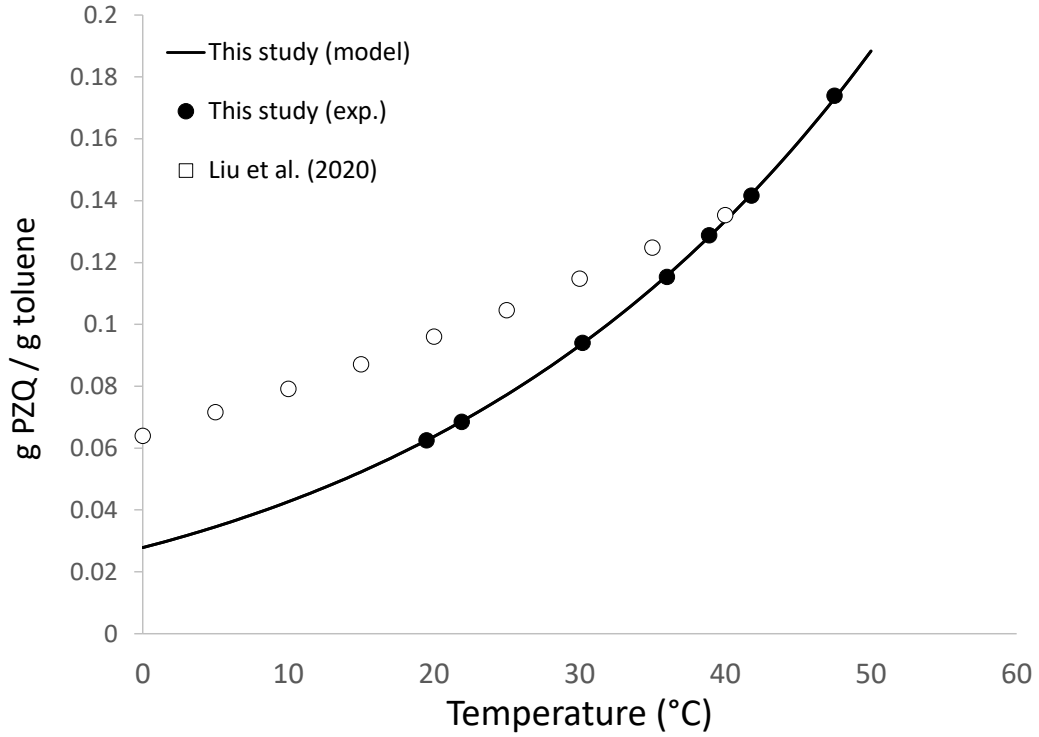

Figure B. 8 - Solubility data of PZQ in toluene (g/g of toluene).